RE-EVALUATING PLUTON/VOLCANO CONNECTIONS AND IGNEOUS TEXTURES IN LIGHT OF INCREMENTAL MAGMA EMPLACEMENT

Ryan Douglas Mills

A dissertation submitted to the faculty of the University of North Carolina at Chapel Hill in partial fulfillment of the requirements for the degree of Doctor of Philosophy in the Department of Geological Sciences.

Chapel Hill
2012

Approved by:

Drew Coleman

Allen Glazner

Alan Boudreau

Jonathan Lees

Kevin Stewart

ABSTRACT

RYAN DOUGLAS MILLS: Re-evaluating pluton/volcano connections and igneous textures in light of incremental magma emplacment
(Under the direction of Drs. Drew Coleman and Allen Glazner)

Zircon U/Pb geochronologic data collected within the past ten years indicate that plutons are emplaced incrementally over time periods of 10^5 to 10^6 annum at magma accumulation rates on the order of 10^{-4}-10^{-3} km^3/a. Although incremental emplacement of magmas is now widely accepted, evaluation of the wide-ranging effects on pluton-volcano connections and the generation of magma diversity has just begun.

Magma emplacement rates calculated for large ignimbrites (10^{-2} km^3/a) are higher than most estimates for plutons (10^{-4}-10^{-3} km^3/a). Thermal models for magma emplacement in the crust predict this rate disparity and suggest that magma emplacement rates of 10^{-2} km^3/a or greater are needed to produce large ignimbrites. Thus, there is a fundamental difference in the rates of accumulation of ignimbrite and pluton magmas but little is known on how individual magmatic centers behave. Geochemistry and U/Pb zircon data from the Mt. Princeton batholith and spatially associated ignimbrites in central Colorado indicate that the vast majority of the batholith was emplaced between periods of ignimbrite eruption at a rate of $1.6x10^{-3}$ km^3/a. The temporal disconnect supports the hypothesis that ignimbrites are generated during periods of high magma flux, without significant fractionation in the upper crust and that plutons represent similar magmas that froze in the crust during periods of low magma flux.

Thermal models and geochronology also indicate that pluton emplacement must be episodic with only small fractions (<5%) of mobile magma existing at any one time. The episodic emplacement of plutons also leads to temperature cycling of the magma, which is hypothesized to affect crystal textures. Experiments on crystal growth of ammonium thiocyanate in a magma analog at approximately 50ºC and plagioclase and olivine growth in an alkali basalt at approximately 1150ºC indicate that temperature cycling changes the texture of magmas dramatically; creating large crystals and decreasing crystal number density. Also, crystal alignment is observed in the magma analog experiments coincident with the thermal gradient. Together, these results indicate that temperature cycling of magmas can affect the crystal size distribution and fabric of the resultant rock and is a variable that needs to be assessed when interpreting igneous textures.

ACKNOWLEDGEMENTS

I gratefully acknowledge the support of my two advisors, Drs. Drew Coleman and Allen Glazner. Their vigor helped me navigate the occasional turbulent waters of graduate studies. I also appreciate the time and thoughts of my Ph.D. committee members: Drs. Alan Boudreau, Jonathan Lees, Kevin Stewart, and Lara Wagner. I am quite grateful to have worked with Jackie Ratner who was a co-author on the publication of chapter 3 of this dissertation. The science presented in chapter 2 was aided by thoughtful comments and reviews by Drs. Matt Zimmerer, Peter Lipman, and Bill McIntosh. My Ph.D. work was enhanced by conversations with fellow graduate students Mike Ackerson, Dr. Jesse Davis, Ryan Frazer, Kayla Ireland, Dr. Russ Mapes, Josh Rosera and Michael Tappa. I especially want to thank former office mate Scott Bennett for field assistance in Colorado and lending his excellent scientific perspective to my work.

Funding for these projects was provided by the National Science Foundation, the Geological Society of America, Sigma Xi, and the Martin Fund at UNC.

Finally, I am lucky to have such wonderful family and friends. All of whom appear to believe in me, at least most of the time.

Coffee is a beverage that puts one to sleep when not drank.
-Alphonse Allais

TABLE OF CONTENTS

LIST OF TABLES

LIST OF FIGURES

Chapter 2

Chapter 3

CHAPTER 1

INTRODUCTION

Since the recognition that plutonic rocks originated as crystallized magmas (rather than metasomatic alteration of sedimentary rock), mapped plutons have been interpreted to represent the frozen remains of large magma chambers. Thus, much of how we interpret the igneous rock record – from the scale of the links between batholiths and volcanic rocks to the scale of rock textures and mineral chemistries – has its foundation on the concept of rapidly assembled high melt-fraction magma bodies in the crust. Data collected within the past ten years, however, are challenging this fundamental concept in igneous petrology.

It is now evident from U/Pb geochronology that plutons are emplaced incrementally over time periods of 10^5 to 10^6 annum (a) at magma accumulation rates on the order of 10^{-4} - 10^{-3} km^3/a (Coleman et al. 2004; Matzel et al. 2006; Michel et al. 2008; Tappa et al. 2011; Davis et al. 2012). Thus, large plutons take longer to construct than small plutons. Although incremental emplacement of magmas is now widely accepted, evaluation of the wide-ranging effects on pluton-volcano connections and the generation of magma diversity has just begun (e.g. Glazner et al. 2008; Tappa et al. 2011).

Magma emplacement rates calculated for large ignimbrites (10^{-2} km^3/a; Schmitz and Bowring 2001; Crowley et al. 2007) are higher than most estimates for plutons (10^{-4} - 10^{-3} km^3/a). Thermal models for magma emplacement in the crust (e.g. Annen 2009) predict this rate disparity and suggest that magma emplacement rates of 10^{-2} km^3/a or greater are needed to produce large ignimbrites. Thus, there is apparently a fundamental difference in the rates of accumulation of ignimbrite and pluton magmas. This raises many questions about how pluton emplacement and ignimbrite generation compare at a single magmatic center. Do

pluton emplacement and ignimbrite generation overlap in time? Or are they distinct events? Is the chemistry of the ignimbrite compared to the plutons suggestive of crystal-liquid separation?

Thermal models also indicate that pluton emplacement must be episodic with only small fractions (<5%) of mobile magma existing at any one time (e.g. Annen 2009). This makes it nearly impossible to produce large-scale chemical and textural zoning in plutons by crystal-liquid separation, which challenges many hypotheses. For example, forming large-scale mineral fabrics in plutons by gravitational settling or syn-emplacement flow (e.g. Zak et al. 2007) is impossible if only small fractions of the pluton are liquid at any one time. The episodic emplacement of plutons also leads to temperature cycling of the magma. Interestingly, textures of ice have been shown to coarsen during temperature cycling (e.g. Donhowe and Hartel 1996; Colbeck 1982) and Johnson and Glazner (2010) hypothesized that temperature cycling produced megacrysts of K-feldspar in the Cathedral Peak Granodiorite. However, no experimental work on magmas has tested this hypothesis.

In the first paper of this dissertation I reconcile the slow emplacement of plutons with the occurrence of large ignimbrites by documenting a temporal disconnect between the emplacement of the Mount Princeton batholith in central Colorado and spatially associated ignimbrites. The second and third papers test the hypothesis that textures in igneous rocks may develop due to crystal aging under oscillating temperature conditions and thermal gradients. Together the three papers present alternative hypotheses to long-standing petrologic hypotheses that have failed in light of our new understanding of what a pluton represents.

CHAPTER 2

TEMPORAL AND CHEMICAL CONNECTIONS BETWEEN PLUTONS AND IGNIMBRITES FROM THE MOUNT PRINCETON MAGMATIC CENTER

ABSTRACT

The Mount Princeton magmatic center, located in central Colorado, consists of the epizonal Mount Princeton batholith, the nested Mount Aetna caldera, and volumetrically minor leucogranites. New CA-TIMS U/Pb zircon ages indicate the majority of the Mount Princeton batholith was emplaced during a period of regional ignimbrite quiescence. The structurally highest unit of quartz monzonite yields a $^{206}Pb/^{238}U$ age of 35.80 ± 0.10 Ma and the youngest dated unit of the quartz monzonite is a porphyritic unit that yields a $^{206}Pb/^{238}U$ age of 35.37 ± 0.10 Ma. Using the exposed, dated volume of the quartz monzonite and new geochronology yields an estimated pluton filling rate of 0.0016 km^3/a. This rate is comparable to accumulation rates published for other plutons, and orders of magnitude slower than fluxes necessary to support accumulation of large eruptible magma volumes. Geochronologic data for the two large ignimbrites spatially associated with the batholith indicate a complete temporal disconnect between pluton building and explosive eruption of magma. The Wall Mountain Tuff erupted from a source in the same geographic area as the Mount Princeton batholith at 37.3 Ma (Ar/Ar sanidine), but no structural evidence of a caldera or temporally associated plutonic rocks is known. The Badger Creek Tuff erupted at 34.3 Ma (Ar/Ar sanidine) during the formation of the Mount Aetna Caldera in the southern portion of the batholith. Our $^{206}Pb/^{238}U$ age for the Badger Creek Tuff is 34.47 ± 0.05. The only analyzed plutonic

rocks of similar age to the Badger Creek Tuff are an extra-caldera dike with a $^{206}Pb/^{238}U$ age of 34.57 ± 0.08 Ma, a ring dike with a $^{206}Pb/^{238}U$ age of 34.48 ± 0.09 Ma and a pluton with a $^{206}Pb/^{238}U$ age of 34.60 ± 0.13 Ma. Major- and trace-element data from the plutons and ignimbrites are inconsistent with significant shallow level fractionation. The small-volume intrusions related to the eruption of the Badger Creek Tuff are chemically similar to the ignimbrite and show no signs of crystal-liquid separation in the shallow crust.

Radiogenic isotope data (Hf, Nd, Pb and Sr) from the batholith and associated ignimbrites indicate a change in source of the magmas from 37 to 30 Ma. Magmatism progressed from partial melts of fertile crust to partial melts of depleted lower crust and/or upper mantle.

INTRODUCTION

Deciphering the chemical and temporal connection between silicic batholiths and silicic ignimbrites is critical to evaluating the significance of crystal-liquid separation and properly interpreting the chemistry of plutonic and volcanic rocks. Specifically, the origin of silicic ignimbrite magmas is debated. The prominent (null) hypothesis involves fractional crystallization of an intermediate magma in the upper crust, resulting in crystals (plutonic rocks) and a complementary felsic liquid (i.e. silicic ignimbrites; Bowen 1928; Bachmann and Bergantz 2004; Hildreth 2004). Compaction can segregate the liquid from the crystals once crystals account for approximately 50% of the system, and the segregation and extraction of a fraction of the liquid from the system is hypothesized to yield silicic ignimbrites (Bachmann and Bergantz 2004; Hildreth 2004). In this model the crystal residue and accompanying interstitial liquid fully solidifies as a batholith. An alternative hypothesis for the origin of plutons and ignimbrites posits that magma flux controls whether an ignimbrite or a pluton is generated (Glazner et al., 2004; Tappa et al. 2011), with high flux leading to ignimbrite eruptions and low flux leading to pluton generation. This hypothesis involves genesis of magmas by partial melting of lower crustal, mafic to intermediate composition rocks with little upper crustal modification (Chen and Arculus 1995; Huppert and Sparks 1998; Sisson et

al. 2005; Annen et al. 2006; Yamamoto 2007; Tappa et al. 2011).

These end-member models predict testable, different temporal and chemical relationships between ignimbrites and plutonic rocks. An upper crustal crystal-liquid separation model predicts synchronous development of the ignimbrite (volcanic) and plutonic components of the magma system. However, because the crystal residue portion (pluton) of the system crystallizes prior to extraction and crystallization of the liquid portion (ignimbrite) a small discrepancy in crystallization ages is predicted between the two. The alternative hypothesis does not require a temporal connection between the ignimbrite and plutonic rocks and predicts a disconnect between ignimbrite and pluton generation that is a function of the change in magma flux through time.

If plutons represent crystal cumulates then the chemistries of volcanic and plutonic rocks are inextricably linked: neither is representative of the source magma composition, and there should be predictable relationships between them. However, if upper crustal crystal-liquid separation is negligible, the plutonic and volcanic rocks should be chemically similar. If so then the bulk chemistry of both rock types is representative of the source magma and can be used to understand the chemical evolution of the system. These differences become increasingly important further back in the geologic record where it is rare to preserve co-genetic volcanic and plutonic rocks.

In order to investigate the temporal and chemical connections between plutonic rocks and ignimbrites we performed high-precision U/Pb zircon geochronology and whole-rock elemental and isotopic geochemistry on intrusive and extrusive rocks associated with the Eocene to Oligocene Mount Princeton magmatic center in central Colorado (Fig 1). Uplift associated with Rio Grande rift faulting, erosion, and rugged topography provide excellent 3D exposure of plutons and intracaldera volcanic rocks. In addition, large ignimbrite outflow sheets related to the magma center are well exposed to the west in the Thirtynine Mile volcanic field (Fig 1).

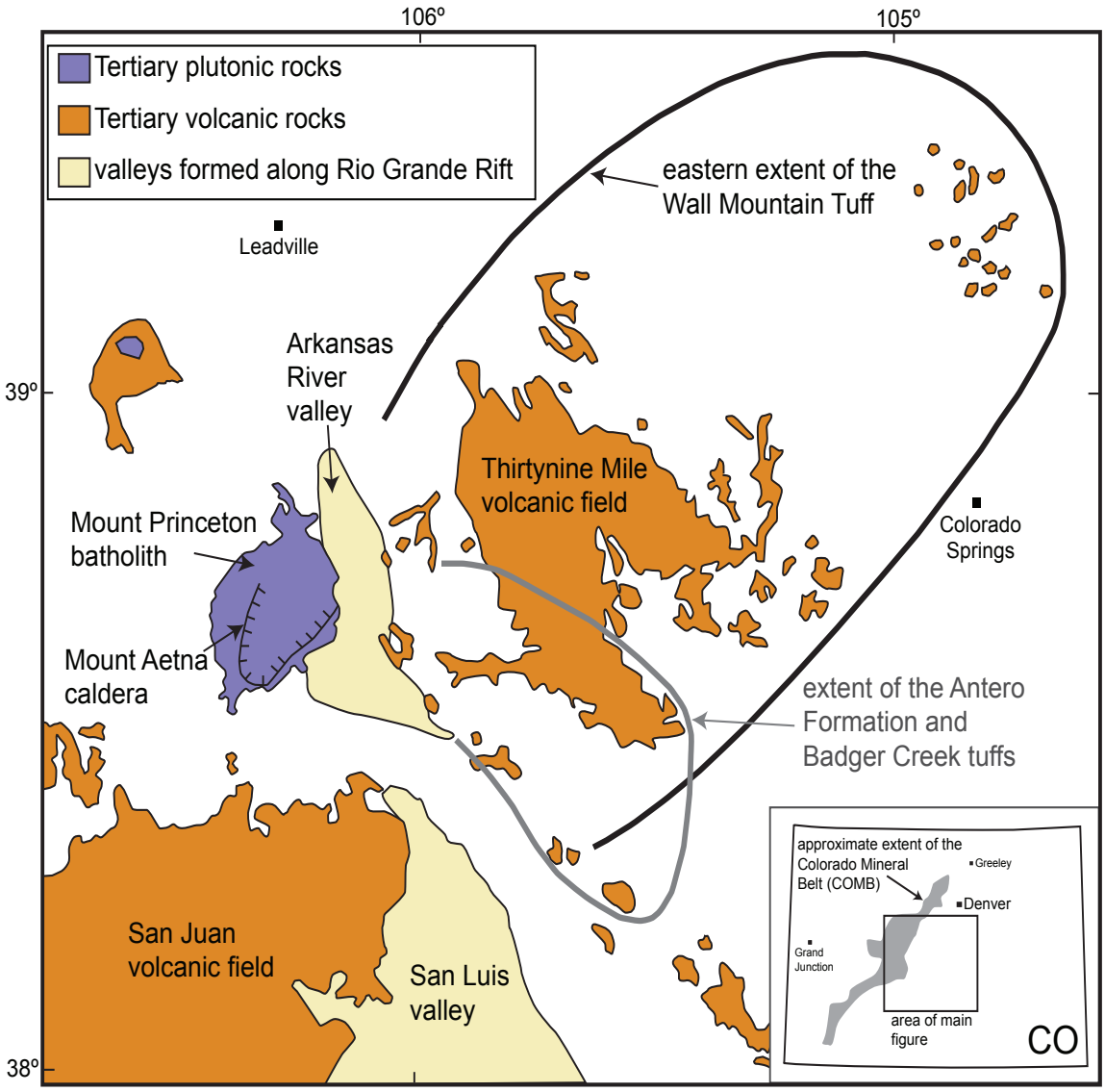

Figure 1 Overview map of central Colorado (after McIntosh and Chapin 2004) highlighting Tertiary plutonic and volcanic rocks and rift valleys. Extent of Wall Mountain Tuff and Badger Creek Tuff are shown. Inset figure of Colorado with approximate extent of the Colorado Mineral Belt in gray.

GEOLOGIC BACKGROUND

Shortly after cessation of Laramide compression (late Eocene-early Oligocene), a magmatic center was active in central Colorado. Palinspastic reconstructions (Atwater and Stock 1998; McQuarrie and Oskin 2010) place this magmatism approximately 1,200 km from the paleotrench along the western boundary of the North American plate. The calc-alkaline geochemistry and linear distribution of the magmatic belt along with overall space-time patterns of magmatism in the western U.S. (Coney and Reynolds 1977) led researchers to suggest that the magmatism was related to flat slab subduction. However, debate exists on whether these magmas were generated in a subduction setting (Mutschler et al. 1987).

Extensive pyroclastic deposits, epizonal plutons and mapped calderas (Lipman 2007; Lipman and McIntosh 2008) record the migration of late Paleogene magmatism in central Colorado from the Sawatch Range in the north to the San Juan volcanic field in the south (Fig. 1). The >1,000 km^3 (Lipman 2007) 37.3 Ma (McIntosh and Chapin 2004; Zimmerer and McIntosh in prep) Wall Mountain Tuff is the largest ignimbrite preserved in the Thirtynine Mile volcanic field. Overall preserved areal distribution of the Wall Mountain Tuff is 10,400 km^2 (Fig. 1; Epis and Chapin 1975; Shannon 1988). Convergence of paleovalleys containing the tuff toward geographic Mount Princeton led several researchers to hypothesize that the source of the Wall Mountain Tuff was the Mount Princeton batholith (Shannon 1988, McIntosh and Chapin 2004; Lipman 2007), the largest Tertiary plutonic body exposed in Colorado (Fig. 1; Tweto 1979; Shannon 1988; Toulmin and Hammarstrom 1990). However, significant difference in initial whole-rock Sr isotopic ratios between the Wall Mountain Tuff and the batholithic rocks led Campbell (1994) to question this correlation.

The Mount Princeton batholith is part of the Sawatch uplift which is directly west of the Arkansas River valley that runs roughly north-south along the main fault of the Rio Grande rift system (Fig. 1). The horst and graben deformation created maximum vertical exposure through the batholith of ~1.5 km. As mapped by Shannon (1988), the majority of the batholith can be divided into interior quartz monzonites and texturally and compositio-

nally diverse border units. Interior and border units are collectively referred to as Mount Princeton Quartz Monzonite (Fig. 2). Imprecise Th-Pb geochronology, compositional zoning, the large number of continuous textural horizons and the lack of cross-cutting relationships led Shannon (1988) to conclude that the Mount Princeton batholith was emplaced, chemically differentiated, and crystallized as a single, large magma body.

The younger Mount Aetna caldera collapse structure complicates the interpretation of the geologic history of the Mount Princeton batholith. The central portion of the batholith subsided into the Mount Aetna cauldron during the eruption of the crystal-rich dacitic Badger Creek and Antero tuffs (Shannon 1988) at 34.3 Ma (McIntosh and Chapin 2004; Zimmerer and McIntosh in prep). The Badger Creek and Antero tuffs are indistinguishable in age and chemistry (McIntosh and Chapin 2004), and for simplicity in this paper we will refer to the tuffs collectively as the Badger Creek Tuff. Evidence for the caldera includes the preservation of intracaldera tuff in the southern portion of the structure, and ring shears and associated ring dikes that extend to the north (Fig. 2; Shannon 1987; Toulmin and Hammarstrom 1990). One of the northern dikes is distinctive because it is preserved outside the mapped caldera boundaries (Fig. 2) and is characterized by the preservation of structures typically attributed to ignimbrites (e.g. flattened pumice). This unit is informally called the tuff dike (Shannon 1988), because of its appearance and distinct cross-cutting relationship with Precambrian wall rocks. The Mount Aetna Quartz Monzonite stock, adjacent to the intracaldera tuff in the southern portion of the batholith, locally grades into a porphyritic ring dike (Shannon 1987; Toulmin and Hammarstrom 1990). The ring dikes and stock are interpreted to have intruded shortly after caldera collapse (Shannon 1987; Campbell 1994).

The youngest plutonic rocks exposed that are associated with the Mount Princeton magmatism include leucogranites that intruded at ~30 Ma (McIntosh and Chapin 2004). The three largest leucogranite intrusions, the Antero, California and North Fork, all cross-cut the older Mount Princeton units (Fig. 2). Whole-rock geochemistry (Campbell 1994) indicates that these intrusions are chemically evolved and likely related to the beginning of bimodal

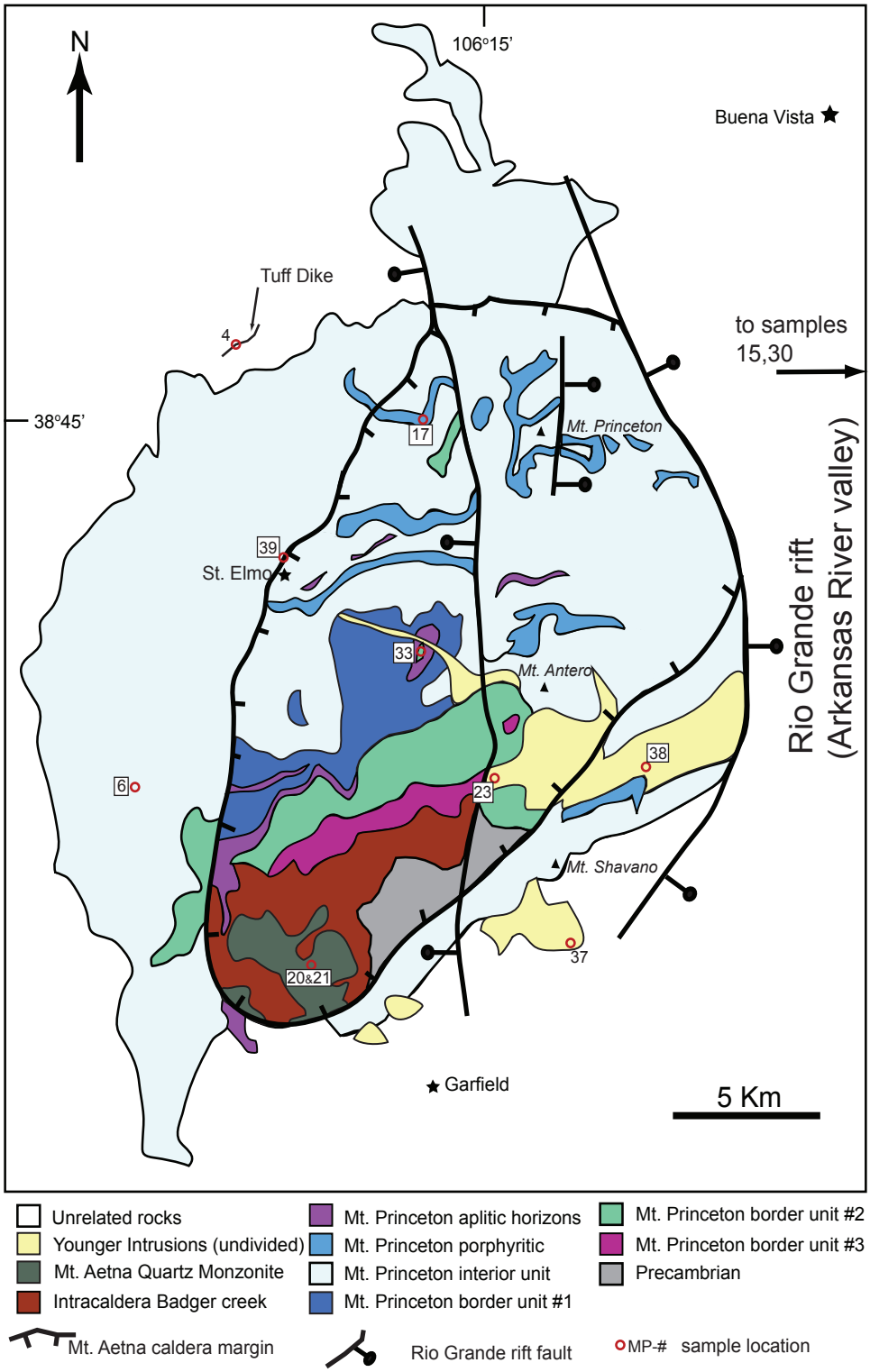

Figure 2 Simplified geologic map of the Mount Princeton batholith modified from Shannon (1988). Sample locations for MP-15 and -30 (not shown) are located in paleovalleys to the east.

magmatism in the area coincident with Rio Grande rifting (Shannon 1988).

METHODS

Elemental chemistry

Samples were ground to a powder using a steel jaw crusher and a ceramic shatterbox. Rock fragments from the tuffs that were powdered were scrutinized using a handlens to limit the amount of lithic material in the powders. Powders were analyzed for major- and traceelement concentrations by Activation Laboratories (Ontario, Canada). Samples were dissolved by lithium metaborate/tetraborate fusion. Major-elements and Sc, Be, V, Sr, Zr, and Ba were analyzed by ICP-OES and all other trace-elements were analyzed by ICP-MS.

Lead, neodymium, and strontium isotope chemistry

Whole-rock powder was dissolved and cations were separated for isotopic analysis following methods outlined by Miller et al. (1995). Isotopic ratios for Pb, Nd and Sr were obtained on the VG Sector 54 thermal ionization mass spectrometer at the University of North Carolina at Chapel Hill. Mass fractionation correction of 0.12%/amu as determined by replicate analyses of NBS-981 was used for Pb isotopic ratios. Isotopic ratios for Nd were normalized to $^{146}Nd/^{144}Nd = 0.7219$ and replicate analyses of standard JNdi yielded $^{143}Nd/^{144}Nd = 0.512109$ (n = 27). Isotopic ratios for Sr were normalized to $^{86}Sr/^{88}Sr = 0.1194$ and replicate analyses of standard NBS-987 yielded $^{87}Sr/^{86}Sr = 0.710269$ (n = 37). Isotope ratios were corrected to initial values using elemental data obtained from Activation Laboratories (this study) and crystallization ages obtained by ID-TIMS U/Pb zircon analyses (this study) or by LA-ICP-MS U/Pb zircon analyses (Zimmerer and McIntosh in prep).

Hafnium in zircon chemistry

Zircons for Hf analysis were mounted in 2.5 cm diameter epoxy rounds and abraded to a depth approximately half way through the average zircon (~ 50 microns). All mounted

zircons were imaged on the scanning electron microscope at the University of North Carolina at Chapel Hill. Cathodoluminescence images were obtained and used to avoid obvious inherited cores during laser analysis.

The Hf isotopic composition of zircon was analyzed by in-situ laser ablation-multicollector-inductively coupled plasma-mass spectrometry (LA-MC-ICPMS) methods using a New Wave Nd:YAG UV 213-nm laser coupled to a Thermo-Finnigan Neptune MCICP-MS with 9 Faraday collectors housed at Washington State University. The laser was operated at both 5 and 10 Hz pulse rate (depending on the thickness of the zircon) with a 40 μm spot. The carrier gas consisted of purified He with small quantities of N_2 to minimize oxide formation and increase sensitivity. Analyses consisted of 60 1-second measurements in static mode, with cups measuring masses 171, 173, 175, 176, 177, 178, 179, 180 and 182. The largest obstacle in LA-MC-ICP-MS Hf isotopic analysis is the isobaric interference of ^{176}Yb and ^{176}Lu on ^{176}Hf. We corrected for these by monitoring interference free isotopes of Lu and Yb and using the known isotopic composition of these elements to determine the contributions of ^{176}Yb and ^{176}Lu to the total mass 176 signal. Whereas the contribution of Lu is minor, the contribution of Yb is large enough (approximately 2 - 15% of the total signal on mass 176) that the mass bias relationship for Yb needs to be carefully considered. The ideal way of determining Yb mass bias is to compare the measured ratio of interference-free Yb isotopes to their known ratio, but this is often difficult in practice due to the low signal intensities on ^{171}Yb and ^{173}Yb. Thus, we assumed a linear relationship between Hf and Yb mass bias, described as: $\beta Yb = x*\beta Hf$. The value for x was determined by analyzing the zircon standards 91500 (^{176}Yb/^{177}Hf ~ 0.03), FC1 (^{176}Yb/^{177}Hf ~ 0.10), and R33 (^{176}Yb/^{177}Hf ~ 0.15) and adjusting the x value to best fit the known ^{176}Hf/^{177}Hf values determined on chemically purified solutions of these zircon standards. The x value and modified ^{176}Yb/^{173}Yb were then used to calculate the Hf isotopic composition of the unknowns.

For in-situ Hf isotopic measurements, the internal measurement error is, by itself, often considerably less than the total uncertainty. Additional causes of uncertainty include

the difficulty in correcting for the Yb interference, instrumental bias, and matrix effects. Although it is difficult to assess the full uncertainty on a given measurement, we conservatively estimate the total uncertainty to be approximately ± 2 εHf units (2σ), based on the reproducibility of analyses of the zircon standards.

Hf isotope results are presented in εHf units, using CHUR values of $^{176}Hf/^{177}Hf$ = 0.282785 and $^{176}Lu/^{177}Hf$ = 0.0336 (Bouvier et al. 2008) and a decay constant value of $1.867e^{-11}$/a (Scherer et al. 2001; Söderlund et al. 2004).

U/Pb Analyses

Samples were crushed using a jaw crusher and a disc mill. Zircon was isolated using standard density (water table and heavy liquids) and magnetic separation techniques. Individual grains were selected using a binocular microscope to represent the range of size and morphology present in the populations. Selected zircon grains were thermally annealed for 48 hours at 900ºC, then chemically abraded for 14 hours at 220ºC in order to eliminate volumes affected by radiation damage and to remove inclusions (Mundil et al. 2004; Mattinson 2005). Depending on the size of the zircon grains and the Pb concentration, fractions consisting of 1 to 3 individual grains were selected for analysis.

Zircon fractions were spiked using a ^{205}Pb-^{233}U-^{236}U tracer (Parrish and Krogh 1987) and dissolved following a procedure modified after Krogh (1973) and Parrish (1987). Uranium and Pb were isolated using HCl anion exchange column chromatography procedures modified after Krogh (1973).

Isotope ratios of both U and Pb were determined by thermal ionization mass spectrometry (TIMS) on a VG Sector 54 mass spectrometer at the University of North Carolina at Chapel Hill. Uranium was run as a metal after loading in graphite and H_3PO_4 on single Re filaments. Lead was loaded in silica gel on single Re filaments. All data were collected using the Daly detector in peak switching mode. Mass fractionation for Pb was determined to be 0.15%/amu over a wide temperature range based on multiple analyses of the NBS-981 common Pb standard. Mass fractionation for U was calculated in real time using the $^{233}U/^{236}U$

ratio (a known constant from the ^{205}Pb-^{233}U-^{236}U tracer) and assuming linear fractionation. Data processing and age calculations were completed using the PbMacDat spreadsheet that is based on the reduction algorithms Schmitz and Schoene (2007). Decay constants used were $^{238}U = 0.155125 \times 10^{-9} \pm 0.16598 \times 10^{-14}$ a^{-1}, and $^{235}U = 0.98485 \times 10^{-9} \pm 0.13394 \times 10^{-13}$ a^{-1} (Steiger and Jäger 1977). All errors are reported at 2σ uncertainty and consider analytical and decay-constant uncertainties. Corrections for initial Th/U disequilibrium (Schmitz and Bowring 2001) were made using [Th] and [U] data for the host rocks (Table 1) following the procedure outlined by Mattinson (1973).

RESULTS

Major- and trace-element chemistry

Geochemical analyses of plutonic rocks from the Mount Princeton batholith (Table 1) generally agree with previously published data (Toulmin and Hammarstrom 1988; Campbell 1994). The Mount Princeton Quartz Monzonite units and the Mount Aetna Quartz Monzonite range from 63 to 67 wt% SiO_2 and major-oxide concentrations negatively correlate with SiO_2 (CaO, MgO, etc., Fig. 3) except Na_2O and K_2O which are positively correlated or do not correlate (Fig. 3). The leucogranites from the batholith range from 75 to 76 wt% SiO_2 (Fig. 3) and are depleted in all other major-elements, except Na_2O and K_2O, relative to the other rocks in the batholith.

Major-element data for both the Badger Creek Tuff sample and the Wall Mountain Tuff sample generally agree with data from Campbell (1994) for the two units (Fig. 3), although there is significant spread in the data for the tuffs (Campbell 1994) that likely is the results of varied crystal content in the samples and winnowing of fine ash during eruption. Our analysis of the Badger Creek Tuff has 64 wt% SiO_2 or 67 wt% SiO_2 when renormalized without volatiles (LOI = 5.4 wt%). Campbell (1994) analyzed samples fall within a range from 62 to 67 wt% SiO_2 (Campbell 1994). The chemistry of the Badger Creek Tuff sample we analyzed is within the range of chemical values for the Mount Princeton Quartz

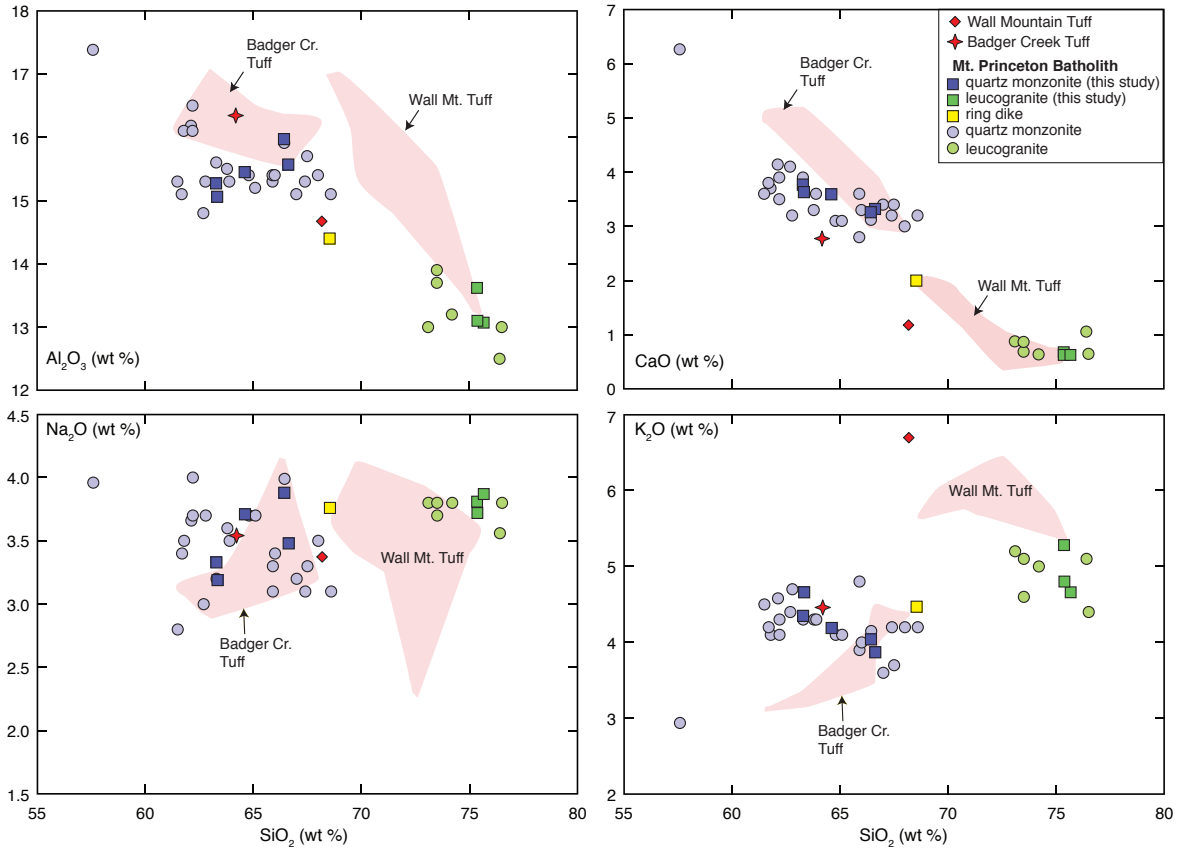

Figure 3 Selected major-element variation diagrams of whole-rock chemistry from this study. Pink fields define data from Campbell (1994) for the Badger Creek Tuff and the Wall Mountain Tuff respectively. Our data for the Badger Creek Tuff and the Wall Mountain Tuff are slightly different than the data from Campbell (1994), likely due to alteration in our samples that was not removed prior to powderization and chemical analysis. Data represented by circles are from Toulmin and Hammarstrom (1990).

Monzonite and the Mount Aetna Quartz Monzonite for most major-elements (Fig. 3). Our analysis of the Wall Mountain Tuff is within the range of Campbell (1994) for all major-elements except SiO_2 (we obtained lower concentrations; 68 wt% vs. 69-75 wt%) and K_2O (we obtained higher concentrations 6.71 vs. 5.38 to 6.43 wt%; Campbell, 1994; Fig. 3). The high concentration of K_2O may reflect some minor alteration.

Rare-earth element (REE) patterns (Fig. 4) for the Mount Princeton and Mount Aetna quartz monzonites and Badger Creek Tuff samples are similar and show LREE enrichment, minor negative Eu anomalies, and slight MREE depletion (Fig. 4). The Wall Mountain Tuff has a pattern similar to the quartz monzonites and the Badger Creek Tuff, but the overall concentrations of the REE are elevated with La at 400 times chondrite (Fig. 4). The leuco-granites have a different REE pattern that is characterized by lower overall concentrations of REE (La around 100 times chondrite), a pronounced negative Eu anomaly, and a well-defined scoop-shape.

Zirconium concentrations in the Wall Mountain Tuff (~ 500 ppm) are higher than the quartz monzonites (Fig. 5) and the Badger Creek Tuff , which have Zr concentrations ranging from ~150 to 300 ppm. The concentration of Zr in the leucogranitic portion of the batholith is lower (approximately 100 ppm). The Zr/Hf ratios of the quartz monzonite rock samples range from 36 to 39, similar to, or slightly higher than the chondritic value of 36.3 (Sun and McDonough 1989). Both the Badger Creek and Wall Mountain tuffs have slightly elevated Zr/Hf ratios of 43 and 40, respectfully. The leucogranites have extremely low Zr/Hf ratios (25 to 29) relative to other rocks analyzed and the chondritic value.

Alkali trace-element (Rb, Sr and Ba) concentrations in the quartz monzonite portion of the batholith are rather homogeneous (Fig. 5) with no clear trend with crystallization age or SiO_2. The leucocratic portion of the batholith is depleted in Sr and Ba and enriched in Rb in comparison to the quartz monzonite portion. Previous results (Campbell 1994) indicate that the Badger Creek and Wall Mountain tuffs have large ranges for Rb, Sr and Ba. Our analyses fall within the ranges established by Campbell (1994) for all 3 alkali trace-elements.

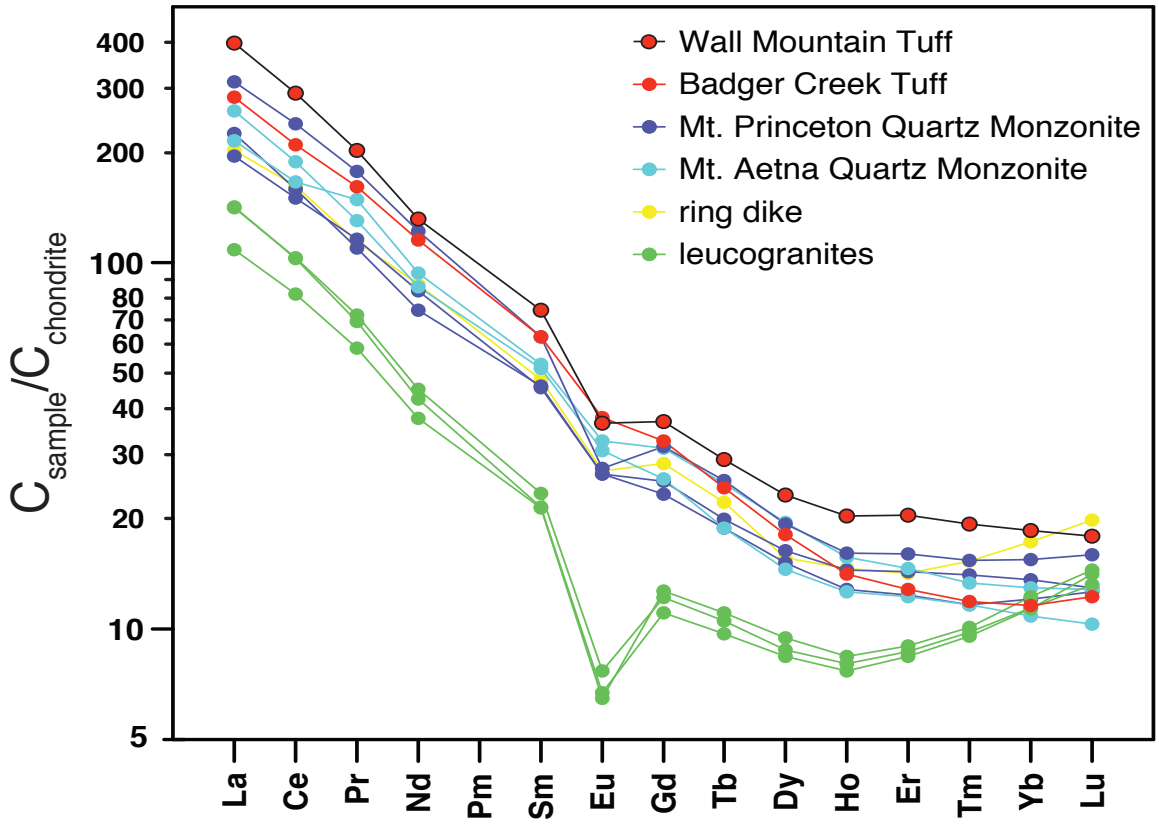

Figure 4 Rare-earth element geochemistry of plutonic rocks from the Mount Princeton batholith, Badger Creek Tuff and Wall Mountain Tuff plotted relative to chondrite (McDonough and Sun 1995).

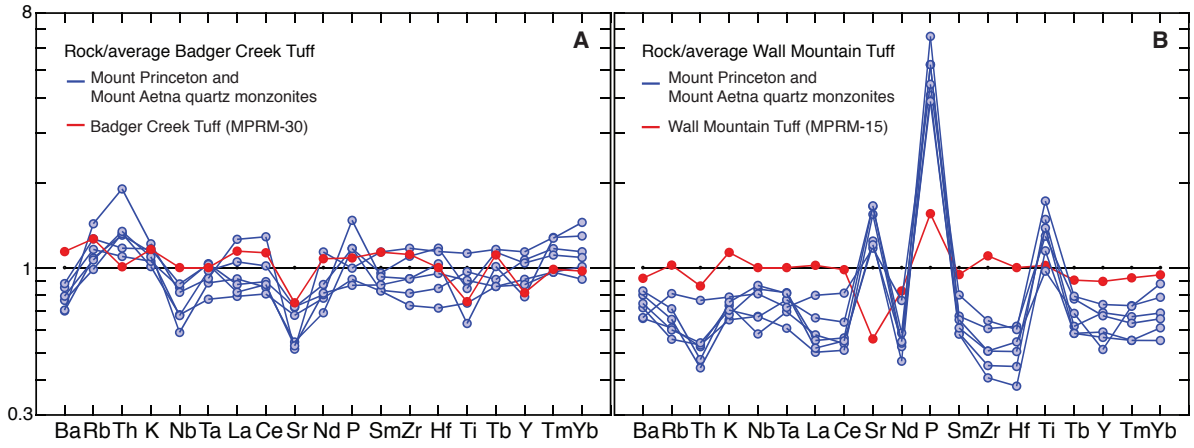

Figure 5 Trace-element variation diagram displaying quartz monzonite sample from the Mount Princeton batholith normalized relative to the average values for Badger Creek Tuff (Campbell 1994; A) and the average values of Wall Mountain Tuff (Campbell 1994; B). Additionally, our analyses of Badger Creek Tuff and Wall Mountain Tuff are shown for comparison.

Whole rock radiogenic isotope chemistry

Strontium

The sample of the Wall Mountain Tuff we analyzed has an initial $^{87}Sr/^{86}Sr$ value of 0.7094 (Table 2; Fig. 6), which is within the range of values obtained by Campbell (1994) for the tuff. The three Mount Princeton Quartz Monzonite samples have initial $^{87}Sr/^{86}Sr$ values ranging from 0.7074 to 0.7078 with no correlation with crystallization age (Fig. 6). Both Mount Aetna Quartz Monzonite samples have initial $^{87}Sr/^{86}Sr$ values of 0.7073 (Fig. 6). The Badger Creek Tuff also has an initial $^{87}Sr/^{86}Sr$ value of 0.7073 (Fig. 6), which is within the range of values obtained by Campbell (1994) for the Badger Creek Tuff. The leucogranites have a large range in initial $^{87}Sr/^{86}Sr$ values ranging from 0.7043 (Mount Antero) to 0.7080 (North Fork).

Neodymium

Neodymium isotopic ratios for quartz monzonites from the Mount Princeton batholith are fairly homogenous (εNd from -9.91 to -9.08), and the leucogranites are only slightly more negative (εNd from -10.11 to -10.44; Table 2; Fig. 7). The Badger Creek Tuff has an εNd of -9.03, similar to, but slightly more radiogenic than the intermediate rocks in the batholith. The Nd in the Wall Mountain Tuff is less radiogenic than any of the intrusive rocks (εNd = -10.66; Fig. 7).

Lead

Initial Pb isotopic ratios for the Badger Creek Tuff ($^{206}Pb/^{204}Pb$ = 18.42, $^{207}Pb/^{204}Pb$ = 15.58, and $^{208}Pb/^{204}Pb$ =38.28) and Wall Mountain Tuff ($^{206}Pb/^{204}Pb$ = 18.02, $^{207}Pb/^{204}Pb$ = 15.6 and $^{208}Pb/^{204}Pb$ = 38.22; Table 2; Fig. 8) are the next most radiogenic of the samples analyzed. The quartz monzonite units have rather homogenous Pb isotopic compositions and show little correlation between the different isotopic ratios (Fig. 8). The range in values for the quartz monzonites ($^{206}Pb/^{204}Pb$ from 17.66 to 18.09, $^{207}Pb/^{204}Pb$ from 15.52 to 15.55 and $^{208}Pb/^{204}Pb$

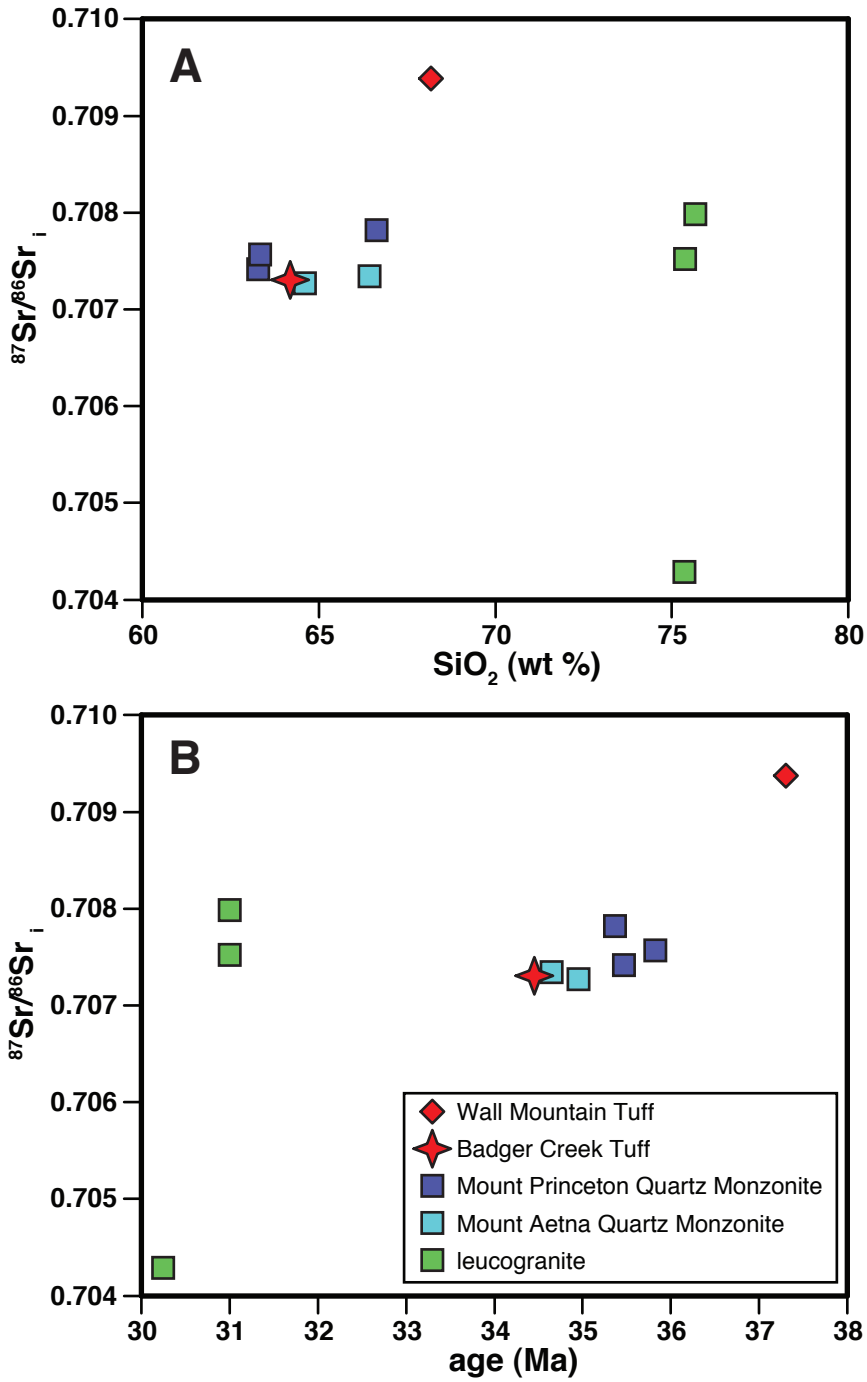

Figure 6 $^{87}Sr/^{86}Sr_i$ plotted against SiO_2 (A). $^{87}Sr/^{86}Sr_i$ plotted against age (B) of the sample (this study; Zimmerer and McIntosh in prep) or Ar/Ar geochronology (Wall Mountain Tuff; Zimmerer and McIntosh in prep).

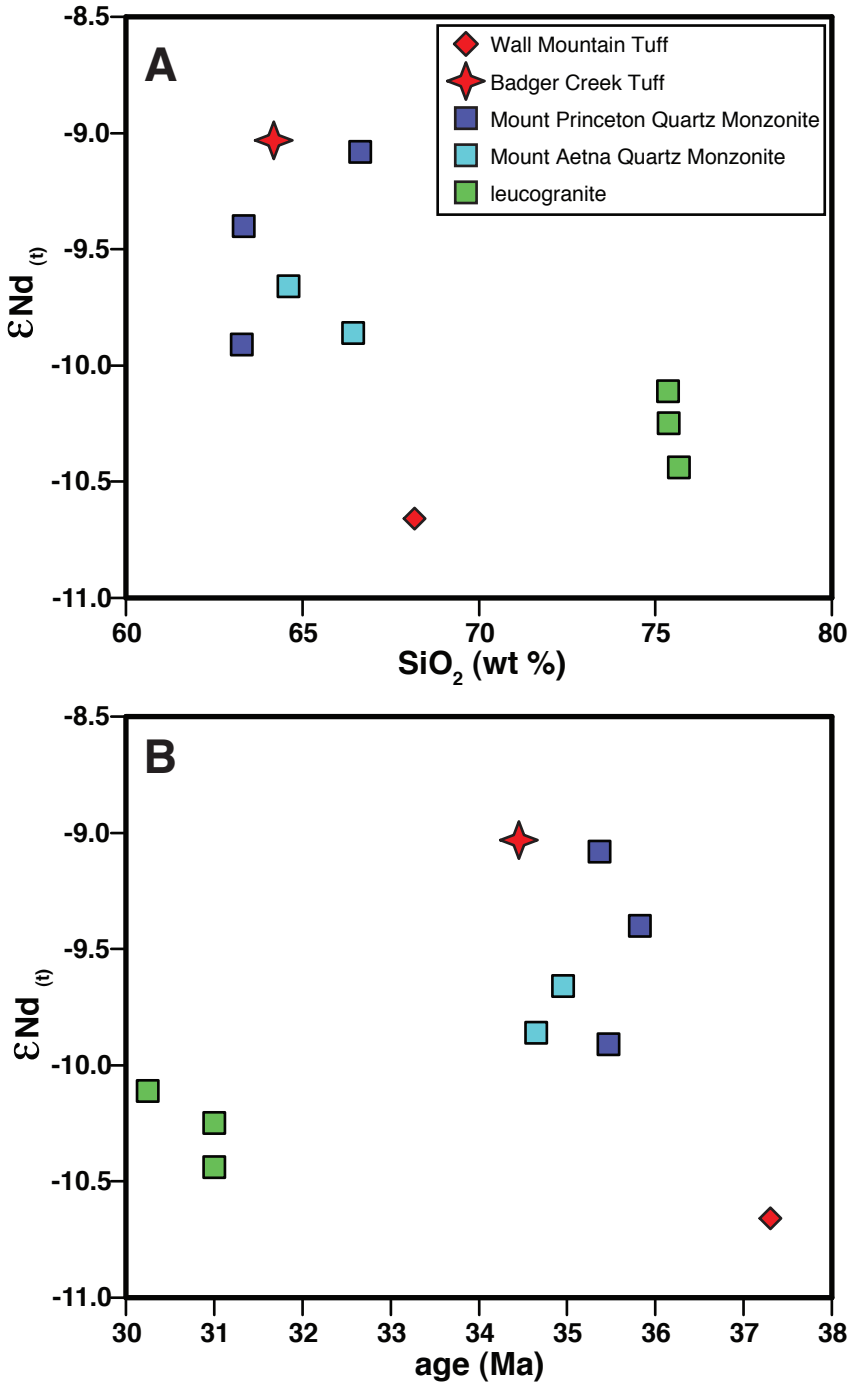

Figure 7 $\varepsilon Nd_{(t)}$ plotted against SiO_2 (A). $\varepsilon Nd_{(t)}$ plotted against age (B) of the sample (this study; Zimmerer and McIntosh in prep) or Ar/Ar geochronology (Wall Mountain Tuff; Zimmerer and McIntosh in prep).

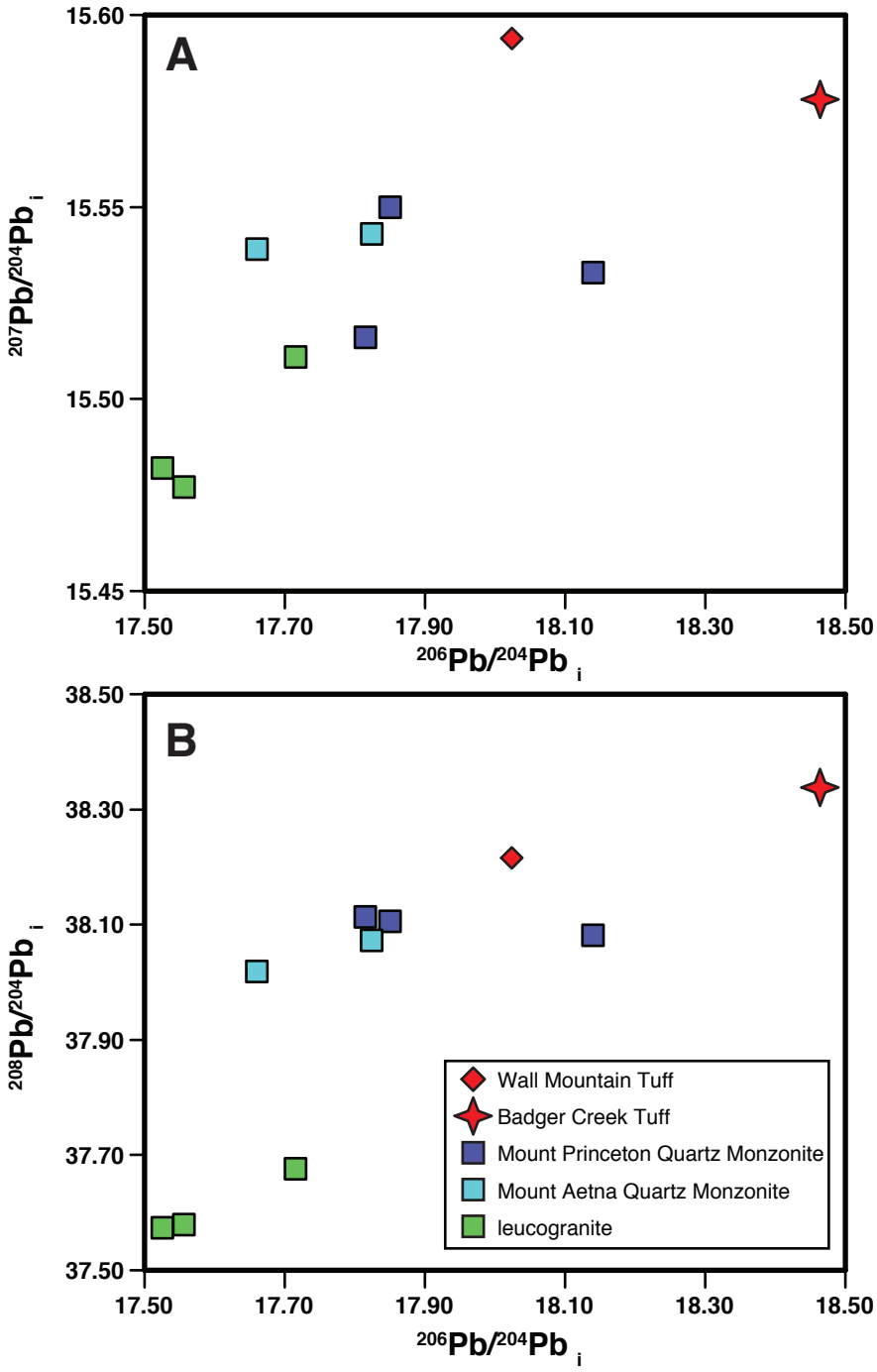

Figure 8 $^{208}Pb/^{204}Pb_i$ plotted against $^{206}Pb/^{204}Pb_i$ (A) and $^{207}Pb/^{204}Pb_i$ plotted against $^{206}Pb/^{204}Pb_i$ (B) for quartz monzonites, leucogranites, Badger Creek Tuff and the Wall Mountain Tuff.

from 38.02 to 38.11) is slightly less radiogenic than the two tuffs (Fig. 8). The leucogranites have significantly less radiogenic Pb isotopic compositions than the intermediate composition portion of the batholith ($^{206}Pb/^{204}Pb$ from 17.53 to 17.72, $^{207}Pb/^{204}Pb$ from 15.48 to 15.51 and $^{208}Pb/^{204}Pb$ from 37.57 to 37.68). Calculated initial whole rock Pb isotopic ratios are in agreement with feldspar Pb isotopes from similar units (Stein 1985).

Hf isotopic compositions of zircon

The range in $\varepsilon Hf_{(t)}$ obtained from zircon from the Wall Mountain Tuff is -11.14 to -17.14 (Table 3; Fig. 9) and the weighted mean is -12.94 with a MSWD of 3.10. Excluding the most negative $\varepsilon Hf_{(t)}$ value of -17.14 (obtained from an inherited core) yields a weighted mean of 12.59 (MSWD = 1.67) that we accept as the magmatic value. The Mount Princeton and Mount Aetna Quartz Monzonite zircons yielded a total range in $\varepsilon Hf_{(t)}$ from -9.43 to -13.92 (Fig. 9). The range in weighted mean $\varepsilon Hf_{(t)}$ for individual Mount Princeton Quartz Monzonite samples is -11.68 to 12.04 and for the Mount Aetna Quartz Monzonite samples it is -12.46 to -12.49 (Fig. 9). Zircons from the tuff dike yield a similar weighted mean (-12.73) as the Mount Aetna Quartz Monzonite (Fig. 9). The weighted mean for the Badger Creek Tuff is -11.36. The 3 leucogranite samples all have less negative weighted means, which range from -9.59 to -10.54 and the overall range from individual zircons in the leucogranite samples is -7.23 to -13.10 (Fig. 9).

U/Pb zircon geochronology

Zircons from dated samples contain few inclusions and lack visible inherited cores. All fractions reported are concordant within uncertainty (considering analytical and decay-constant uncertainties; Table 4) after the application of a Th correction. We use the weighted mean $^{206}Pb/^{238}U$ age as the best estimate for the crystallization age of the samples (Fig. 10).

Pooling zircons into multigrain fractions can compress the spread in data which can produce precise, but inaccurate, ages (Renne et al. 2006) if there is inheritance or Pb-loss in individual zircons. In addition, when dating an eruption event using U/Pb zircon data it is

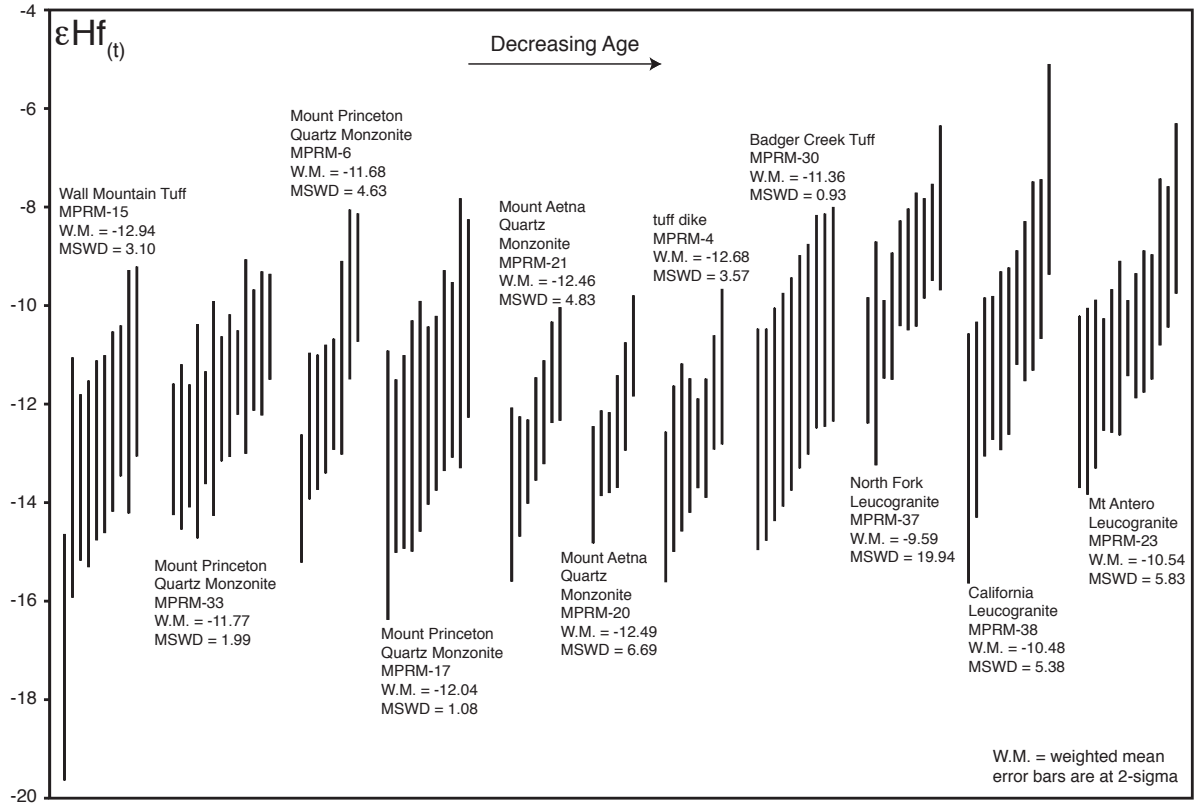

Figure 9 LA-ICP-MS Hf-in-zircon analyses for plutonic rocks from the Mount Princeton batholith and the Wall Mountain Tuff, Badger Creek Tuff, and tuff dike. Samples are ordered from oldest to youngest based on ages from this study and Zimmerer and McIntosh (in prep).

important to pinpoint the youngest zircon growth, which mandates the use of single grains or tips of grains (Crowley et al. 2007). However, we adopted a multi-grain analytical strategy because we were generally concerned with zircon growth during the crystallization history of the magmas; larger fractions helped circumvent the problem of low U concentrations in sampled zircons. We are confident that our weighted mean $^{206}Pb/^{238}U$ ages are not skewed by Pb-loss due to the chemical abrasion pre-treatment procedure, which has been convincingly demonstrated by prior studies to eliminate zircon domains affected by Pb-loss (Mundil et al. 2004; Mattinson 2005). Moreover, our interpretations do not hinge on deciphering the growth systematics of individual zircon grains.

Wall Mountain Tuff

One sample from the densely welded Wall Mountain Tuff (MPRM-15; Fig 1) was collected for zircon geochronology. All U/Pb data that was obtained for this sample was normally discordant and produced a poorly-defined mixing array between approximately 37 Ma and approximately 1.4 Ga. Because the new zircon growth around 37 Ma incorporated very little U, the older, radiogenic Pb-rich component dominated the Pb signal. No zircon age is interpreted for this sample.

Mount Princeton Quartz Monzonite

Three samples from the Mount Princeton Quartz Monzonite units were analyzed (MPRM-6, MPRM-17, and MPRM-33; Fig. 2). MPRM-33 was collected from close to the structural top of the batholith in one of the border units. Zircons from MPRM-33 have low [U] resulting in low radiogenic Pb:common Pb ratios. Six concordant fractions yield a weighted mean $^{206}Pb/^{238}U$ age of 35.80 ± 0.09 Ma (Fig. 10). MPRM-6 was collected outside of the Mount Aetna collapse structure from the interior unit of the Mount Princeton batholith. The weighted mean $^{206}Pb/^{238}U$ age for seven concordant fractions is 35.47 ± 0.07 Ma (Fig. 10). MPRM-17 was collected inside the Mount Aetna collapse structure in a porphyritic portion of the Mount Princeton Quartz Monzonite which outcrops as a semi-continuous horizon

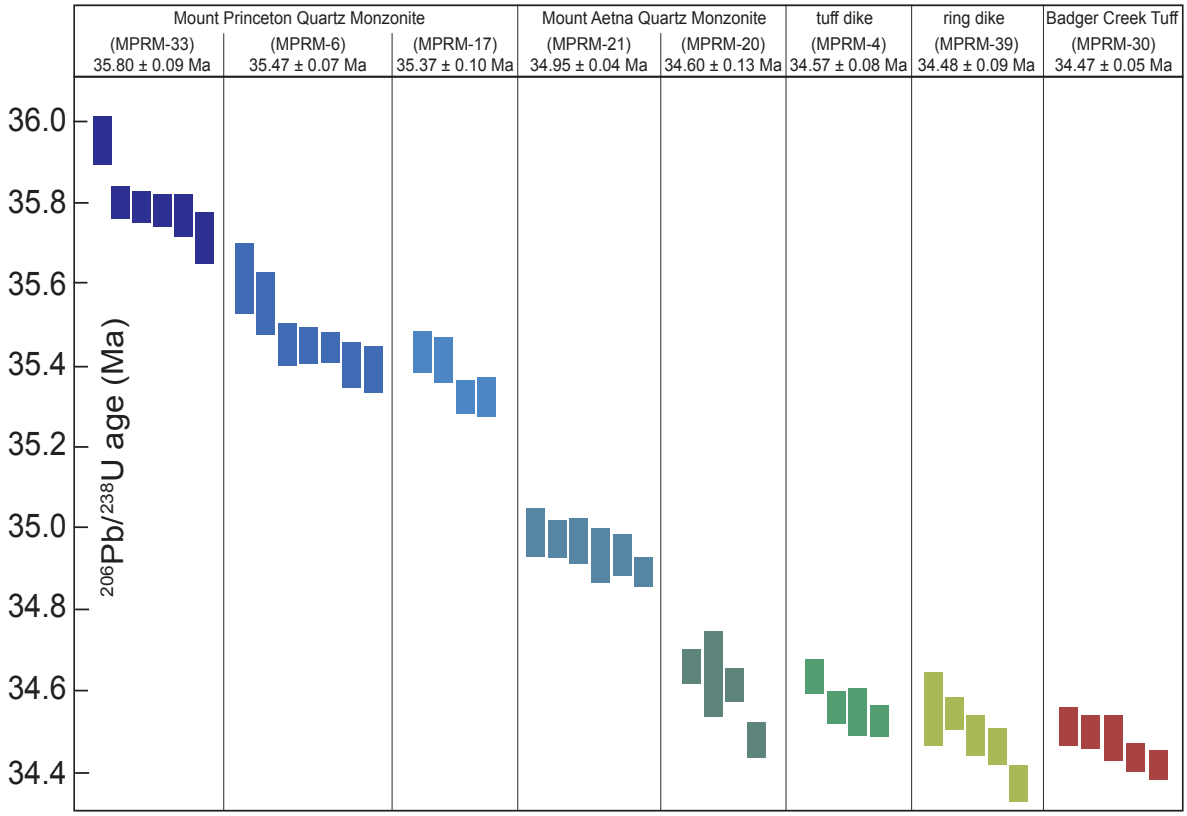

Figure 10 The $^{206}Pb/^{238}U$ ages for zircon from the Mount Princeton batholith and Badger Creek Tuff. Data for all samples are concordant within uncertainty and are corrected for initial Th disequilibrium. Samples are plotted in order of decreasing mean age and fractions are plotted in order of decreasing age for each sample.

between the interior unit and border (roof) units (Fig. 2). MPRM-17 yields a weighted mean $^{206}Pb/^{238}U$ age of 35.37 ± 0.10 Ma (Fig. 10).

Mount Aetna Quartz Monzonite

Two samples from the Mount Aetna Quartz Monzonite were analyzed (MPRM-20 and MPRM-21; Fig. 2). MPRM-21 was collected from the porphyritic portion of the intrusion and yields a weighted mean $^{206}Pb/^{238}U$ age of 34.95 ± 0.04 Ma (Fig. 10). MPRM-20 was collected from the fine-grained portion of the intrusion and yields a weighted mean $^{206}Pb/^{238}U$ age of 34.60 ± 0.13 Ma (Fig. 10).

Tuff dike

One sample (MPRM-4; Fig 2) from the altered tuff dike located north of the batholith was collected and analyzed. Data from four concordant fractions yield a weighted mean $^{206}Pb/^{238}U$ age of 34.57 ± 0.08 Ma (Fig. 10).

Northern ring dike

One sample from the northern ring dike (MPRM-39; Fig. 2) was collected and analyzed. Five concordant fractions give a weighted mean $^{206}Pb/^{238}U$ age of 34.48 ± 0.09 Ma (Fig. 10).

Badger Creek Tuff

One sample from the outflow of the Badger Creek Tuff (MPRM-30; Fig. 1) was collected and analyzed. Five concordant fractions yield a weighted mean $^{206}Pb/^{238}U$ age of 34.47 ± 0.05 Ma (Fig. 10).

Mount Antero Leucogranite

One sample from of the Mount Antero Leucogranite (MPRM-23; Fig. 2) was analyzed and 3 concordant fractions give a weighted mean $^{206}Pb/^{238}U$ age of 30.25 ± 0.10 Ma.

DISCUSSION

Origins of the Mount Princeton magma system

Farmer and DePaolo (1984) listed two possibilities for the source of metaluminous Cenozoic magmas in central Colorado based on Nd and Sr isotopic ratios: 1) partial melting of mafic lower crust and 2) interaction of mantle-derived melts with felsic lower crust. Based on Nd isotopic ratios and REE concentrations Stein and Crock (1990) proposed that the metaluminous quartz monzonites in the Colorado Mineral Belt were generated by partial melting of the lower crust with limited, if any, mantle input. Our initial isotopic ratios (Figs 6, 7, 8, 9) agree with previously obtained values (Stein 1985; Campbell 1994) for rocks from the Mount Princeton magmatic center. Because young lower crust and lithospheric mantle are difficult to distinguish isotopically we infer that the source of the magmas was likely lower crust based on the lack of mafic magmas produced at the Mount Princeton magmatic center. However, the nature of the lower crust was likely modified by input from the lithospheric mantle throughout the history of Cenozoic magmatism.

Ages of the tuffs

Pervasive inheritance problems precluded the possibility of determining a precise U/Pb zircon age for the Wall Mountain Tuff. Consequently, we accept the Ar/Ar age of 37.25 ± 0.08 Ma determined by Zimmerer and McIntosh (in prep) as the best estimate for the eruption age. The age of the Wall Mountain Tuff is sufficiently greater than any of the other units we discuss here that the uncertainty associated with comparing U/Pb and Ar/Ar ages is insignificant.

The Badger Creek Tuff yielded zircons with simple systematics resulting in a weighted mean $^{206}Pb/^{238}U$ age of 34.47 ± 0.05 Ma (Fig. 10). This age agrees with the sanidine Ar/Ar eruption age of 34.26 ±.06 Ma (Zimmerer and McIntosh in prep) when uncertainties in the decay constants are considered.

The contrast between U/Pb zircon crystallization ages and Ar/Ar sanidine eruption

ages is highly variable (see review by Costa (2008)) for different magmatic systems and does not appear to scale with eruption volume (Reid 2008). Whereas some ignimbrites show minimal discrepancies of less than 15% of the age (Reid and Coath 2000; Bindeman et al. 2001; Simon and Reid 2005; Crowley et al. 2007) other ignimbrites have discrepancies greater than 15% and up to 50% of the age (Brown and Fletcher 1999; Schmitt et al. 2003). The variable ages in eruptive units is usually attributed to magma residence, indicating a long-lived crystal-liquid system capable of precipitating zircon over hundreds of thousands of years; however, remobilization of previously solid material is also possible. The 0.6% discrepancy between the U/Pb and the Ar/Ar for the Badger Creek Tuff is insignificant for interpretations made here. In order to compare equivalent ages we accept the U/Pb age of the tuff for discussion below.

Assembly of the Mount Princeton Quartz Monzonite

The Mount Princeton plutons are all classified as quartz monzonite but there is textural and chemical variability that led Shannon (1988) to distinguish multiple phases. Although we only dated three samples of the quartz monzonite, our sampling strategy was designed to maximize spatial and textural coverage of the plutons. In addition, Zimmerer and McIntosh (in prep) dated samples from a broader geographic area of the Mount Princeton Quartz Monzonite. They interpret eight samples ranging in Ar/Ar biotite age from 35.78 to 35.23 Ma to represent the interval of crystallization of the Mount Princeton Quartz Monzonite. Biotite ages and zircon ages agree within uncertainty for mapped units defined by Shannon (1988), which is to be expected for fast cooling epizonal plutons. Therefore, we accept the range in zircon ages to be indicative of the assembly time for the Mount Princeton Quartz Monzonite, approximately 430 ka.

The oldest sample dated from the Mount Princeton Quartz Monzonite (MPRM-33, 35.80 Ma; Fig. 10) was collected at the top of the exposed pluton in the border unit (Fig. 2). This is considered to be close to the top of the intrusive sequence on the basis of the textural variability of the border units and restricted exposure in the dropped section inside the Mount

Aetna caldera (Shannon 1988). The oldest biotite ages (35.78 and 35.72 Ma; Zimmerer and McIntosh in prep) were obtained from another border (roof) unit that is also interpreted to be close to the top of the batholith (Shannon 1988). The geochronologic data support the hypothesis that magma cooled and crystallized adjacent to the roof and subsequent intrusions crystallized below the upper border units. The data may also be consistent with top-down construction of the pluton (Menand 2008; 2011); however, the limited data are not necessarily as convincing for this as documented elsewhere (Michel et al. 2008; Morgan et al. 2008; Tappa et al. 2011).

The sample that yielded the intermediate age for the Mount Princeton Quartz Monzonite (MPRM-6; 35.47 Ma; Fig. 10) is from the largest mapped unit (Fig. 2) of Shannon (1988), referred to as the "interior unit." Biotite ages for samples from this unit range from 35.56 to 35.23 Ma (Zimmerer and McIntosh in prep), indicating that zircon crystallization in part of the unit preceded that recorded in the sample we dated (35.47 Ma), probably by 100 to 200 ka. We interpret the increased scatter in the data for MPRM-6 (relative to the other samples in this study) to be the result of incorporation of zircon from slightly older portions of the intrusive system as inferred for many other plutons (e.g. Miller et al. 2007). The oldest fraction from MPRM-6 yields a $^{206}Pb/^{238}U$ age of 35.61 Ma (Fig. 10), which we suggest is the best estimate for the beginning of crystallization of the interior unit of the Mount Princeton Quartz Monzonite.

The youngest sample of the Mount Princeton Quartz Monzonite (MPRM-17; 35.37 Ma; Fig. 10) is from the porphyritic facies of the pluton. Its age is the same, within uncertainty, of the sample dated from the interior unit (MPRM-6). However, unlike other dated samples, Ar/Ar biotite ages for the porphyritic facies are significantly younger (31.49 to 30.80 Ma; Zimmerer and McIntosh in prep) than the zircon age for this unit. Zimmerer and McIntosh (in prep) interpret the biotite ages to represent resetting of the Mount Princeton Quartz Monzonite during emplacement of the younger leucogranites (31-30 Ma). The thin, wispy outcrop pattern of the porphyritic facies (Fig. 2) and the young biotite ages leads us

to suggest that these may represent conduits for fluids escaping during emplacement of the leucogranites. Furthermore, the pulses of heat and/or volatiles (Glazner et al. 2011) that reset the biotite ages may be responsible for textural coarsening (Higgins 1999; Johnson and Glazner 2010) in the porphyritic facies.

Given the zircon age range of 430 ka, the area of exposure of 450 km^2 (Shannon 1988) and the exposed vertical thickness of 1.5 km, we calculate an integrated magma flux of 0.0016 km^3/a for the Mount Princeton Quartz Monzonite. Thermal models indicate that magma flux of at least 0.01 km^3/a is necessary to produce enough magma to feed a super eruption of at least 450 km^3 (Annen 2009). Thus, the integrated flux is too low to produce a super eruption, but magma flux may have been much higher over shorter timescales. However, the lack of ignimbrites in the Thirtynine Mile volcanic field (McIntosh and Chapin 2004) within the age range for the Mount Princeton Quartz Monzonite (Fig. 11) indicates that no known ignimbrite eruptions were associated with the construction of the Mount Princeton Quartz Monzonite.

Assembly of the Mount Aetna Quartz Monzonite

The Mount Aetna Quartz Monzonite is the intrusion, or set of intrusions, closest in age to the Badger Creek Tuff, and locally cuts the intracaldera tuff (Toulmin and Hammarstrom 1990). The two dated samples from the Mount Aetna Quartz Monzonite have varied textures and give distinctly different age results. Zircon fractions from the porphyritic sample (MPRM-21) produced consistent results: a weighted mean $^{206}Pb/^{238}U$ age of 34.95 Ma ±0.04 Ma (Fig. 10), with little observed inheritance. In contrast, zircon from the fine-grained sample (MPRM-20) show significant age spread yielding large uncertainty in the weighted mean $^{206}Pb/^{238}U$ age (34.60 ± 0.13 Ma). We assume that Pb-loss has been mitigated by chemical abrasion (Mundil et al. 2004; Mattinson 2005) and propose that the older fractions in the fine-grained sample represent antecrysts (Miller et al. 2007). Therefore, the age of the youngest fraction (34.48 Ma) is likely closest to the true emplacement age.

We are reluctant to make conclusions about whether the fine-grained sample (MPRM-

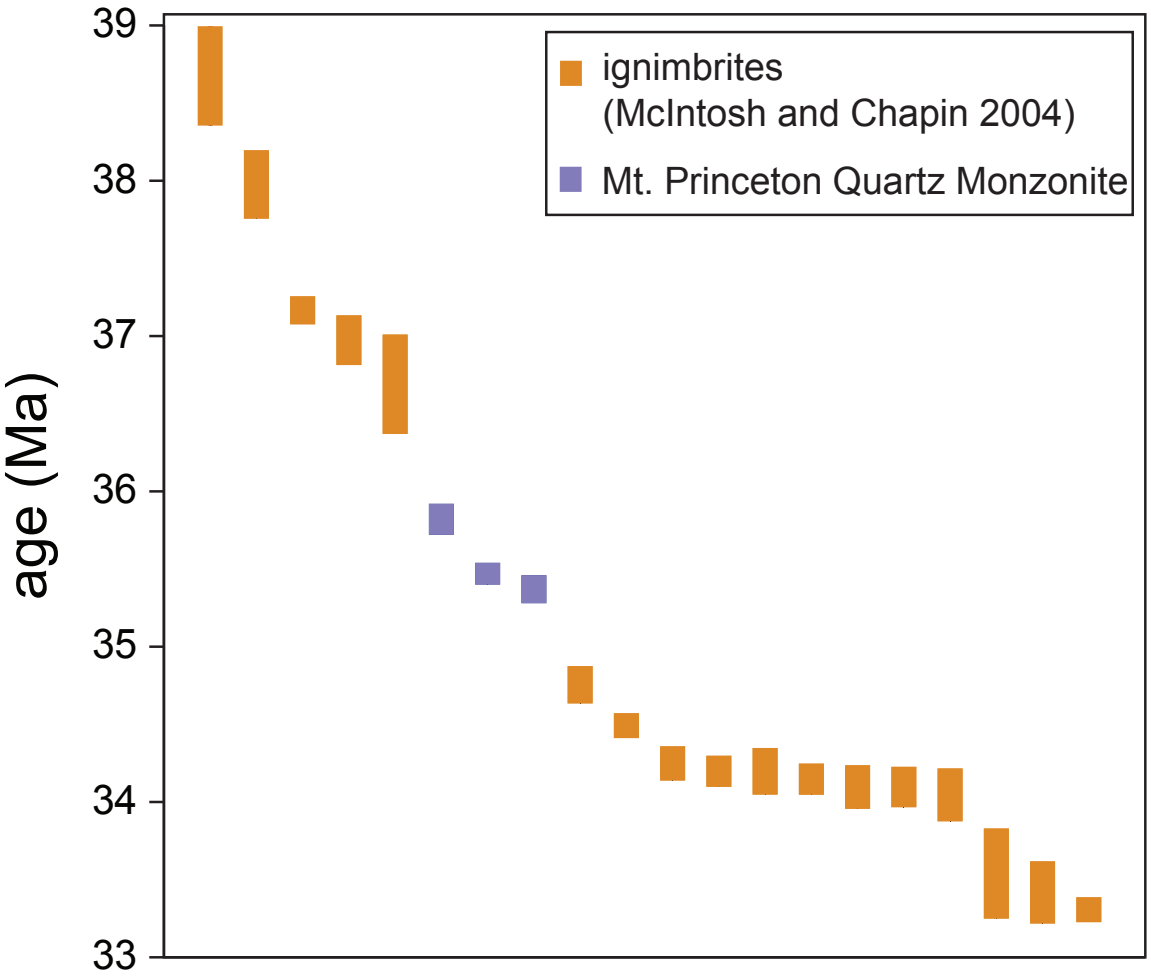

Figure 11 Plot of Ar/Ar sanidine ages (McIntosh and Chapin 2004; recalculated using FC-2 = 28.201 Ma, Kuiper et al. 2008) for ignimbrites preserved in the Thirtynine Mile volcanic field and zircon $^{206}Pb/^{238}U$ ages from the Mount Princeton Quartz Monzonite (MPRM-33, MPRM-6, MPRM-17).

20) is older or younger than the Badger Creek Tuff due to the large spread in fraction ages (inheritance) and the large uncertainty on the pooled age. However, U/Pb data from the porphyritic sample (MPRM-21) indicate the zircon crystallized approximately 500-700 ka before zircon crystallization in, and eruption of, the tuff, and field evidence indicates that the Mount Aetna pluton elsewhere cross cuts the tuff. The two most likely explanations for the disagreement between the zircon age from the porphyritic sample and the field relationships are: 1) zircon in the porphyritic Mount Aetna Quartz Monzonite is dominantly remobilized zircon from earlier intrusions (Klemetti and Cooper 2007), or 2) the Mount Aetna Quartz Monzonite stock is a complex, diachronous set of intrusions that accumulated over at least 500 ka.

Remobilization of the 34.95 Ma Aetna pluton 500-700 ka after intrusion is consistent with the observation that it locally cuts the Badger Creek Tuff. In this interpretation, the Aetna pluton is the penecontemporaneous source of the Badger Creek tuff, and the fine-grained facies of the pluton is the chilled margin of the porphyritic facies (Shannon 1988). However, it is difficult to reconcile this interpretation with the 1) lack of evidence for young zircon growth in the porphyritic facies, particularly since the presumed chilled margin is dominated by young zircon growth, and 2) lack of 34.95 Ma zircon in either the chilled margin or the Badger Creek Tuff. Although the spread in the U/Pb data for the fine-grained sample may be related to mixing of 34.95 Ma zircons with young zircon (< 34.4 Ma) there is no evidence for a 34.95 Ma component in the Badger Creek Tuff U/Pb data.

Thus, we prefer a model that involves incremental assembly of the Mount Aetna Quartz Monzonite over a 500 ka period that spans the eruption of the Badger Creek Tuff. We suggest that the intracaldera tuff was deposited on top of the Mount Aetna Quartz Monzonite and later intrusions were emplaced at the rheologic boundary between the tuff and the quartz monzonite, locally remobilizing and annealing the previous contact. Additional geochronology of the Mount Aetna Quartz Monzonite from the contact is needed to fully test these models.

Relation of the Wall Mountain Tuff to the Mount Princeton batholith

The Wall Mountain Tuff (37.25 Ma; Zimmerer and McIntosh in prep) is the largest rhyolitic ignimbrite preserved in the Thirtynine Mile volcanic field. Its size (1,000 km^3), inscrutable geochronology (Shannon 1988; Friedrich et al. 1998) and paleovalley fill distribution led many to suggest that the source of the ignimbrite was the Mount Princeton batholith (Tweto 1979; Shannon 1988; Lipman 2007). Our geochronology for the Mount Princeton batholith (35.82 to 30.25 Ma) indicate that presently exposed units of the batholith are too young to be directly related to the genesis of the Wall Mountain Tuff. In addition, our whole-rock isotopic analyses confirm the assertion made by Campbell (1994) on the basis of Sr isotopes, that the Wall Mountain Tuff had a different source than the Mount Princeton Quartz Monzonite.

Shannon (1988) and Lipman (2007) predicted that the relationship between the Mount Princeton Quartz Monzonite and the Wall Mountain Tuff was strong evidence for significant crystal/liquid fractionation in the upper crust because the Wall Mountain Tuff is more felsic than the Mount Princeton Quartz Monzonite. Lipman (2007) suggested that differentiation in the upper crust produced felsic caps that erupted and are now preserved as ignimbrite sheets in the Southern Rocky Mountain volcanic field and that some plutons represent the more mafic crystal cumulates left behind in the crust. At least in the case of the Wall Mountain Tuff and the Mount Princeton batholith there is no evidence to support this hypothesis: geochronologic and geochemical data contradict any direct connection between the tuff and the batholith.

Plutonic remnants of the Wall Mountain Tuff

Whole rock Sr and Pb isotopic ratios for the Wall Mountain Tuff are akin to magmas sourced farther into the NE-SW trending Colorado Mineral Belt than the Mt. Princeton batholith. However, the Twin Lakes batholith to the north, which displays a large range in crystallization ages (63 – 39 Ma) that approaches the age of the Wall Mountain Tuff

(Feldman 2010), appears to be too far north to reconcile with the paleovalley fill of the tuff. Another potential source location is to the west, in the Elk and West Elk Mountains. However, present data on multiple stocks in the Elk and West Elk Mountains indicate that the magmatism in this area post-dates the Wall Mountain Tuff by several million years (Obradovich et al. 1969; Garcia 2011). Thus, there are no known plutonic equivalents of the tuff. Furthermore, if the source caldera for the Wall Mountain Tuff was located in the same geographic area as the Mount Princeton batholith as suggested by geomorphic data, it must have been at a structurally higher level that was completely eroded shortly after the caldera forming eruption.

To evaluate the possibility that the Wall Mountain Tuff was derived through shallow fractional crystallization from plutonic rocks eroded from above the exposed Mount Princeton batholith, we estimate the volume of plutonic rock that must have been removed. The best estimate for the crystallization depth of the Mount Princeton Quartz Monzonite is 3 km (Hammarstrom and Zen 1986), which establishes a minimum thickness of the Wall Mountain magma system. The maximum calculated exhumation rate for the Mount Princeton Quartz Monzonite is 1.5 mm/a (Hammarstrom and Zen 1986), which is based on the deposition of the Badger Creek Tuff on the Mount Princeton Quartz Monzonite at 34.3 Ma. If this rate is applied to the amount of time between the eruption of the Wall Mountain Tuff (37.3 Ma) and the oldest age of the Mount Princeton Quartz Monzonite (35.8 Ma) then an additional 2.25 km of the magma system could have possibly been present at the time of the eruption of the Wall Mountain Tuff. This places an upper limit on the thickness of the Wall Mountain magma system of 5.25 km. Lipman (2007) estimated the area of the Wall Mountain Tuff caldera at 350 km^2 which establishes a upper estimate of total magma volume of 1,800 km^3. The eruptive volume of the tuff is estimated to be 1,000 km^3, leaving a maximum residual (but now eroded) pluton volume of 800 km^3. Thus the greatest intrusive extrusive ratio calculated from this model is 0.8:1, significantly lower than modern estimate for caldera forming systems (Smith 1979; Spera and Crisp 1981; White et al., 2006). Furthermore, we

estimated all variables above to maximize pluton volume. Thus, if the Wall Mountain Tuff was derived from above the presently exposed Mount Princeton batholith, we suggest that it was fairly efficiently evacuated from the upper crust leaving behind little magma to crystallize as plutons.

Origin of the Badger Creek Tuff

The trap-door style Mount Aetna caldera formed during the eruption of the Badger Creek Tuff and a network of ring dikes and tuff dikes (cutting Precambrian wall rocks) are correlated with the eruption of the tuffs (Shannon 1988; Toulmin and Hammarstrom 1990). Zircon U/Pb ages for the ring dike (34.48 ± 0.09 Ma), tuff dike (34.57 ± 0.08 Ma) and fine-grained Mount Aetna Quartz Monzonite (34.60 ± 0.13 Ma) overlap with the zircon age of the Badger Creek Tuff (34.47 ± 0.05 Ma; Fig. 10) and are all older than the sanidine Ar/Ar eruption age of 34.26 ± 0.06 Ma for the Badger Creek Tuff (Zimmerer and McIntosh in prep).

If uncertainties in the U and K decay constants are propagated through the error calculation, the zircon ages for the dikes and fine-grained Mount Aetna Quartz Monzonite and the Badger Creek Tuff overlap at 2σ with the sanidine Ar/Ar age for the Badger Creek Tuff. The older U/Pb age for the Badger Creek Tuff compared to the Ar/Ar age may be related to an inaccurate calibration of the U/Pb and K/Ar systems (Kuiper et al. 2008; Renne et al. 2010) or pre-eruption zircon residence. Another possibility is that the Badger Creek Tuff was remobilized prior to eruption, similar to what has been proposed for the Fish Canyon Tuff (Bachmann and Bergantz 2003). In this model the high crystallinity and old zircon grains of the Badger Creek Tuff would be the result of partial melting of a near-solid crystal mush by injection (± gas sparging) of a mafic magma just prior to eruption (Bachmann and Bergantz 2003, 2006). However, there is no field evidence for the addition of mafic magmas to the Badger Creek magma chamber and the high crystallinity could be the result of rapid decompression crystallization upon ascent (Blundy and Cashman 2005). Thus, we propose that the age discrepancy is likely a combination of inaccurate calibration between the U/Pb and K/Ar

systems and prolonged zircon growth in the magma chamber.

Relationship between the Badger Creek Tuff and the Mount Princeton batholith

Despite the discrepancy with the U/Pb and Ar/Ar ages, the fine-grained Mount Aetna Quartz Monzonite, ring dike and tuff dike all have $^{238}U/^{206}Pb$ zircon ages equivalent to the Badger Creek Tuff, consistent with the correlation of the dikes with the Badger Creek Tuff by Shannon (1988). The fine-grained portion of the Mount Aetna Quartz Monzonite is chemically similar to the Badger Creek Tuff (Figs. 3, 4, 5); however, a large portion of the quartz monzonite from the batholith is chemically similar to the Badger Creek Tuff (Figs. 3, 4, 5). The ring dike is slightly more felsic than any analyzed sample of the Badger Creek Tuff (Fig. 3). Chemical modification of the ring dike by late stage magmatic fluids travelling through the ring fracture could have altered the chemistry, or the ring dike may represent a more felsic zone of the Badger Creek magma chamber that is not observed in the sampled portions of the intracaldera tuff or the outflow sheet. The tuff dike is highly altered so it is not possible to test whether it is chemically similar to the Badger Creek Tuff.

Comparison of the erupted portion of the Badger Creek magma chamber and the portion that crystallized in the crust indicates shallow-crustal crystal-liquid fractionation was not an important process in the genesis of the Badger Creek Tuff and related intrusions. Crystal-liquid fractionation should produce predictable depletions in the liquid of elements that are concentrated in early crystallizing phases (e.g., Sr, Ba, Zr and Eu). Conversely, the liquid should be enriched in incompatible elements including Rb, and should have a lower Zr/Hf ratio due to zircon fractionation. None of these predicted variations are observed in the Badger Creek Tuff and related intrusions. Instead, the erupted material is chemically similar to the intrusions and does not show any evidence of representing a liquid that was extracted from a crystal mush. Incorporation of crystals from a crystal mush into the tuff could have muted the fractionation signal but it is unlikely that the signal would be completely obscured.

Implications for connections between plutons and ignimbrites

Zircon U/Pb ages from plutonic rocks from the Mount Princeton batholith and associated ignimbrites indicate a temporal disconnect between pluton emplacement and caldera-forming eruptions (Fig. 11). Because the caldera system is defined by eruption of two significant-volume ignimbrites, it does not fit neatly into the waxing/ignimbrite/waning stage model defined by Lipman (2007). What is clear, however, is that the majority of the batholith was emplaced between eruption of the Wall Mountain Tuff and the Badger Creek tuffs, and that there is no identified ignimbrite in the region that is the same age as the most volumetrically significant plutonic rocks (Fig. 11).

Because the plutonic rocks in the Princeton batholith region are not temporally associated with large-volume volcanism, the relatively low flux of magma that characterizes intra-ignimbrite magmatism - including waxing and waning stages elsewhere (e.g. Tappa et al. 2011), apparently favors pluton construction. According to this hypothesis, low-flux magmas generally stall in the upper crust and build plutons incrementally. These plutons most likely support small to moderate sized, steady state eruptions of magma (e.g. Claiborne et al. 2010) with no caldera formation. In contrast, the high magma flux modeled (Annen 2009) for super eruptions and documented by zircon geochronology of ignimbrites (Schmitz and Bowring 2001; Simon and Reid 2005; Crowley et al. 2007) results in nearly complete eruption of the rising magma (Tappa et al. 2011). Importantly, if ignimbrite eruption dominates the volume of rock preserved in the volcanic record, but is essentially absent from the plutonic record, the existing estimates of the intrusive:extrusive rock ratio (Smith 1979; Spera and Crisp 1981; White et al. 2006) likely reflect long-term averages, and have no relevance to magma chamber dynamics. The temporal disconnect between accumulation of large plutons and eruption of large ignimbrites means that the volume of intrusive rock preserved in one environment cannot be used to estimate the volume of extrusive rock that should be preserved in the other, and vice versa (e.g. Lipman 2007; de Silva and Gosnold 2007).

Another potentially significant corollary of this hypothesis is that it predicts that old

magmatic centers (> 50Ma) will preserve an apparent disconnect between episodes of plutonism and volcanism because ignimbrites will dominate the preserved volcanic record, and there will be little, if any, temporally correlative plutonic rocks. For example, Glazner (1991) noted a mismatch in the timing of volcanic and plutonic episodes in the Mesozoic Sierra Nevada arc. There, the sparse volcanic rocks that are preserved are dominated by ignimbrites (e.g. Saleeby et al. 1990; Barth et al. 2011) that erupted between episodes of significant pluton assembly. He attributed this mismatch to the angle of plate convergence, with episodes of oblique convergence favoring plutonism because plutons could intrude in releasing bends along strike-slip faults. Here we propose a tectonic connection to the mismatch as well, but suggest it may be tied to changes in magma flux. During periods of low flux, plutonism dominates. During periods of high flux, ignimbrite eruption, which leaves almost nothing in the plutonic record, dominates.

If large volcanic eruptions are not supported by large pluton volumes, then the bulk geochemistry of ignimbrites, and the origin of zonation in plutonic rocks and ignimbrites need not be the result of shallow crustal processes. Clemens et al. (2010) attributed chemical variations seen at varied scales in silicic plutons and volcanic deposits to changes (physical and chemical) in the lower crust source through time. This hypothesis is supported by the work of Tappa et al. (2011) who showed that the silicic cap of the zoned Rio Hondo pluton could not be liquid derived from deeper, more mafic portions of the pluton because the silicic cap predated the more mafic parts of the pluton. These authors hypothesized that the zoning was a result of temporal variation in the composition of the magmas feeding the shallow plutons. Similar zoning could form in an ignimbrite if the flux of magma from the source was high enough (Tappa et al. 2011).

Finally, the model presented distinguishes the plutonic rock record from the ignimbrite record. However, it simultaneously reinforces the temporal and chemical connections between the plutonic rock record and "typical" volcanic rocks. Although eruption of 5000 km^3 ignimbrites is geologically spectacular, low flux eruptions likely dominate at magmatic

centers (Crisp 1984). Temporally, the waxing and waning stages of magmatism dominate even in the ignimbrite-rich Southern Rocky Mountain volcanic field. Although the waxing and waning magmas may be poorly represented (relative to the ignimbrites) in older magmatic centers, we suggest that their temporal evolution is well preserved in the pluton record. The chemical evolution of the system is also likely recorded in the plutonic material because whole rock chemistry of plutonic rocks and volcanic rocks are not unique (Mills et al. 2008). Thus, for ancient magmatism, the plutonic rock record could provide the best insight into source evolution and, consequently, the chemical evolution of Earth's crust.

CONCLUSIONS

1) Emplacement of large plutons at the Mount Princeton magma center occurred during periods marked by a lack of ignimbrite eruptions (Figs. 10, 11).
2) Small plutons that are coeval with ignimbrite eruption at the Mount Princeton magma center are chemically similar to the ignimbrite (Fig. 5) and show no signs of crystal-liquid separation.
3) Magma flux estimate for the Mount Princeton Quartz Monzonite is 0.0016 km^3/a which is too low to produce super eruptions.
4) The source of the magmas at Mount Princeton migrated from felsic lower crust to mafic lower crust through time.

Table 1 Whole-rock major-element concentrations (wt. %)

Sample name	SiO_2	Al_2O_3	Fe_2O_3(T)	MnO	MgO	CaO	Na_2O	K_2O	TiO_2	P_2O_5	LOI	Total
Mount Princeton Quartz Monzonite												
MPRM-6	63.29	15.27	5.30	0.063	1.78	3.77	3.33	4.35	0.665	0.27	1.70	99.79
MPRM-17	66.63	15.57	4.09	0.080	1.29	3.32	3.48	3.87	0.515	0.21	1.16	100.20
MPRM-33	63.34	15.06	5.70	0.106	2.11	3.63	3.19	4.66	0.773	0.23	1.04	99.83
Mount Aetna Quartz Monzonite												
MPRM-20	66.43	15.97	4.28	0.084	1.22	3.26	3.88	4.04	0.580	0.27	0.71	100.70
MPRM-21	64.61	15.45	4.44	0.086	1.46	3.59	3.71	4.19	0.620	0.34	0.92	99.39
ring dike												
MPRM-39	68.54	14.40	3.39	0.126	0.93	2.00	3.76	4.47	0.436	0.20	1.13	99.38
leucogranite												
MPRM-23	75.35	13.62	1.08	0.066	0.16	0.63	3.81	5.28	0.136	0.05	0.33	100.50
MPRM-37	75.67	13.07	1.13	0.061	0.22	0.62	3.87	4.66	0.135	0.06	0.40	99.91
MPRM-38	75.38	13.10	1.17	0.071	0.18	0.68	3.72	4.80	0.158	0.06	0.22	99.55
Wall Mountain Tuff												
MPRM-15	68.18	14.69	1.42	0.050	0.58	1.20	3.37	6.71	0.457	0.08	1.66	98.39
Badger Creek Tuff												
MPRM-30	64.20	16.33	2.63	0.050	0.81	2.76	3.54	4.45	0.521	0.25	5.37	100.90

Table 1 continued Whole-rock trace-element concentrations (ppm)

Sample name	Sc	Be	V	Cr	Co	Ni	Cu	Zn	Ga	Ge	As	Rb	Sr	Y	Zr	Nb	Mo	Ag	In	Sn	Sb	Cs	Ba
Mount Princeton Quartz Monzonite																							
MPRM-6	10	2	99	< 20	10	< 20	10	40	20	1.5	6	124	491	24.7	199	14.2	< 2	< 0.5	< 0.1	2	1.3	4.6	951
MPRM-17	7	2	74	< 20	11	< 20	10	70	21	1.7	< 5	113	610	21.1	180	16.4	< 2	1.2	< 0.1	2	0.8	2.4	1037
MPRM-33	11	2	109	40	16	20	20	70	21	1.6	< 5	164	463	26.4	287	19.7	< 2	1.2	< 0.1	3	0.7	2.7	957
Mount Aetna Quartz Monzonite																							
MPRM-20	7	3	58	30	6	< 20	20	150	22	1.4	< 5	133	651	24.1	269	20.5	< 2	< 0.5	0.1	30	0.4	2.1	1151
MPRM-21	7	3	73	< 20	10	< 20	20	70	23	1.4	< 5	122	654	20.2	224	16.3	< 2	< 0.5	< 0.1	2	< 0.2	1.4	1074
ring dike																							
MPRM-39	5	3	34	< 20	6	30	50	220	20	1.0	6	145	476	18.3	224	21.1	< 2	2.3	0.1	3	1.2	3.3	1189
leucogranite																							
MPRM-23	4	6	8	< 20	2	< 20	< 10	< 30	23	2.4	< 5	293	111	15.0	109	51.0	< 2	< 0.5	< 0.1	3	0.6	2.8	387
MPRM-37	6	7	9	< 20	2	< 20	< 10	< 30	23	2.6	< 5	393	95	17.2	87	36.6	< 2	< 0.5	< 0.1	8	0.7	4.6	274
MPRM-38	3	5	10	< 20	2	< 20	10	50	21	2.2	< 5	237	124	14.9	121	35.1	< 2	< 0.5	< 0.1	3	0.6	3.0	408
Wall Mountain Tuff																							
MPRM-15	7	3	20	20	2	< 20	< 10	80	20	1.5	< 5	207	221	31.9	487	24.4	< 2	< 0.5	< 0.1	2	0.3	2.7	1319
Badger Creek Tuff																							
MPRM-30	3	3	39	20	8	< 20	20	60	23	2.2	7	145	676	18.9	273	24.1	< 2	1.6	< 0.1	2	0.7	2.1	1544

Table 1 continued Whole-rock trace-element concentrations (ppm)

Sample name	La	Ce	Pr	Nd	Sm	Eu	Gd	Tb	Dy	Ho	Er	Tm	Yb	Lu	Hf	Ta	W	Tl	Pb	Bi	Th	U
Mount Princeton Quartz Monzonite																						
MPRM-6	53.6	97.4	10.2	34.0	6.82	1.490	5.04	0.72	4.0	0.79	2.3	0.348	2.2	0.318	5.4	1.36	0.7	0.72	11	1	22.0	5.68
MPRM-17	46.5	92.2	10.8	38.3	6.77	1.490	4.65	0.68	3.7	0.7	1.98	0.287	1.9	0.311	4.6	1.19	1.2	0.56	108	0.9	22.3	5.71
MPRM-33	74.0	147.0	16.5	55.8	9.32	1.550	6.28	0.92	4.8	0.88	2.56	0.381	2.5	0.392	7.3	1.41	1.9	0.59	22	0.2	32.1	3.34
Mount Aetna Quartz Monzonite																						
MPRM-20	51.2	102.0	13.8	42.8	7.84	1.840	6.2	0.9	4.8	0.86	2.34	0.33	2.1	0.315	7.5	1.59	1.6	0.83	21	2.1	18.5	5.61
MPRM-21	61.6	116.0	12.1	39.4	7.61	1.730	5.11	0.68	3.6	0.69	1.96	0.287	1.8	0.254	6.1	1.5	1.7	1.35	13	0.4	22.7	3.85
ring dike																						
MPRM-39	48.1	99.6	10.6	39.9	7.12	1.520	5.64	0.8	3.8	0.8	2.27	0.379	2.8	0.489	6.6	1.58	3.3	0.95	82	1.4	19.8	5.79
leucogranite																						
MPRM-23	33.7	62.9	6.4	19.4	3.19	0.378	2.2	0.35	2.1	0.42	1.35	0.236	1.8	0.348	4.0	3.57	2.4	1.07	38	0.3	25.7	13
MPRM-37	25.8	50.3	5.4	17.2	3.17	0.363	2.53	0.4	2.3	0.46	1.44	0.249	2.0	0.357	3.5	4.01	2.7	1.31	33	0.1	26.3	12.8
MPRM-38	33.6	63.5	6.7	20.6	3.47	0.432	2.43	0.38	2.2	0.44	1.39	0.242	1.8	0.326	4.2	2.69	1.8	0.93	35	0.3	33.7	12
Wall Mountain Tuff																						
MPRM-15	94.5	178.0	18.8	60.3	11.00	2.060	7.33	1.05	5.7	1.11	3.27	0.478	3.0	0.441	12.1	1.95	1.2	1.87	30	0.5	36.1	8.21
Badger Creek Tuff																						
MPRM-30	67.2	129.0	15.0	52.8	9.30	2.130	6.5	0.88	4.5	0.77	2.05	0.294	1.9	0.302	6.4	1.54	3.5	0.96	35	0.2	17.0	4.26

Table 2 Whole-rock Nd, Pb and Sr isotopic data

Sample name	$^{143}Nd/^{144}Nd$	% S.E.	εNd(t)	$^{206}Pb/^{204}Pb_m$	% S.E.	$^{207}Pb/^{204}Pb_m$	% S.E.	$^{208}Pb/^{204}Pb_m$	% S.E.	$^{206}Pb/^{204}Pb_i$	$^{207}Pb/^{204}Pb_i$	$^{208}Pb/^{204}Pb_i$	$^{87}Sr/^{86}Sr_m$	% S.E.	$^{87}Sr/^{86}Sr_i$
Mount Princeton Quartz Monzonite															
MPRM-6	0.512113	0.0008	-9.90	18.029	0.0052	15.559	0.0052	38.335	0.0052	17.850	15.550	38.106	0.707787	0.0009	0.7074
MPRM-17	0.512151	0.0006	-9.08	17.833	0.0056	15.517	0.0066	38.137	0.0068	17.815	15.516	38.113	0.708088	0.0009	0.7078
MPRM-33	0.512134	0.0006	-9.40	18.140	0.0053	15.533	0.0053	38.251	0.0052	18.087	15.531	38.082	0.708089	0.0010	0.7076
Mount Aetna Quartz Monzonite															
MPRM-20	0.512113	0.0010	-9.86	17.747	0.0035	15.543	0.0033	38.113	0.0032	17.660	15.539	38.019	0.707638	0.0007	0.7073
MPRM-21	0.512125	0.0012	-9.65	17.921	0.0037	15.547	0.0079	38.261	0.0079	17.824	15.543	38.073	0.70754	0.0008	0.7073
leucogranite															
MPRM-23	0.512101	0.0006	-10.11	17.658	0.0057	15.482	0.0058	37.646	0.0061	17.556	15.477	37.579	0.707571	0.0010	0.7043
MPRM-37	0.512085	0.0006	-10.44	17.832	0.0057	15.516	0.0045	37.755	0.0054	17.715	15.511	37.676	0.713257	0.0009	0.7080
MPRM-38	0.512093	0.0006	-10.25	17.628	0.0059	15.487	0.0064	37.668	0.0078	17.525	15.482	37.573	0.709961	0.0009	0.7075
Wall Mountain Tuff															
MPRM-15	0.512072	0.0013	-10.63	18.123	0.0061	15.599	0.0064	38.360	0.0066	18.024	15.594	38.216	0.710813	0.0007	0.7094
Badger Creek Tuff															
MPRM-30	0.512155	0.0005	-9.03	18.464	0.006	15.578	0.0065	38.338	0.0074	18.423	15.576	38.284	0.707571	0.0006	0.7073

Table 3 Hf isotopic data from zircon

Sample	spot	$^{176}Hf/^{177}Hf$	2σ	$^{176}Lu/^{177}Hf$	2σ	$^{176}Yb/^{177}Hf$	2σ	eHf(t)	2σ
MPRM-4	1a	0.282400	0.000026	0.000796	0.000037	0.026357	0.001354	-12.85	0.91
	2a	0.282399	0.000039	0.000817	0.000009	0.028056	0.000256	-12.89	1.36
	4b	0.282386	0.000048	0.001175	0.000018	0.052705	0.001300	-13.37	1.69
	5a	0.282445	0.000045	0.000940	0.000022	0.033747	0.001368	-11.29	1.58
	7a	0.282430	0.000033	0.001106	0.000017	0.047721	0.000662	-11.81	1.16
	9a	0.282364	0.000043	0.000803	0.000009	0.034710	0.000647	-14.14	1.53
	11a	0.282403	0.000034	0.000833	0.000007	0.037100	0.000518	-12.75	1.21
	12a	0.282398	0.000048	0.001284	0.000040	0.060408	0.001920	-12.93	1.70
MPRM-6	1a	0.282413	0.000039	0.000725	0.000001	0.034595	0.000174	-12.37	1.37
	2a	0.282497	0.000037	0.000855	0.000003	0.042002	0.000302	-9.43	1.30
	4a	0.282487	0.000049	0.001299	0.000072	0.061081	0.001081	-9.77	1.73
	7a	0.282451	0.000056	0.001083	0.000066	0.051652	0.002294	-11.06	1.96
	8a	0.282430	0.000032	0.000872	0.000008	0.042049	0.000516	-11.80	1.13
	10b	0.282370	0.000037	0.001314	0.000176	0.054154	0.004494	-13.92	1.30
	11a	0.282411	0.000042	0.000845	0.000011	0.039641	0.000247	-12.45	1.49
	13a	0.282421	0.000037	0.001021	0.000016	0.047384	0.000532	-12.10	1.30
MPRM-15	2a	0.282397	0.000052	0.000983	0.000045	0.043546	0.001730	-12.94	1.83
	5a	0.282278	0.000071	0.001449	0.000234	0.059228	0.006298	-17.14	2.50
	7a	0.282430	0.000070	0.000755	0.000028	0.035865	0.001225	-11.75	2.47
	11a	0.282381	0.000069	0.000650	0.000016	0.030523	0.000729	-13.49	2.44
	12a	0.282400	0.000051	0.000638	0.000005	0.029627	0.000372	-12.81	1.81
	13a	0.282448	0.000055	0.001371	0.000076	0.067361	0.002686	-11.14	1.93
	14a	0.282381	0.000048	0.000788	0.000005	0.035726	0.000073	-13.49	1.69
	16a	0.282425	0.000043	0.000687	0.000039	0.032007	0.001716	-11.93	1.53
	17a	0.282413	0.000052	0.000927	0.000027	0.044420	0.001290	-12.36	1.83
	18a	0.282384	0.000054	0.001742	0.000125	0.078476	0.003613	-13.42	1.89
MPRM-17	1a	0.282405	0.000066	0.000756	0.000007	0.032489	0.000407	-12.66	2.35
	2a	0.282417	0.000066	0.000711	0.000020	0.029122	0.000737	-12.25	2.34
	4a	0.282443	0.000058	0.000999	0.000010	0.036310	0.000395	-11.33	2.04
	4b	0.282464	0.000077	0.000767	0.000076	0.030224	0.002952	-10.57	2.74
	6a	0.282396	0.000056	0.000916	0.000034	0.038727	0.001233	-12.98	1.96
	7a	0.282388	0.000050	0.001205	0.000041	0.053602	0.002536	-13.27	1.76
	8a	0.282473	0.000057	0.001057	0.000022	0.038034	0.000431	-10.27	2.01
	10b	0.282424	0.000050	0.000825	0.000020	0.035025	0.001286	-11.99	1.77
	12a	0.282377	0.000077	0.000809	0.000007	0.034571	0.000416	-13.66	2.73
	13a	0.282417	0.000051	0.001243	0.000034	0.046025	0.001071	-12.24	1.81
	14a	0.282443	0.000050	0.000669	0.000006	0.028100	0.000217	-11.31	1.78
MPRM-20	1a	0.282458	0.000029	0.000882	0.000025	0.030513	0.001681	-10.80	1.02
	4a	0.282397	0.000023	0.000571	0.000009	0.019749	0.000590	-12.97	0.82
	5a	0.282379	0.000034	0.000773	0.000005	0.032636	0.000236	-13.62	1.19
	6a	0.282397	0.000025	0.000605	0.000006	0.021396	0.000248	-12.98	0.87
	7a	0.282429	0.000031	0.000614	0.000002	0.024888	0.000287	-11.83	1.10
	8a	0.282409	0.000032	0.000815	0.000012	0.032317	0.000919	-12.54	1.14
MPRM-21	14a	0.282410	0.000030	0.001173	0.000044	0.046245	0.002609	-12.50	1.05
	15b	0.282383	0.000034	0.001260	0.000144	0.049726	0.006069	-13.47	1.22
	16a	0.282372	0.000050	0.000487	0.000002	0.019320	0.000149	-13.84	1.77
	17a	0.282447	0.000033	0.000925	0.000023	0.036476	0.001047	-11.18	1.15
	18a	0.282391	0.000024	0.000999	0.000030	0.044626	0.001184	-13.17	0.85
	19a	0.282443	0.000029	0.000971	0.000027	0.046663	0.001378	-11.36	1.03
	20a	0.282420	0.000030	0.001192	0.000057	0.053517	0.002463	-12.17	1.05

Table 3 continued Hf isotopic data from zircon

Sample	spot	$^{176}Hf/^{177}Hf$	2σ	$^{176}Lu/^{177}Hf$	2σ	$^{176}Yb/^{177}Hf$	2σ	eHf(t)	2σ
MPRM-23	1a	0.282467	0.000036	0.000878	0.000019	0.035702	0.000806	-10.61	1.27
	2a	0.282428	0.000049	0.000680	0.000027	0.028102	0.001382	-11.96	1.75
	3a	0.282429	0.000054	0.000356	0.000002	0.015541	0.000055	-11.94	1.90
	4a	0.282477	0.000036	0.000864	0.000118	0.038374	0.004843	-10.23	1.27
	4b	0.282439	0.000048	0.000838	0.000045	0.033289	0.001800	-11.59	1.71
	5a	0.282444	0.000032	0.000652	0.000003	0.026920	0.000163	-11.40	1.14
	5b	0.282513	0.000041	0.002256	0.000315	0.097730	0.013787	-9.01	1.43
	6a	0.282510	0.000048	0.002031	0.000061	0.092539	0.003277	-9.12	1.69
	7a	0.282540	0.000049	0.001667	0.000126	0.071561	0.005735	-8.03	1.73
	8a	0.282475	0.000041	0.000684	0.000044	0.035065	0.002350	-10.32	1.44
	9a	0.282459	0.000050	0.000573	0.000011	0.028452	0.000581	-10.86	1.77
	10a	0.282465	0.000022	0.000343	0.000018	0.017027	0.000905	-10.66	0.77
	11a	0.282452	0.000041	0.000759	0.000013	0.034812	0.000730	-11.12	1.46
MPRM-30	1a	0.282477	0.000042	0.000535	0.000005	0.017506	0.000148	-10.15	2.18
	2a	0.282405	0.000064	0.000681	0.000006	0.025717	0.000214	-12.69	2.27
	3a	0.282419	0.000059	0.000757	0.000011	0.028195	0.000871	-12.19	2.17
	4a	0.282427	0.000061	0.000515	0.000004	0.019432	0.000223	-11.89	2.19
	4b	0.282408	0.000039	0.000773	0.000013	0.035523	0.000763	-12.60	2.17
	6a	0.282472	0.000055	0.000657	0.000004	0.024976	0.000119	-10.31	2.18
	7a	0.282457	0.000038	0.000984	0.000038	0.050843	0.001890	-10.86	2.16
	8a	0.282473	0.000045	0.000726	0.000008	0.034730	0.000656	-10.28	2.17
	10a	0.282437	0.000045	0.000710	0.000020	0.029457	0.001362	-11.58	2.17
	11a	0.282449	0.000024	0.000786	0.000012	0.036972	0.000332	-11.14	2.17
MPRM-33	1a	0.282408	0.000061	0.000367	0.000006	0.017150	0.000325	-12.54	2.17
	3a	0.282458	0.000041	0.000372	0.000006	0.017021	0.000218	-10.76	1.46
	4a	0.282400	0.000035	0.000398	0.000012	0.017736	0.000614	-12.84	1.25
	4b	0.282434	0.000041	0.000590	0.000027	0.027264	0.001461	-11.62	1.45
	6a	0.282451	0.000056	0.000504	0.000022	0.024394	0.000965	-11.03	1.97
	7a	0.282421	0.000062	0.000401	0.000008	0.019088	0.000403	-12.08	2.18
	8a	0.282399	0.000047	0.000390	0.000006	0.017833	0.000248	-12.86	1.68
	9a	0.282455	0.000035	0.000540	0.000012	0.024419	0.000467	-10.90	1.23
	9b	0.282468	0.000030	0.000740	0.000021	0.033274	0.000834	-10.42	1.07
	10a	0.282398	0.000038	0.000390	0.000011	0.017705	0.000382	-12.91	1.33
	12a	0.282427	0.000036	0.000333	0.000007	0.015100	0.000348	-11.89	1.27
	13a	0.282410	0.000032	0.000370	0.000009	0.016348	0.000345	-12.47	1.14
	14a	0.282442	0.000024	0.000491	0.000023	0.021765	0.000594	-11.35	0.86
MPRM-37	1a	0.282464	0.000023	0.000515	0.000006	0.024320	0.000459	-10.68	0.80
	2a	0.282456	0.000064	0.000500	0.000013	0.024423	0.000717	-10.97	2.27
	3a	0.282540	0.000047	0.000953	0.000096	0.046501	0.004063	-8.02	1.67
	4a	0.282478	0.000036	0.000811	0.000037	0.041139	0.001904	-10.22	1.29
	5a	0.282517	0.000029	0.001514	0.000045	0.067605	0.001747	-8.84	1.02
	6a	0.282526	0.000028	0.001332	0.000063	0.064814	0.003407	-8.51	0.98
	7a	0.282510	0.000038	0.001238	0.000089	0.053724	0.004366	-9.07	1.36
	8a	0.282502	0.000030	0.000878	0.000032	0.041291	0.001440	-9.35	1.07
	9a	0.282505	0.000035	0.000775	0.000065	0.034048	0.002673	-9.27	1.23
	10a	0.282453	0.000036	0.001107	0.000064	0.045757	0.002928	-11.11	1.28
MPRM-38	1a	0.282418	0.000056	0.000829	0.000072	0.035475	0.003114	-12.31	1.99
	2a	0.282396	0.000072	0.001082	0.000053	0.042892	0.002083	-13.09	2.54
	3a	0.282562	0.000060	0.000946	0.000037	0.038707	0.001939	-7.23	2.14
	4a	0.282452	0.000051	0.000871	0.000032	0.036237	0.001560	-11.11	1.81
	5a	0.282458	0.000048	0.001061	0.000023	0.044457	0.000767	-10.92	1.70
	6a	0.282500	0.000054	0.000601	0.000011	0.026958	0.000586	-9.40	1.92
	7a	0.282482	0.000033	0.000725	0.000022	0.031940	0.000757	-10.03	1.16
	7b	0.282510	0.000046	0.000793	0.000082	0.034408	0.003766	-9.05	1.62
	8a	0.282448	0.000041	0.001055	0.000032	0.047546	0.001873	-11.26	1.46
	10a	0.282442	0.000046	0.000703	0.000008	0.034920	0.000472	-11.44	1.61
	11a	0.282486	0.000046	0.001063	0.000096	0.052811	0.004136	-9.90	1.62

Table 4. U-Pb data for rocks of the Mount Princeton magma center

ID (n)	Pb* / Pbc	Th / U	$^{206}Pb/^{204}Pb$ [a]	$^{206}Pb/^{238}U$ [b]	error (%)	$^{207}Pb/^{235}U$ [b]	error (%)	$^{207}Pb/^{206}Pb$ [b]	error (%)	ages (Ma) [c] $^{206}Pb/^{238}U$	error (Ma)	ages (Ma) [c] $^{207}Pb/^{235}U$	ages (Ma) [c] $^{207}Pb/^{206}Pb$	corr. coeff.	total common Pb (pg)
Mount Princeton Quartz Monzonite (MPRM-33; 0387588, 4281885)															
F-7 (1)	11	1.08	622.78	0.00558	0.17	0.03604	0.60	0.04686	0.56	35.95	0.060	35.95	35.68	0.402	0.72
F-11 (2)	5.9	0.858	349.42	0.00555	0.13	0.03567	1.0	0.04663	0.95	35.77	0.048	35.59	23.50	0.451	2.9
F-13 (1)	7.7	1.28	407.10	0.00555	0.10	0.03588	0.58	0.04688	0.55	35.78	0.036	35.80	36.87	0.413	2.1
F-14 (2)	8.7	0.899	501.87	0.00555	0.10	0.03602	0.51	0.04706	0.48	35.79	0.036	35.93	45.47	0.397	2.4
F-15 (2)	18	0.783	1071.2	0.00555	0.11	0.03611	0.29	0.04716	0.26	35.80	0.038	36.02	50.51	0.430	2.2
Mount Princeton Quartz Monzonite (MPRM-6; 0377514, 4277352)															
F-1 (3)	28	0.911	1578.5	0.00552	0.21	0.03555	0.33	0.04673	0.25	35.55	0.075	35.47	29.82	0.672	2.3
F-2 (3)	32	0.720	1853.0	0.00553	0.24	0.03555	0.39	0.04666	0.30	35.61	0.086	35.47	25.97	0.647	3.9
F-6 (2)	9.9	0.842	572.15	0.00549	0.15	0.03566	0.77	0.04709	0.73	35.39	0.054	35.57	47.94	0.368	3.8
F-7 (2)	20	0.788	1164.9	0.00549	0.15	0.03539	0.49	0.04672	0.45	35.40	0.053	35.31	29.27	0.417	3.5
F-16 (1)	21	0.864	1174.3	0.00550	0.14	0.03540	0.37	0.04667	0.33	35.45	0.049	35.32	26.61	0.451	2.2
F-17 (1)	19	0.837	1068.0	0.00550	0.10	0.03557	0.26	0.04691	0.24	35.44	0.036	35.49	38.70	0.451	2.2
F-19 (1)	11	0.848	646.36	0.00550	0.12	0.03550	0.30	0.04681	0.27	35.45	0.044	35.42	33.57	0.456	1.6
Mount Princeton Quartz Monzonite (MPRM-17; 0387042, 4289957)															
F-2 (1)	17	0.805	986.39	0.00550	0.14	0.03535	0.60	0.04663	0.56	35.43	0.048	35.28	24.60	0.390	1.4
F-4 (2)	23	0.630	1369.8	0.00548	0.13	0.03513	0.60	0.04649	0.56	35.32	0.047	35.06	17.09	0.366	1.5
F-7 (1)	18	0.509	1141.0	0.00548	0.11	0.03522	0.43	0.04662	0.40	35.32	0.037	35.15	23.13	0.411	2.1
F-10 (1)	18	0.823	1020.2	0.00550	0.15	0.03547	0.35	0.04682	0.31	35.41	0.052	35.39	34.03	0.474	2.3
Mount Aetna Quartz Monzonite (MPRM-21; 383745; 4271437)															
F-11 (2)	46	0.615	2744.2	0.00542	0.14	0.03483	0.40	0.04661	0.36	34.93	0.050	34.76	22.86	0.455	1.8
F-12 (2)	34	0.700	1992.2	0.00542	0.13	0.03485	0.54	0.04659	0.50	34.97	0.045	34.79	21.85	0.430	1.9
F-15 (1)	67	0.674	3968.1	0.00541	0.10	0.03484	0.20	0.04669	0.17	34.89	0.036	34.77	26.52	0.546	1.0
F-18 (1)	32	0.717	1859.8	0.00542	0.15	0.03499	0.38	0.04678	0.34	34.97	0.053	34.92	31.46	0.456	1.1
F-19 (1)	16	0.727	926.82	0.00543	0.16	0.03496	1.1	0.04672	1.0	34.99	0.057	34.89	28.35	0.398	1.5
F-20 (2)	42	0.623	2490.4	0.00542	0.19	0.03487	0.43	0.04668	0.37	34.93	0.066	34.81	26.06	0.494	1.6
Mount Aetna Quartz Monzonite (MPRM-20; 383578, 4271646)															
F-2 (2)	21	0.619	1284.5	0.00538	0.12	0.03461	0.33	0.04667	0.30	34.66	0.041	34.54	26.43	0.442	2.5
F-3 (2)	84	0.447	5271.6	0.00537	0.30	0.03462	0.32	0.04672	0.12	34.64	0.10	34.55	28.44	0.924	1.7
F-7 (1)	25	0.487	1566.3	0.00535	0.12	0.03443	0.37	0.04668	0.34	34.48	0.042	34.37	26.61	0.398	1.0
F-8 (1)	8.6	0.443	556.92	0.00537	0.11	0.03466	0.41	0.04682	0.39	34.61	0.039	34.60	33.39	0.340	2.4
tuff dike (MPRM-4; 0380061, 4292398)															
F-10 (2)	20	0.807	1146.2	0.00536	0.16	0.03474	0.65	0.04701	0.60	34.55	0.056	34.68	43.64	0.409	1.4
F-11 (2)	39	0.597	2373.1	0.00537	0.12	0.03464	0.24	0.04675	0.20	34.64	0.041	34.57	30.27	0.540	2.6
F-12 (2)	54	0.644	3175.0	0.00536	0.11	0.03450	0.25	0.04671	0.22	34.53	0.038	34.44	28.26	0.484	1.2
F-15 (2)	24	0.674	1427.4	0.00536	0.10	0.03471	0.27	0.04696	0.24	34.56	0.036	34.65	40.80	0.445	1.5
ring dike (MPRM-39; 0382900 4285240)															
F-3 (3)	17	0.707	1012.2	0.00535	0.14	0.03457	0.32	0.04686	0.28	34.49	0.047	34.51	36.13	0.480	1.5
F-7 (2)	16	0.710	921.09	0.00536	0.26	0.03451	0.60	0.04669	0.53	34.56	0.089	34.45	27.25	0.374	1.3
F-8 (2)	29	0.625	1757.8	0.00535	0.12	0.03452	0.40	0.04682	0.37	34.46	0.043	34.46	34.12	0.390	0.70
F-9 (3)	23	0.721	1350.3	0.00536	0.11	0.03469	0.30	0.04694	0.27	34.54	0.037	34.63	40.44	0.439	0.88
F-10 (2)	12	0.960	679.63	0.00533	0.12	0.03455	0.87	0.04697	0.82	34.37	0.042	34.48	42.27	0.443	1.1
Badger Creek Tuff (MPRM-30; 0416691, 4274214)															
F-7 (2)	42	0.572	2514.1	0.00535	0.16	0.03446	0.29	0.04672	0.24	34.48	0.056	34.40	28.63	0.590	1.4
F-11 (2)	55	0.562	3334.4	0.00534	0.10	0.03456	0.24	0.04692	0.21	34.44	0.035	34.50	38.79	0.466	0.48
F-14 (1)	16	0.799	939.30	0.00535	0.12	0.03455	0.56	0.04681	0.52	34.50	0.040	34.49	33.66	0.386	0.59
F-15 (2)	29	0.922	1630.0	0.00534	0.10	0.03450	0.30	0.04686	0.27	34.42	0.036	34.44	36.32	0.421	1.2
F-18 (1)	19	0.588	1156.5	0.00535	0.13	0.03442	0.85	0.04662	0.80	34.51	0.046	34.36	23.59	0.436	1.0
Mount Antero Leucogranite (MPRM-23; 391036; 4277871)															
F-1 (2)	18	0.709	1061.4	0.00470	0.10	0.03040	0.35	0.04695	0.32	30.28	0.031	30.41	40.99	0.379	1.1
F-2 (1)	16	0.581	996.28	0.00468	0.11	0.03028	0.32	0.04688	0.30	30.20	0.032	30.29	37.05	0.393	1.2
F-3 (2)	17	0.713	1031.6	0.00470	0.10	0.03033	0.44	0.04684	0.41	30.27	0.031	30.34	35.58	0.390	1.0

[a] Measured ratio corrected for fractionation only. All Pb isotope ratios were measured using the Daly detector, and are corrected for mass fractionation using 0.15 %/amu.
[b] Corrected for fractionation, spike, and blank.
[c] Th/U assumed for the magma using whole-rock data. All ages are corrected for Th disequilibrium.
[d] All errors except error in the $^{206}Pb/^{238}U$ age are reported in percent at the 2σ confidence interval. Error in the $^{206}Pb/^{238}U$ age is reported in absolute (Ma) at the 2σ confidence interval.

CHAPTER 3

EXPERIMENTAL EVIDENCE FOR CRYSTAL COARSENING AND FABRIC DEVELOPMENT DURING TEMPERATURE CYCLING[1]

ABSTRACT

Oscillating temperature dramatically speeds up recrystallization of a magma analog consisting of ammonium thiocyanate and ammonium chloride crystals in liquid. Linear growth rates increase by a factor of 10 if temperature is oscillated up and down a few degrees (e.g., 47 ± 3 °C) relative to nominally static conditions. Crystals pulse in size during thermal cycling; over the course of hundreds of cycles larger crystals grow and smaller crystals shrink, dramatically skewing the crystal size distribution. Crystal dissolution and growth in a pulsing thermal gradient produces a pronounced fabric, with crystals of ammonium thiocyanate aligned subparallel to the direction of heat flow. Alignment occurs via selective dissolution and growth of crystals of diverse orientations inherited from the starting material. These results have important implications for understanding how crystals grow and for interpreting texture in igneous rocks. Temperature cycling is likely common in magmatic systems and needs to be considered when analyzing chemical zoning of igneous crystals and rock textures.

INTRODUCTION

Igneous textures provide important information about the histories of magmatic

---

[1]paper published in *Geology*, December 2011; v. 39; no. 12; p. 1139-1142

bodies (e.g. Iddings 1909; Cashman 1990; Jerram and Higgins 2007; Hersum and Marsh 2007). In volcanic rocks, crystallization sequence and crystal development can be studied by collection of magma and its cooled counterparts (e.g. Peck et al. 1966) and by quenching experiments (e.g. Hall 1805; Lofgren 1980). How plutonic rocks attain their textures is a more difficult problem because such textures integrate processes that occur during full crystallization from near-liquidus to subsolidus temperatures (e.g. Shelley 1993). However, the processes that create the textures of volcanic rocks can be complicated as well (Blundy and Cashman 2008; Higgins 2011).

Recent experimental and chemical studies demonstrate that there is reason to question some common interpretations of igneous textures. For example, observations of crystal growth in a low-temperature magma analog demonstrate that the usual rules for interpreting sequence of crystallization are commonly violated (Means and Park 1994); some layering in plutonic complexes likely results from chemical rather than physical processes (Boudreau and McBirney 1997); and late crystallization of K-feldspar in dacitic magmas contradicts the common assumption (e.g. Vernon 1986) that K-feldspar megacrysts must represent early crystallization in granodiorites (Johnson and Glazner, 2010).

Simakin and Bindeman (2008) suggested that temperature cycling can produce observed concave-downward crystal size distributions (CSDs) by repeated dissolution and crystallization events. Experiments on ice growth in ice cream (Donhowe and Hartel 1996) show that temperature cycling has a profound effect on CSDs. In particular, these experiments show that large crystals may grow late in the solidification history of a material via dissolution-crystallization. These studies encourage exploration of new chemical and mechanical processes that could be responsible for producing igneous textures.

In this contribution we present the effects of temperature cycling and thermal gradients on crystals in a magma analog system that consists of three solid phases and a liquid phase (Fig. 1) at room temperature. In situ observation provides a view of cryptic processes that are not directly observable in igneous systems.

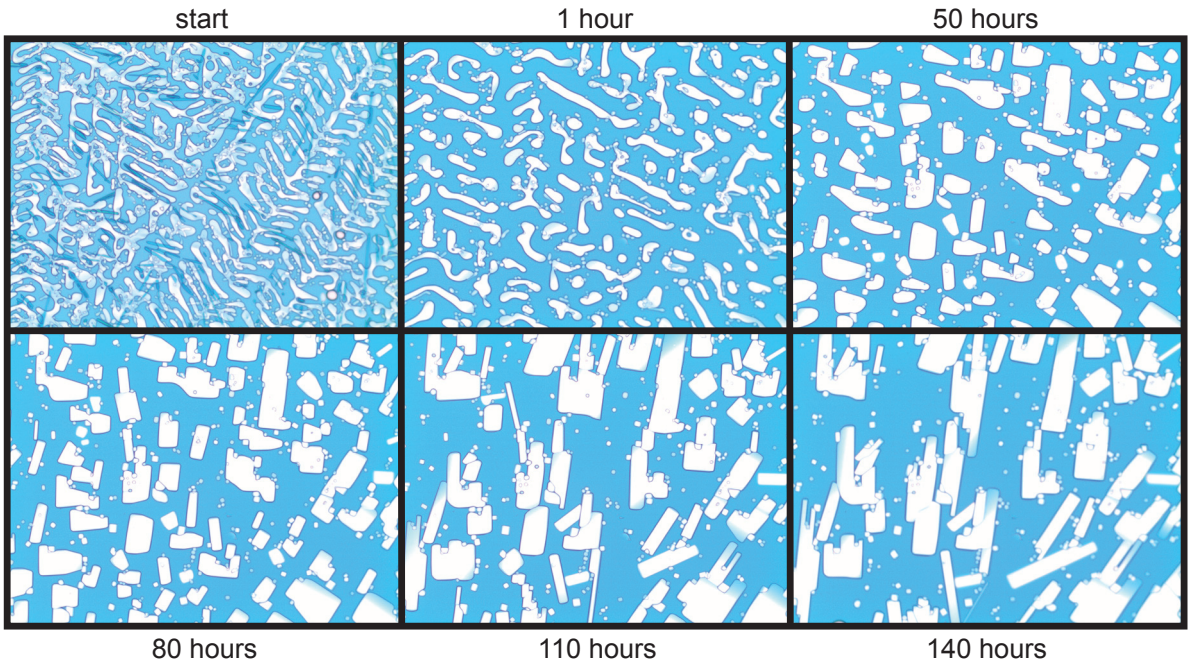

Figure 1 Six still photos from an experiment observed through plane polarized light at 10x (each pane is ~1 mm wide). Temperature of experiment is 47 ± 0.3ºC when static and 47 ± 3ºC when oscillating (period of 12 min.). Pane 1 shows the system shortly after remelting. The white phase (slightly bluish here because the crystals do not span the full vertical thickness) is dendritic, the cubic phase forms tiny, euhedral, white crystals, and the blue phase is acicular. Pane 2, from 1 h into the experiment, shows that shortly after placement on the stage at 47ºC the blue phase dissolves and the white phase condenses into more equant crystals, as noted by Means and Park (1994). Pane 3 is ~2 days into the static temperature run and the system is stable at this point, with minimal crystal growth or dissolution. The bottom three pictures were taken after the temperature was cycled. Pane 4 is ~6 h after temperature cycling was started and shows significant crystal growth relative to the previous photo. Pane 5 shows continued coarsening of the white phase and obvious N-S preferred orientation. The final frame shows continued coarsening and strong preferred orientation. The sixth and final frame is shown to illustrate the joining of large crystals into one clump of crystals; this phenomenon is seen in the largest crystal on Figure 3 at ~120 h.

METHODS

Our experiments were based on a procedure modified from Means and Park (1994). A drop (~10 mL) of the starting solution (a 5:1 by weight mixture of saturated ammonium thiocyanate and cobalt chloride hexahydrate) was placed on a 2.5x7.5 cm glass slide, partially dehydrated in an oven at 90 °C for 10 min and then melted on a hot plate at ~150 °C for 5 seconds. A 2x2 cm glass slide was then placed on top of the liquid and pressed so that the liquid was ~30 μm thick. At this point, the charge rapidly crystallizes to a highly dendritic mass of three solid phases in blue liquid (Fig. 1). The solid phases are ammonium thiocyanate (*white phase*, NH_4SCN, bladed to blocky texture), ammonium chloride (*cubic phase*, NH_4Cl, cubic habit and isotropic), and diammonia tetrathiocyanato cobaltate (*blue phase*, $[NH_4]_2Co[SCN]_4 \cdot nH_2O$, blue color, acicular). We then sealed the edges with low-viscosity UV-curing epoxy. Charges were melted again at ~120 °C immediately before being placed on the microscope stage.

The slide was held at the desired temperatures by a heating stage (Warner Instruments CSH-1) controlled via LabView (Fig. 2). A slot in the heating stage cradled the slide between two conductor plates and a 3 mm thick aluminum plate was placed on top of the slide to promote even heat distribution. The aluminum plate had a 1 cm diameter observation hole in its center and a thin groove drilled down its length. A needle thermocouple placed in the groove measured the temperature on top of the slide at the edge of the field of observation. A consequence of the side-heating aspect of this design is that temperature oscillations in the heaters produce two thermal gradients perpendicular to the long axis of the slide. As T goes up in the heaters isotherms advance into the slide and as T declines the isotherms retreat.

We have compared the textural evolution of ammonium thiocyanate crystals during both thermal oscillation and constant temperature (static annealing) states by experimenting with temperatures ranging from 40 to 60 ºC, with or without a sinusoidal temperature oscillation. Set amplitudes of oscillations ranged from ±3 to ±5 ºC with periods of 10 to 12 minutes. The measured temperature near the center of the slide was ~3 ºC cooler than the set

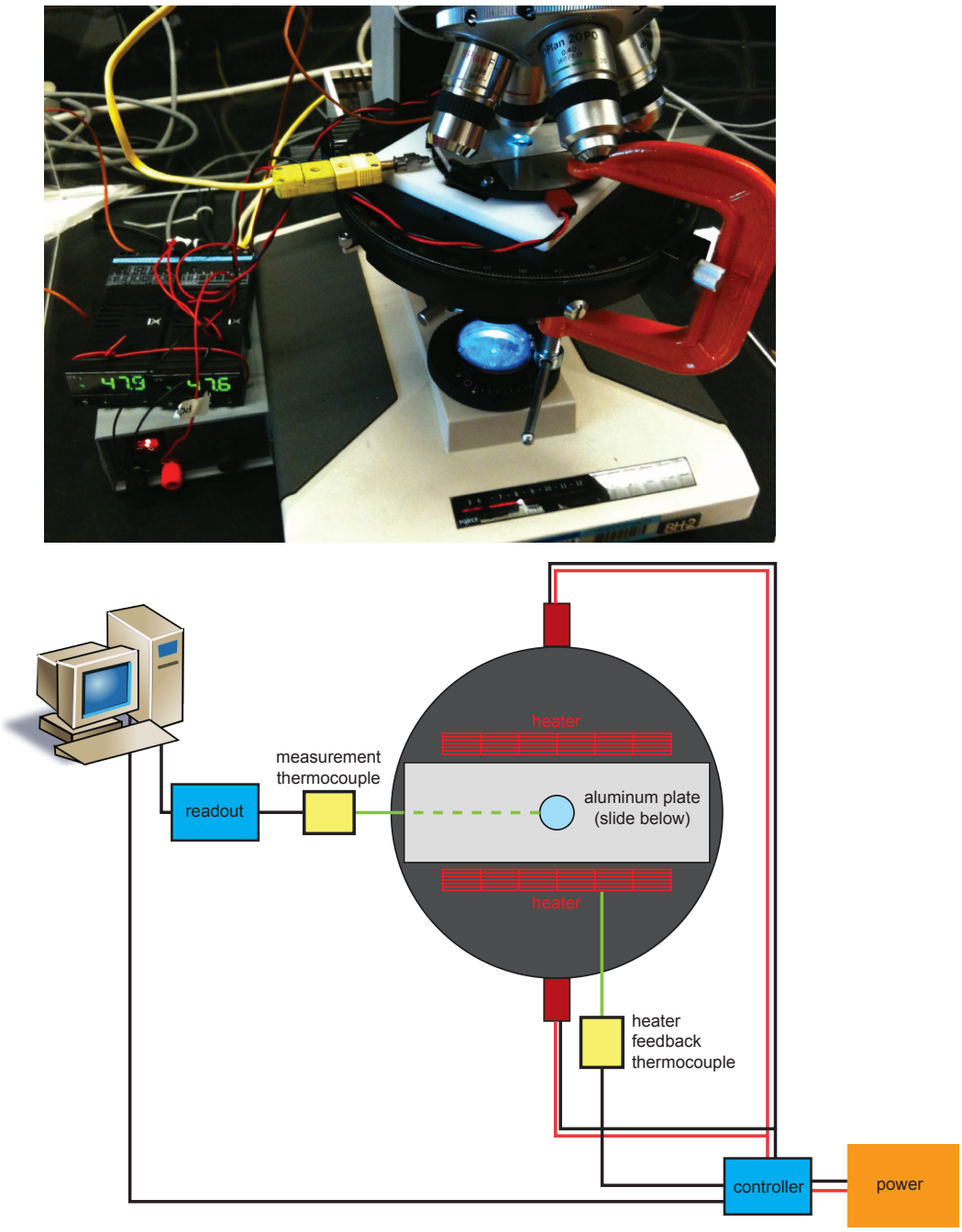

Figure 2 Picture of experimental setup and schematic diagram of experimental setup. A microscope heating stage is placed on a Teflon insulating block clamped to the stage of a petrographic microscope with a digital camera. The digital camera is attached to a desktop computer which allows real-time viewing and image capture. Twisted red-black wires feed heaters on either side of the slide. Two controllers are used, one monitors and controls temperature within the heating stage and the other monitors the temperature on top of the glass slide, under the aluminum cover and near the optical path, with a hypodermic probe (yellow connectors). All temperature measurements are sent to a desktop computer and plotted and stored using a LabView program.

temperature and the measured amplitude of oscillation was ~2 ºC smaller than the set amplitude because of heat loss. Measured temperatures during static annealing typically varied < ± 0.3 °C. We acquired images every 10 min in both plane polarized and circularly cross-polarized light (Higgins 2010). Circular cross-polarization isolated ammonium thiocyanate crystals because ammonium chloride crystals are isotropic and the temperature was above the liquidus of diammonia tetrathiocyanato cobaltate in most experiments.

To measure crystal sizes, we wrote and utilized a Matlab program in which crystals were randomly selected, measured and automatically tracked through a series of images. Crystal dimensions typically observed were 40x40 μm early in an experiment and 250x50 μm late in an experiment. Given the restricted thickness of 30 μm, this indicates that crystals were generally platy or bladed, although this habit is created by the experimental setup.

RESULTS

We present data from 2 experiments that best exemplify the common results we obtained from ~30 experiments. During static annealing the initial dendritic crystals rapidly condense down to much more equant crystals (Figs. 3, 4), as noted by Means and Park (1994). At ~50 °C this happens within 10–30 min and condensation to blob-like equant crystals is complete within 4 h. Further textural maturation after the initial condensation from dendritic morphology is slow (Fig. 3). No new nucleation occurs during the experiments and the total crystal area in the field of view is roughly constant, with a slight increase over time related to the lack of insulation at the observation hole.

If the temperature at the slide is cycled ± 2–3 °C, the texture rapidly matures as crystals coarsen (Fig. 4). All crystals cycle up and down in size, small crystals disappear and large crystals grow (Fig. 3, Fig. 5). Total crystal area at a temperature corresponding to the midpoint of the cycle remains nearly constant throughout the experiments, but the linear rate of crystal growth increases by a factor of approximately 10 when temperature is cycled in this manner (Fig. 3). Given a constant thickness, this implies that the volumetric growth

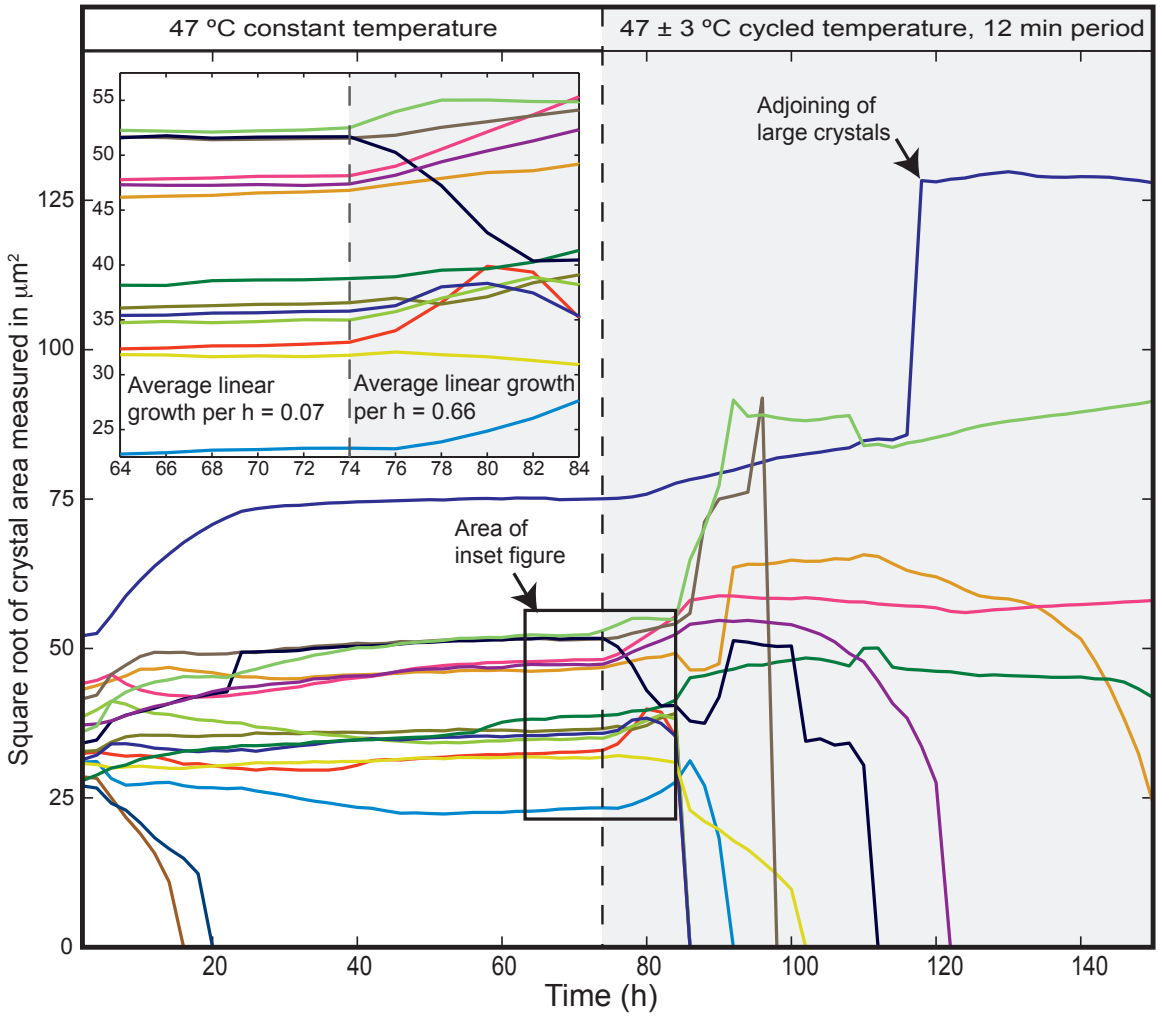

Figure 3 Plot of evolution of specific crystal sizes (characteristic length, defined as area$^{1/2}$) through time for the experiment shown in Figure 1. Different colored lines represent different crystals. Time zero relates to pane 2 in Figure 1. By 20 h some crystals have dissolved, some have stayed relatively constant in size, and some have grown, but from ~20 h to just before temperature cycling began very little change occurred—initially ornate high-energy crystals had annealed to less intricate, lower-energy shapes. After oscillation began there was great mobility in crystal boundaries, many crystals grew to large size, and many disappeared. Inset in top left highlights the changes seen 10 h before and after temperature oscillation began. Colors in the inset relate directly to the main figure. Average linear growth rates for crystals with positive growth were calculated for the time sequence from 64 to 74 h for constant T and from 74 to 84 h for oscillating T. The increase in growth rates from static to oscillating conditions is approximately tenfold. Farther into cycling conditions interpretation is more difficult because crystals begin to coalesce, as seen by the largest crystal in this calculation at ~120 h. However, crystals continued to dissolve until the end of the experiment as seen by the several lines that show gradual to sharp declines to 0. Large crystals can disappear in less than an hour during the oscillating temperature phase if they are oriented at a high angle to the thermal gradient.

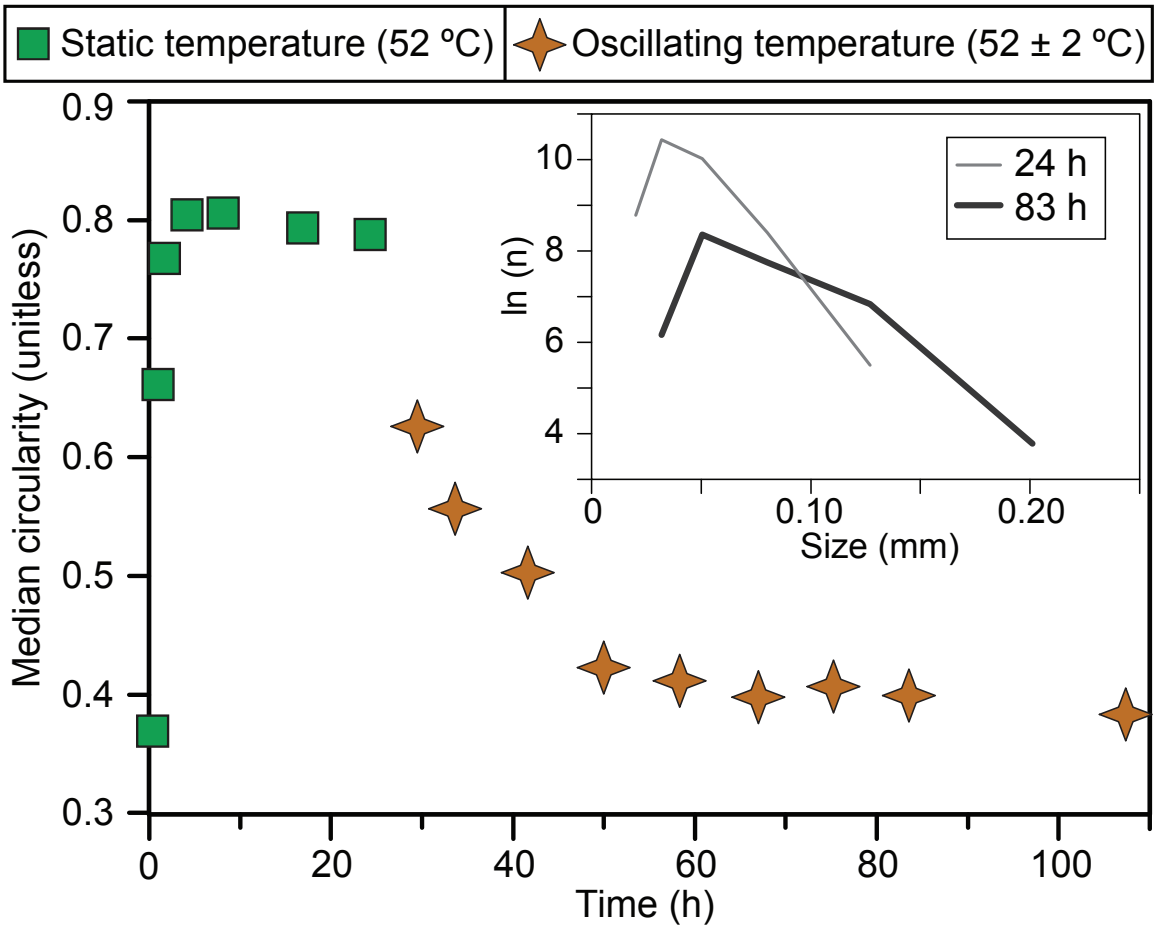

Figure 4 Median circularity versus time for an experiment run at 52ºC static then changed to an oscillating temperature cycle with amplitude of 2 °C and a period of 10 min. Circularity C is defined as $4\pi A/P^2$, where A is crystal area and P is crystal perimeter; for reference, a circle has a C = 1, a square C = 0.785, and a rectangle with an aspect ratio of 4:1 C = 0.503. C rapidly increased and then plateaued early in the experiment as initially dendritic crystals became more equant, but dropped dramatically when cycling began owing to crystal elongation. Circularity was measured from images using ImageJ (http://rsbweb.nih.gov/ij/) after cutting apart touching crystal images; tiniest crystals (<100 square pixels) were omitted in median calculation owing to problems with measuring circularity of small objects with ImageJ. Inset figure shows CSDs for 2 of the frames analyzed for circularity (see Figure 5 for additional CSDs and description of CSDs).

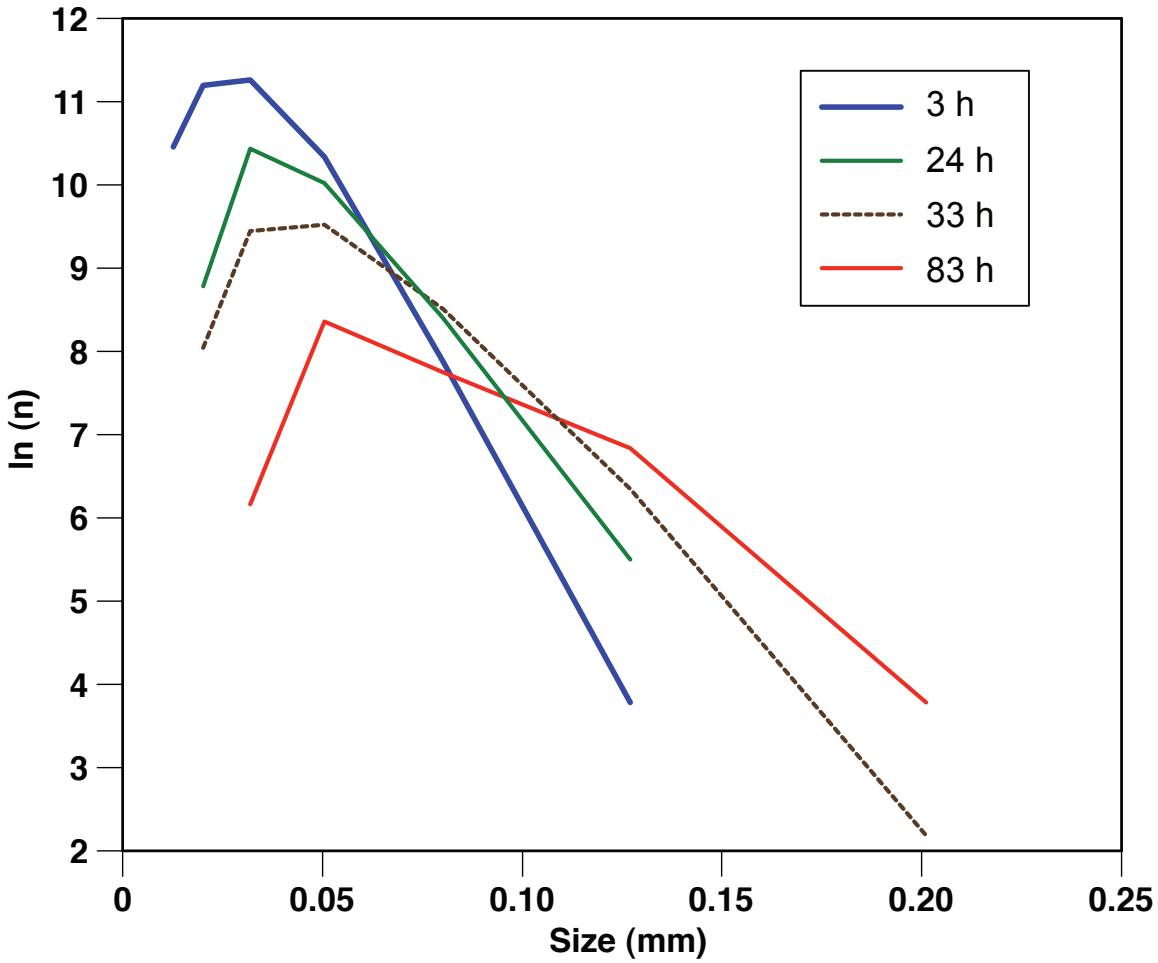

Figure 5 CSD plot for four different still frames from the experiment discussed in Figure 3. Touching crystals in the images were dissected using a thin black line in order to analyze each individual crystal. After cutting apart touching crystal images the entire images were then analyzed using the CSD Corrections software (Higgins, 2000). We calculated CSDs using a shape of 5:1:1. The number of crystals analyzed in each frame is: 580 (3 hrs), 444 (24 hrs), 302 (33 hrs) and 163 (83 hrs). Later images show significant dissolution of small crystals and continual growth of larger crystals. All four distributions have a hump toward the low crystal size, which probably relates to the lack of new nucleation in our experiments after the condensation into blobs from the dendritic mass.

rate increases by a factor of approximately 100. Crystals become significantly more elongate (Fig. 4) and locally accrete to one another and resolve minor crystallographic misalignments, resulting in formation of a single, much larger crystal. Schiavi et al. (2009) noted this phenomenon in plagioclase observed during their crystallization experiments.

The ammonium thiocyanate crystals take on a subhedral, square to elongate shape and a strongly preferred orientation with long axes parallel to the direction of heat flow (north-south in images). The majority of this preferred orientation results from preferential growth of crystals oriented parallel to heat flow, and slower growth or dissolution of crystals in an oblique orientation. Crystal rotation is minor and uncommon. Crystals that start with their long axes approximately east-west commonly dissolve completely, but sometimes such crystals shrink in the east-west direction and grow in the north-south direction (Fig. 1).

DISCUSSION

Temperature Oscillation in Natural Systems

The compounds in this experimental system differ greatly in composition from natural magmas, but initial results from temperature cycling of basalt (Mills and Glazner 2011) indicate that the effects observed here also occur in silicate magmas. Thus, many observable features in igneous rocks, such as the presence of phenocrysts and overall texture and fabric, may result from crystal coarsening in a varying temperature field rather than from primary down-temperature crystallization processes.

Although experimental petrologists generally try to maintain constant temperatures in order to investigate equilibrium conditions, thermochronologic data indicate that temperature cycling occurs in nature (Davis et al. 2012). Simakin and Bindeman (2008) have argued that temperature oscillation is a ubiquitous process in igneous systems. Oscillatory chemical zoning in many minerals (e.g. Boone 1959) can be explained by a number of processes, but a simple way to produce complex oscillatory zoning in numerous minerals simultaneously (e.g., plagioclase, K-feldspar, zircon, apatite, and titanite) is to vary an intensive parameter

such as temperature.

Crystal Growth

We observed no new nucleation after initial dendritic growth during quenching (Fig. 1), indicating that textural modification occurs without additional nucleation. These results support data from Johnson and Glazner (2010) which show that the CSD of K-feldspar shifted dramatically across the transition from non-megacrystic granodiorite to megacrystic granodiorite in the Tuolumne Intrusive Suite of eastern California. The modal proportion of K-feldspar is roughly constant across this transition, but as one traverses into the megacrystic rock, small crystals of K-feldspar disappear and nearly all of the K-feldspar is concentrated into the megacrysts. As noted by Higgins (1999), this observation suggests a crystal coarsening process in which mass was transferred from small crystals to large ones.

Crystal coarsening in an oscillating temperature field has been studied extensively in food science. Investigations into the mechanisms of ice coarsening in ice cream clearly demonstrate that temperature fluctuations promote recrystallization. Donhowe and Hartel (1996) recognized several mechanisms by which ice texture changes. In particular, accretion of crystals and melt-refreeze recrystallization (i.e., dissolution-crystallization) were found to be the dominant processes that cause ice to coarsen. Dissolution-crystallization differs from Ostwald ripening in that the former involves differences in surface energy between crystals but occurs when an intensive variable (particularly temperature) fluctuates, whereas the latter occurs at constant temperature and pressure due solely to differences in surface energy between crystals.

We cannot isolate the contribution of Ostwald ripening to coarsening because we cannot completely eliminate high-frequency temperature fluctuations in our experiments,. However, the dramatic increase in coarsening rates that accompanies deliberate thermal cycling indicates that dissolution-crystallization is the dominant coarsening process. Additionally, CSDs of crystals from our experiments are skewed to the left (Fig. 4, Fig. 5) and thus inconsistent with CSD models of Ostwald ripening (Simakin and Bindeman 2008).

During static conditions, small high-frequency temperature oscillations (RMS variation 0.12 °C, maximum ~0.5ºC) occurring over periods of several seconds may lead to small dissolution and crystallization events that combine with Ostwald ripening to produce a specific texture, characterized by crystals with aspect ratios close to 1:1 (Fig. 1, Fig. 4). During larger, longer-period oscillations (>2ºC), larger dissolution and crystallization events overwhelm Ostwald ripening and produce a texture with much larger crystals and greater aspect ratios (Fig. 1, Fig. 4).

Magmatic Fabric

Magmatic fabric in plutonic rocks (i.e. fabric formed by igneous minerals that do not show solid-state deformation) is nearly always ascribed to magmatic flow and foliations and lineations defining a magmatic fabric are commonly used to infer magma flow paths (e.g. Pitcher and Berger 1972). However, several experimental investigations in addition to ours (Walker et al. 1988; DeFrates et al. 2006; Huang et al. 2009) have shown preferred crystallographic orientation of crystals grown in a thermal gradient. If some plutonic fabric elements form via crystal growth in a varying temperature field, then interpretations of magmatic fabric must be reexamined. For example, Bateman et al. (1983) found a confusing pattern of crossing weak magmatic foliations in the Cathedral Peak Granodiorite in California. The main fabric is a steeply oriented lineation defined by hornblende and some of the foliations strike directly into wall rock contacts, making a simple magma flow interpretation problematic. In this situation, magma flow cannot account for all of the magmatic fabric and hornblende alignment via crystallization in a vertical thermal gradient seems plausible. Other mineral alignments and magnetic fabrics that cut across external contacts (e.g. Pitcher and Berger 1972, p. 103, 188; Morgan 1998) could also form, or be enhanced, via thermal gradients.

CONCLUSIONS

Temperature experiments in the ammonium compound magma analog system show

that: 1) the rate of textural coarsening dramatically increases with thermal cycling, 2) the primary process of coarsening is dissolution-crystallization, 3) elongate crystals form a fabric parallel to the thermal gradient, 4) crystals oriented parallel to the thermal gradient coarsen at a faster rate than crystals oriented oblique to the gradient and 5) thermal cycling accentuates the magmatic fabric.

CHAPTER 4

EXPERIMENTAL STUDY OF TEMPERATURE CYCLING ON COARSENING OF PLAGIOCLASE AND OLIVINE IN AN ALKALI BASALT

ABSTRACT

Melting and crystallization experiments were performed on an alkali basalt at 1-atmosphere in order to investigate the effect of temperature cycling on crystal growth. Experiments at 1150ºC near Ni-NiO buffer indicate that coarsening of plagioclase and olivine crystals is accentuated by temperature cycling. We investigated the role of amplitude and period on coarsening and found that crystal number density negatively correlates with amplitude and average crystal size increases with increasing amplitude. We observed no correlation between cycle period and crystal number density or average crystal size. We suggest that dissolution and size-proportional crystal growth during repeated heating and cooling decreases crystal number density and increases average crystal size. Results indicate that phenocrysts can develop quickly in mafic magmas if the magma temperature is cycled.

INTRODUCTION

The texture of an igneous rock is a record of the crystallization history of its source magma. The various crystallizing minerals have different nucleation and growth rates that record changes in temperature and other intensive variables through time. The interplay of these rates, integrated over time, is a primary control on the resultant texture. Thus, in order to use texture to extract information about the history of a magma certain variables must be

independently known or estimated.

The interplay of nucleation and growth rates has been studied extensively in materials science by analyzing the crystal size distribution (CSD) of a population of crystals of a given phase (e.g., Randolph and Larson 1971). Cashman and Marsh (1988) applied this method to silicate melts by analyzing CSDs of basalt samples from Makaopuhi lava lake in Hawaii, where cooling rates and temperatures were directly measured. Their nucleation and growth rates were consistent with experimentally derived values (Kirkpatrick 1977), which led to the now-commonplace usage of CSDs in studies of magma dynamics (e.g. Higgins 1999; Schiavi et al. 2009).

Recent studies have used CSDs as a geochronometer (e.g. Mangan 1990; Higgins and Chandrasekharam 2007; Salisbury et al. 2008), which requires assuming a constant crystal growth rate. However, Brugger and Hammer (2010) showed that decompression rate affects growth rate of plagioclase crystals in dacite magmas, and Pupier et al. (2008) showed that cooling rate and plagioclase growth rate are correlated in basaltic melts, demonstrating that a constant growth rate is unlikely during magma genesis and residence.

In addition to the effect of variable decompression and cooling rates on CSDs, the process of textural coarsening skews CSDs of crystals in igneous rocks (Waters and Boudreau 1996; Higgins 1998; 1999; 2011a, b; Bindeman 2003). Phenocrystic texture is typically attributed to slow cooling followed by rapid cooling (e.g. Best 1982). However, several experiments demonstrate that phenocrystic textures can result from cooling at a constant rate (Lofgren et al. 1974; Walker et al. 1976). Coarsening can also occur during aging under isothermal conditions due to the inverse relationship between crystal size and surface energy (i.e. Ostwald ripening; Voorhees 1985).

Although coarsening can occur during constant-rate cooling and under isothermal conditions, temperature cycling greatly enhances coarsening. For decades, temperature oscillations have been used to grow large crystals in order to study physical parameters of single crystals (e.g. Hintzmann and Müller-Vogt 1969), and coarsening of ice during temperature

cycling is well documented (Colbeck 1982; Donhowe and Hartel 1996). This phenomenon likely also affects growth of silicate minerals in the Earth because temperature cycling in magmas is probably common. For example, repeated injection of hot magma (Huppert and Sparks 1988) and convection (Martin et al. 1987) can cause the temperature of a magma parcel to oscillate. Repeated injection of hydrous, felsic magmas may produce similar fluctuations in the activity of water owing to release of water during successive crystallization events (Glazner et al. 2011).

Simakin and Bindeman (2008) mathematically showed that repeated dissolution and crystallization events should cause a magma's CSD to evolve toward downward concavity. Their results were consistent with CSDs of zircon and quartz from geologic samples. Mills et al. (2011) demonstrated that coarsening during temperature cycling of a magma analog greatly increases average crystal size, changes crystal morphology, and generates crystal alignment under temperature gradients.

In this paper we present results from melting and crystallization experiments on an alkali basalt at 1-atm under both static and oscillating temperatures. The specific aim of these experiments is to understand the individual effects of cycle amplitude, cycle period and experiment duration on crystal coarsening (Fig. 1).

Notation

α cycle amplitude
τ cycle period
t experiment duration
T temperature

EXPERIMENTAL METHODS

Starting materials

Starting material was finely ground powder of an alkali basalt from Pisgah Crater, California. The alkali basalt (sample P-36 of Hughes 1986) contains 8% olivine and 13%

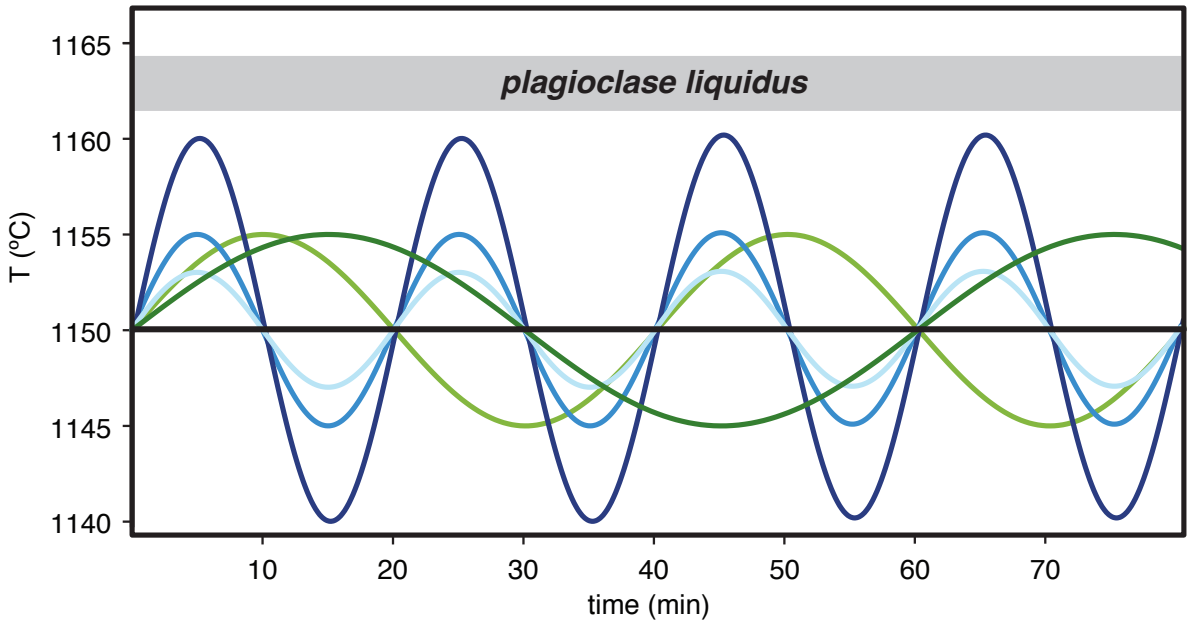

Figure 1 Plot of a subset of the experimental temperature profiles investigated in this study. In order to test the effects of α, τ was set to 20 min and α was varied from ±3ºC to ±10ºC. In order to test the effects of τ, α was set at ± 5ºC and τ was varied from 10 to 60 min. Experiments with t = 70 h and 120 h were conducted for all α/τ combinations. In addition, one static temperature (high-frequency, irregular oscillation of ±1ºC) experiment was conducted at 70 h and 120 h. The plagioclase liquidus was determined by the lack of plagioclase at 1165ºC and the presence of plagioclase at 1160ºC.

plagioclase phenocrysts in an interstitial groundmass of opaque minerals, brown glass, Ti-rich augite, and olivine with minor iddingsite alteration (Hughes 1986). The powder was produced by 10 min of crushing of cm-sized rock chips in a tungsten carbide ball mill. Particle size distribution of powdered starting material (Fig. 2; Glazner and Mills in review) indicates that the largest particles have radius approximately equal to 5 μm and the median and mean radii of the analyzed particle distribution are approximately 1 μm.

Experimental procedure

Platinum loops were fabricated from 0.13 mm diameter wire. The loops were approximately 4 mm in diameter with a crossing wire for additional support. A slurry composed of powdered starting material, a trace amount of white glue binder, and distilled water was pressed into a Teflon block mold with a hemispherical depression 5 mm in diameter. The wire loop was then pressed into the slurry and the entire block was placed on a hotplate until the water evaporated, approximately 5 min.

Melting and crystallization experiments were performed in the hotspot of a Deltech vertical tube, 1-atm, gas-mixing furnace. An atmosphere of approximately 90% CO_2 and 10% H_2, corresponding to an oxygen fugacity close to the Ni-NiO buffer, was maintained throughout all experiments. Temperature of the charge was monitored with a $Pt/PtRh_{10}$ (S-type) thermocouple calibrated against the melting temperature of Au (T= 1064ºC). Thermocouple temperature correction factors ranged from 4 to 10 ºC. The thermocouple was stationed within 1 cm of the hanging charge. At the termination of each experiment, the charges were quenched by running current through the 0.13 mm suspension wire, causing the sample to fall into a beaker of water.

We utilized a LabView program to control furnace temperature cycling and to record the measured temperature every 3 sec. The observed α from the monitor thermocouple was the same as the set α for $\tau > 10$ min. Observed α was 1°C less than the set α for experiments run with $\tau = 5$ min owing to thermal inertia in the system. Cycled experiments were set to the mean temperature for 20 min prior to quench.

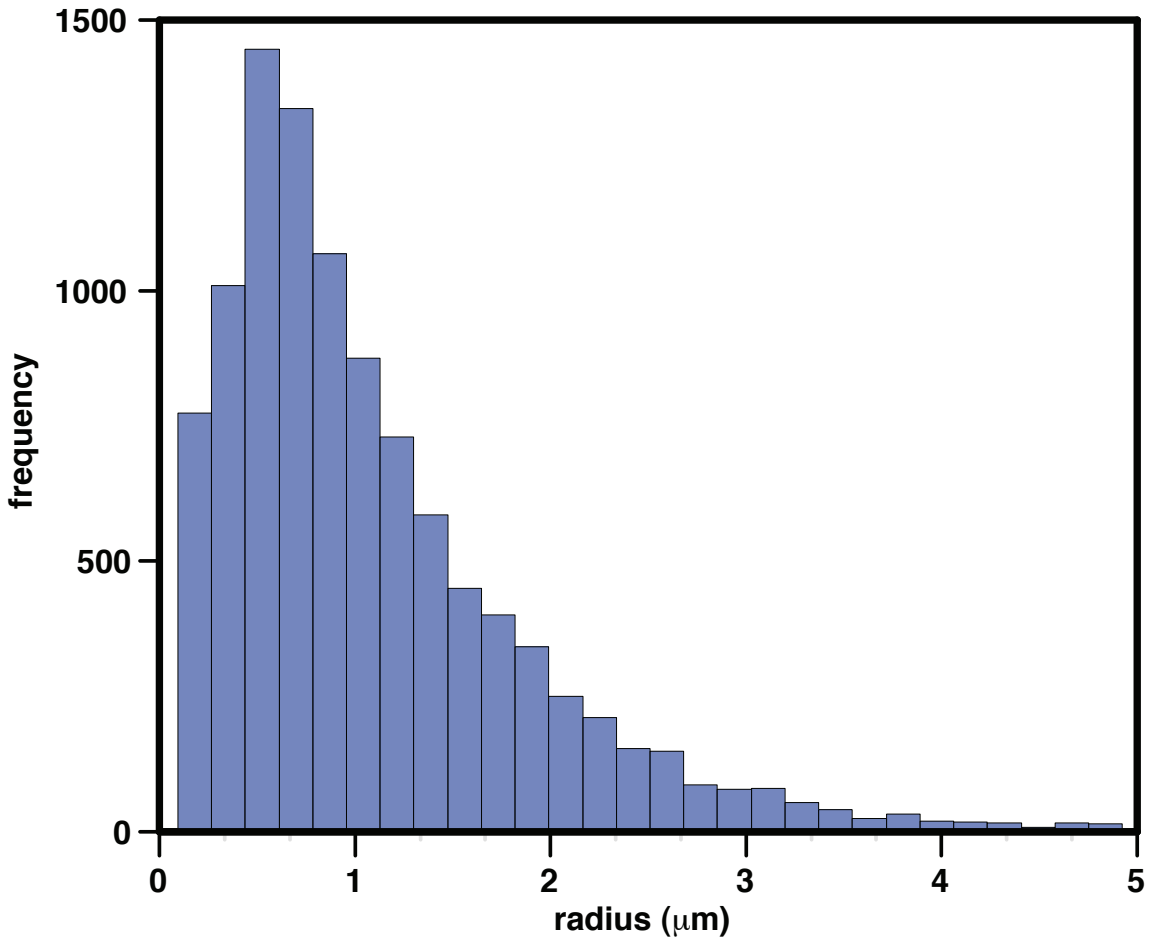

Figure 2 Histogram of fragment size (radius) in the powdered starting material. Mean of analyzed particles is 1.1μm and the median is 0.9μm.

Analyses of experiment products

Experiment products (i.e. charges) consisted of glass and crystals in a semi-spherical shape 4-5 mm in diameter. Charges were mounted in epoxy with the vertical axis parallel to the plane of section and abraded until the maximum diameter cross section of the charge was exposed. The mounts were then polished and carbon coated for imaging on a Leica or Tescan scanning electron microscope (SEM) at the University of North Carolina.

Crystals identified in back-scattered electron (BSE) images of experiment products were digitized (Fig. 3). All plagioclase crystals were digitized because crystals were mostly solitary with well-defined crystal faces and shapes. However, touching crystals were common (~ 10-20% of total crystals), and in those cases boundaries between adjacent plagioclase crystals were assigned by inspection of the crystal shapes and a thin boundary was drawn between different crystals. In the majority of cases involving touching crystals the boundary was easy to identify because of the individual crystal morphologies. Ambiguous situations were rare, accounting for fewer than 10 crystals per image. The uncertainty associated with boundary assignment of plagioclase is small compared to the number of crystals analyzed per image (210 to 1183). However, olivine crystals were difficult to interpret owing to pervasive clumping of crystals, often in long chains. Thus, for olivine we only digitized the largest crystals in the image in order to calculate an integrated growth rate using A_{max} (e.g. Walker et al. 1976; Marsh 1998; Lesher et al. 1999; Brugger and Hammer 2010). Previous studies have used the mean of the 4-10 largest crystals in a sample or experimental charge to calculate the maximum growth rate. We chose to use the median of the 10 largest crystal areas in an image because it is less sensitive to one or two anomalously large crystals.

Binary phase maps (Fig. 3) were produced for the crystals and void space (bubbles and cracks) and then analyzed using the computer program ImageJ. The void area was subtracted from the overall image area in order to obtain the area of glass+crystals for spatial analysis calculations.

Characterization of plagioclase chemical variability was performed at Duke

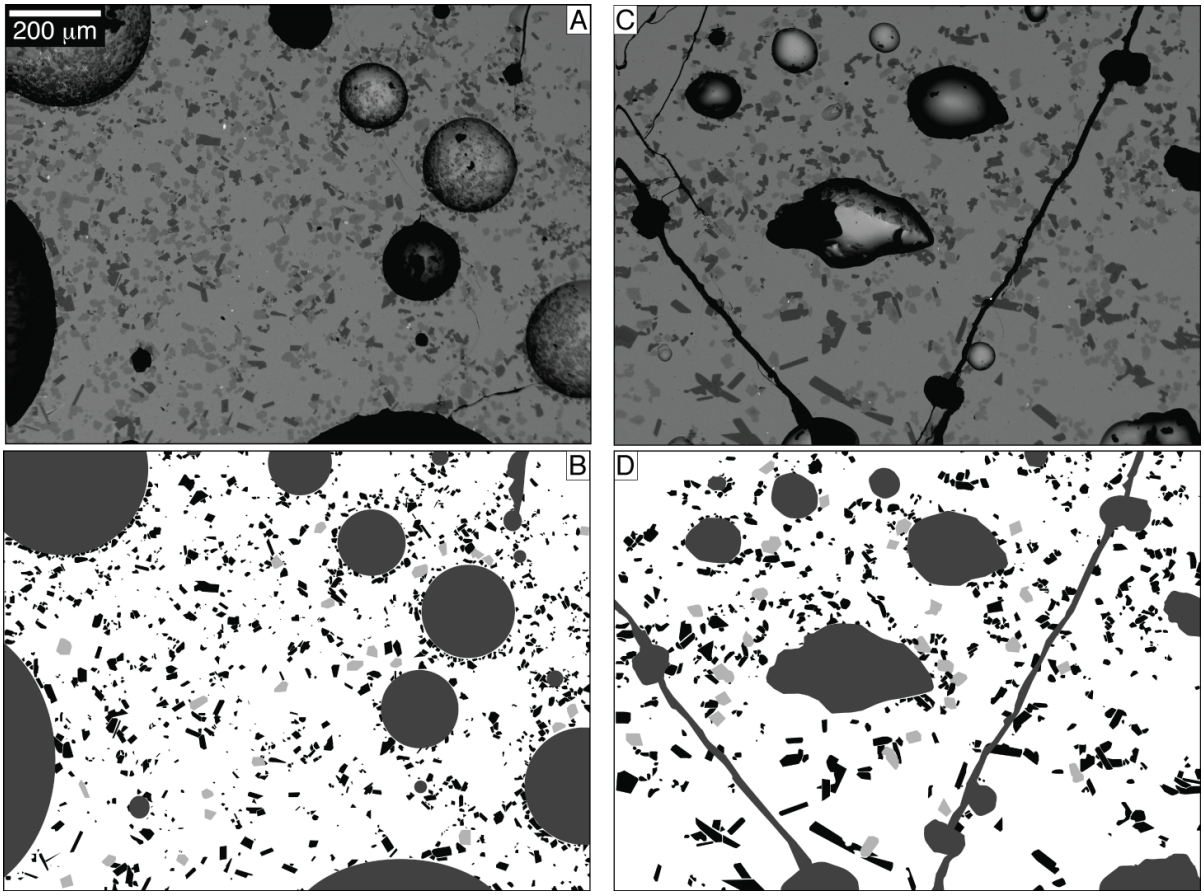

Figure 3 Backscattered electron (BSE) images (A and C) and digitized objects (B and D) of selected experiments. Plagioclase crystals are shown in black, the largest olivine crystals are shown in light gray and bubbles and cracks are shown in dark grey. Pane A is BSE image of experiment 58 (T = 1150ºC, t = 70 h). Pane B is digitized objects from experiment 58. Pane C is BSE image of experiment 56 (T = 1150ºC, t = 70 h, τ = 40 min, α = ± 5ºC) Pane D is digitized objects from experiment 56. Scale is the same for all 4 panes.

University on a Cameca Camebax electron microprobe utilizing Cameca PAP correction software for data reduction. An accelerating voltage of 15 kV and beam current of 15 nA was used for analyses.

Crystal size analyses

The plagioclase area fraction (ϕ) and crystal number density (N_A, mm^{-2}) were obtained from analysis of the binary phase maps. From these two values, estimates of characteristic crystal size (S_N, mm) were calculated using equation 1. Based on intersection probabilities (Underwood 1970) and the lack of crystal foliation, N_A was extrapolated to three dimensions (N_V, mm^{-3}) using equation 2 (Blundy and Cashman 2008). Batch growth rate (G_{batch}, mm/s) was calculated using equation 3 (e.g. Blundy and Cashman 2008; Hammer and Rutherford 2002). The median area of the 10 largest crystals (A_{max}) of plagioclase and olivine were calculated for each image. The median value was then used to calculate G_{max} using equation 4.

$$S_N = (\phi/N_A)^{0.5} \quad (1)$$

$$N_V = N_A/S_N \quad (2)$$

$$G_{batch} = S_N/t \quad (3)$$

$$G_{max} = A_{max}^{0.5}/t \quad (4)$$

CSDs were calculated using CSDCorrections software (Higgins 2000, 2002). CSDs for plagioclase were calculated using the intersection area of each crystal from ImageJ. A shape of 1:2:5 and a roundness parameter of 0.2 were used based on the mode of the intersection width/length and model fit of width/length in CSDcorrections (Higgins 2000). Growth rates were calculated from the CSDs using equation 5 (Marsh 1988).

$$G_{CSD} = \text{slope}^{-1} * t^{1} \quad (5)$$

RESULTS

Qualitative texture variability

Experiments run at short *t* (0.2 and 1 h) consist of crystals from the starting material (augite, plagioclase, olivine, and oxides) and glass produced from melting of starting crystals (Fig. 4). At *t* = 0.2 h all crystals are rounded, and at *t* = 1 h all crystals are rounded except plagioclase, which has locally angular crystal faces (Fig. 4). Iddingsite alteration is locally present on olivine at both *t* = 0.2 and 1 h. Experiment with *t* = 20 h consists of plagioclase, olivine and Mg,Fe,Cr-spinel in glass; augite was eliminated (Fig. 4). Chemical zoning is ubiquitous in plagioclase at *t* = 20 h with starting material plagioclase (An_{60}) normally in the cores of grains and new growth plagioclase (An_{74}) rimming the cores.

Chemical variability from rim to core in plagioclase is minor (< 1 mol%) for experiments greater than 20 h and the vast majority is approximately An_{74}. When a discernible core is present it is in one of the largest crystals in the charge and the core is approximately An_{60}. No chemical variation from rim to core was measured or observed in the olivine grains.

Plagioclase and olivine textures are coarser in all experiments for which the temperature was cycled relative to static experiments of the same duration and mean temperature (e.g. Fig. 3), and experiments with the longest *t* have the coarsest texture. Clumping of crystals is more common as the textures coarsen.

Nucleation sites through time

Plagioclase crystal density (N_V^{plag}) for static experiments decreases rapidly in the first few minutes in the furnace as the starting material partially melts (Fig. 4, 5; Table 1). The number of crystals decreases with increasing duration for all static experiments from 0.2 h to 120 h (Fig. 5).

N_V^{plag} of the oscillating-temperature experiments decreases with increasing α (Fig. 6D; Table 1) at τ = 20 min but does not correlate with τ at α = 5ºC (Fig. 7D; Table 1). The decrease in the number of crystals caused by temperature oscillation is significant; for

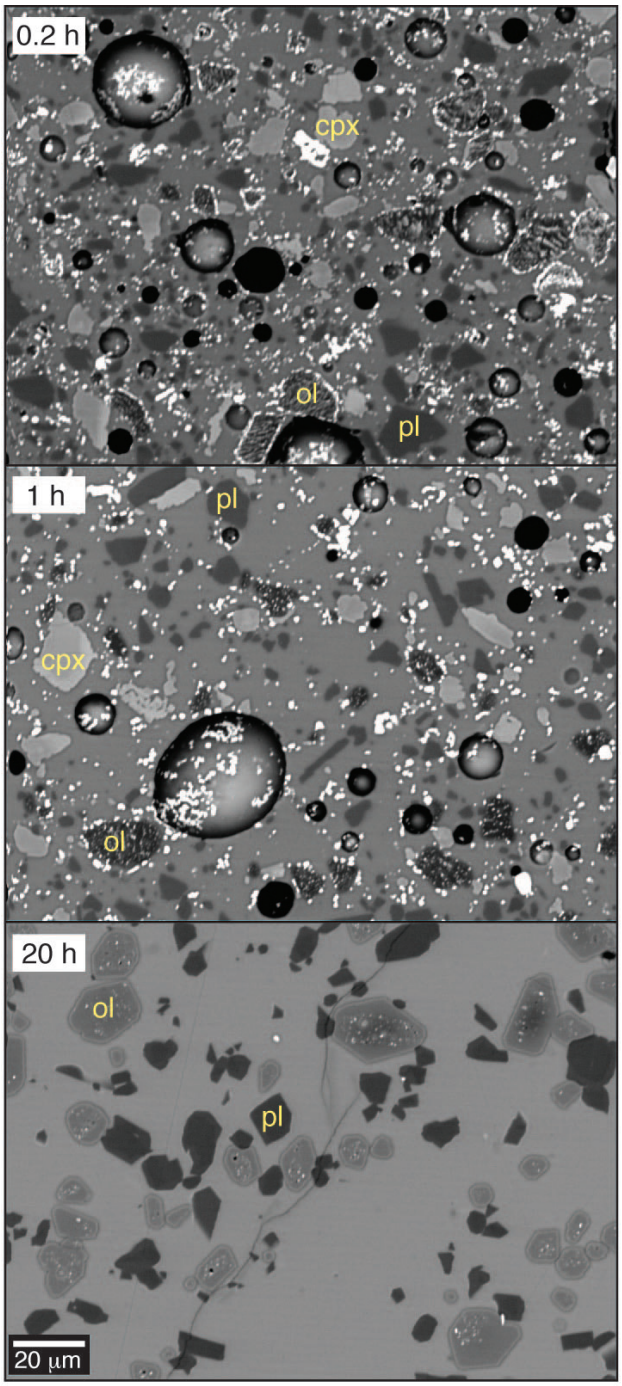

Figure 4 BSE images from static experiment experiments with t = 0.2 h, 1 h and 20 h. Phases indicated in yellow text (cpx=clinopyroxene, ol=olivine, pl=plagioclase). Bright white spots are oxide minerals. Scale is the same for all three images.

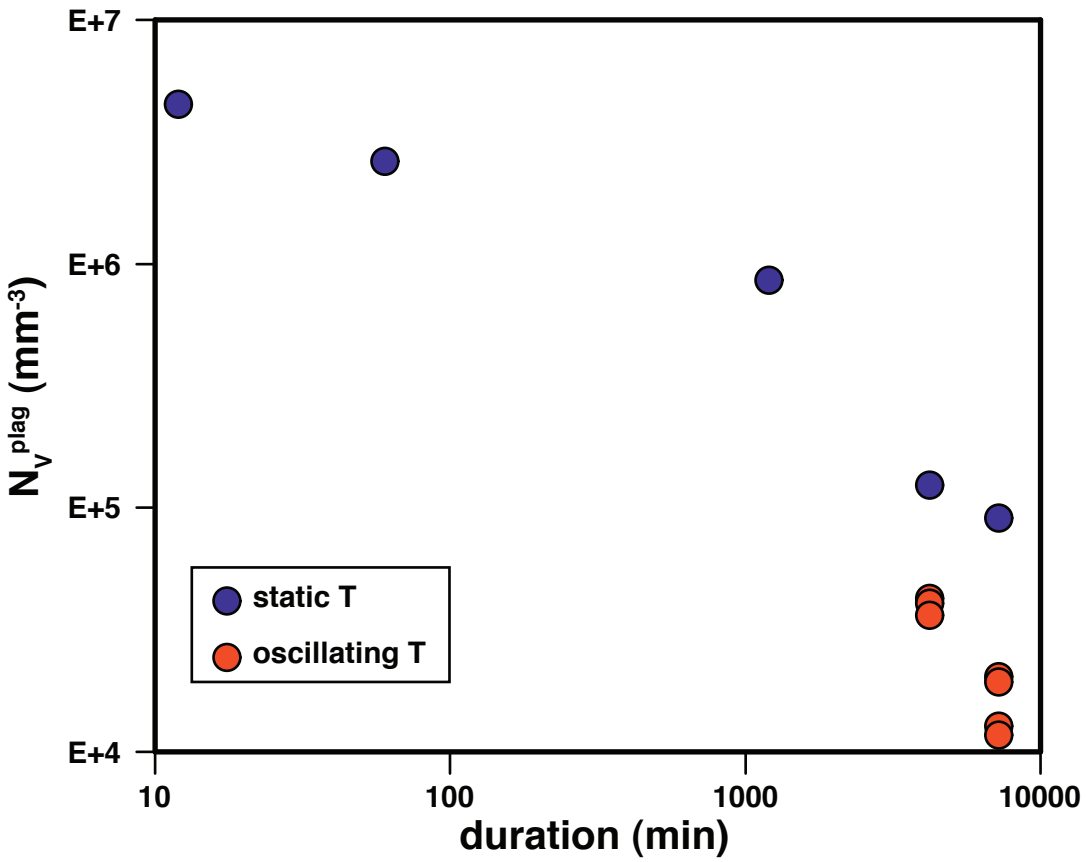

Figure 5 Log-log plot of volume crystal density of plagioclase (N_V^{plag} (mm^{-3})) vs t (min). Static temperature experiments with t = 12 to 7200 mins are plotted. Oscillating temperature experiments with t = 4200 and 7200 mins are plotted.

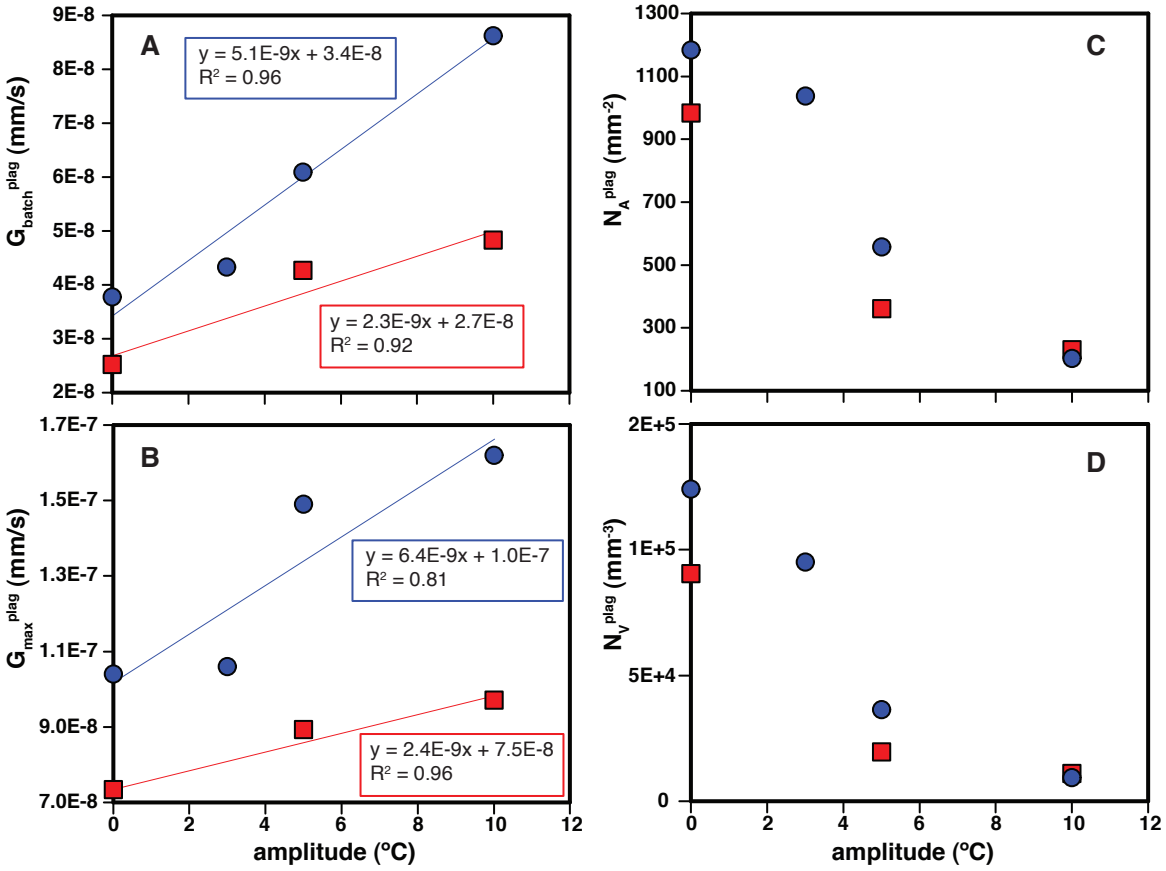

Figure 6 G_{batch}^{plag}, G_{max}^{plag}, N_A^{plag} and N_V^{plag} plotted against α. Blue circles represent experiments with t = 70 h and red squares represent experiments with t = 120 h. All experiments plotted had a mean experimental temperature of 1150ºC and cycled experiments had a τ of 20 min. G_{batch}^{plag} (A) and G_{max}^{plag}, (B) both have a positive correlation with α for t = 70 and 120 h, with a decrease in slope with increasing t. N_A^{plag} (C) and N_V^{plag} (D) both have negative correlations with α.

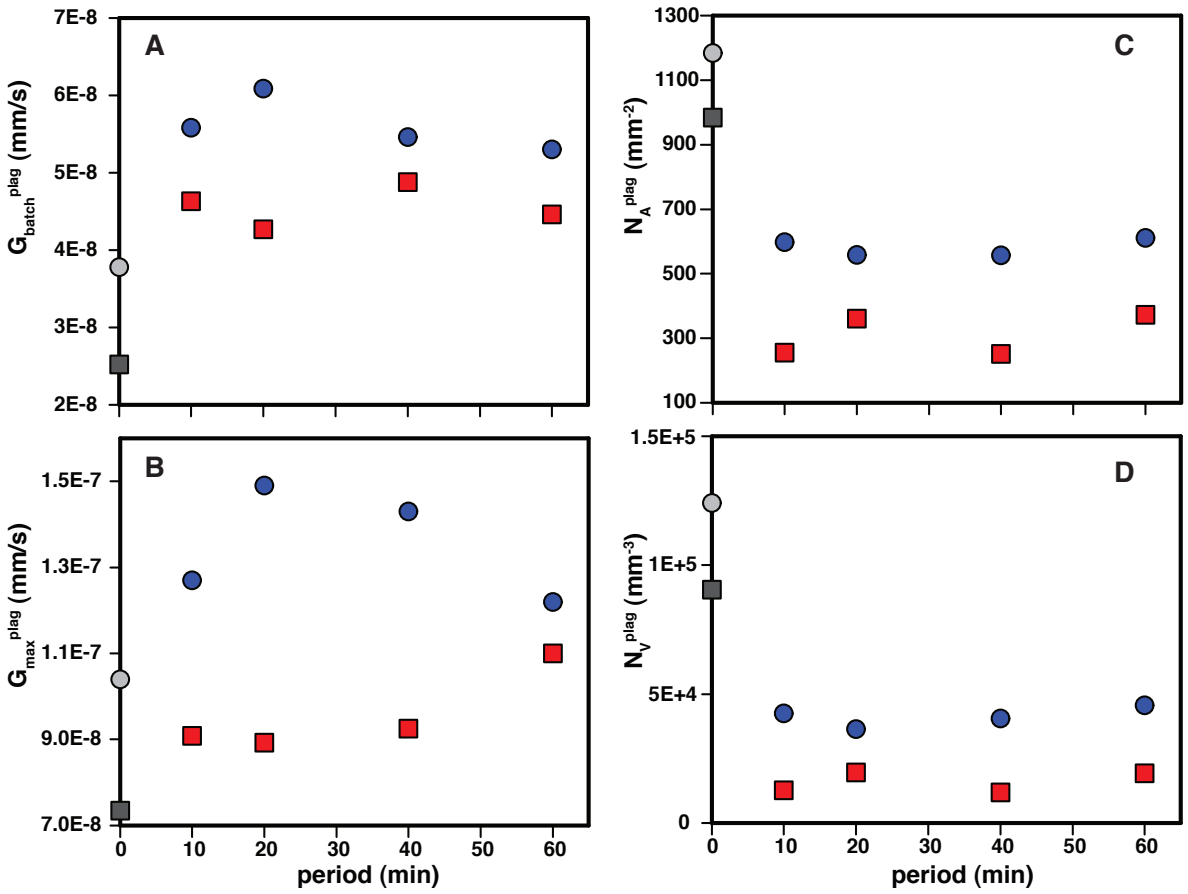

Figure 7 G_{batch}^{plag}, G_{max}^{plag}, N_A^{plag} and N_V^{plag} plotted against τ. Blue circles represent cycled experiments with t = 70 h and red squares represent cycled experiments with t = 120 h. All experiments plotted had a mean experimental temperature of 1150ºC and cycled experiments had α of ± 5ºC. Static experiments (grayscale symbols: 70 h = circle, 120 h = square) are plotted at τ = 0 min for reference. G_{batch}^{plag} (A), G_{max}^{plag} (B), N_A^{plag} (C) and N_V^{plag} (D) do not correlate with τ.

example, N_V^{plag} of the static experiment at 70 h is 3 times the average value of N_V^{plag} for cycled experiments (t = 70 h, α = 5ºC), and N_V^{plag} for the static experiment at 120 h is 6.7 times the average value of N_V^{plag} for cycled experiments (t = 120 h, α = 5ºC).

Plagioclase growth rate

Batch plagioclase growth rate (G_{batch}^{plag}) increases with increasing α (Fig. 6A; Table 1). The slope decreases with time, from $5.1x10^{-9}$ mm/sec/°C at 70 h to $2.3x10^{-9}$ mm/sec/°C at 120 h. However, G_{batch}^{plag} does not correlate with τ (Fig. 7A; Table 1).

Growth rates calculated from the largest plagioclase crystals (G_{max}^{plag}) increase with increasing α (Fig. 6B; Table 1) but do not correlate with τ (Fig. 7B; Table 1). Slopes from linear fits to G_{max}^{plag} variation with α are similar to those for G_{batch}^{plag} and α. For 70 h experiments the slope is $6.4x10^{-9}$ mm/sec/°C and for 120 h experiments the slope is $2.4x10^{-9}$ mm/sec/°C.

CSDs for static T experiments are log-linear except for a turn down at the lowest crystal size bin (Fig. 8) which is not due to resolution of the images (250x) because inspection of charges at higher magnification (1000x) did not indentify additional crystals. CSDs for cycled T experiments have a concave down pattern (Fig. 8). Growth rates calculated from CSDs for select experiments (Fig. 8) are greater than G_{batch}^{plag} and less than G_{max}^{plag}.

Olivine growth rate

$G_{max}^{olivine}$ increases with increasing G_{max}^{plag} and G_{batch}^{plag} for experiments with t = 70 h (Fig. 9; Table 1). There is not a strong correlation between $G_{max}^{olivine}$ and G_{max}^{plag} or G_{batch}^{plag} at 120 h (Fig. 9; Table 1). $G_{max}^{olivine}$ increases with increasing α (Fig. 10A) and a linear fit to the 70 h data has a slope of $7.7x10^{-9}$ mm/sec/°C and a linear fit to the 120 h data has a slope of $3.6x10^{-9}$ mm/sec/°C. $G_{max}^{olivine}$ does not correlate with τ (Fig. 10B).

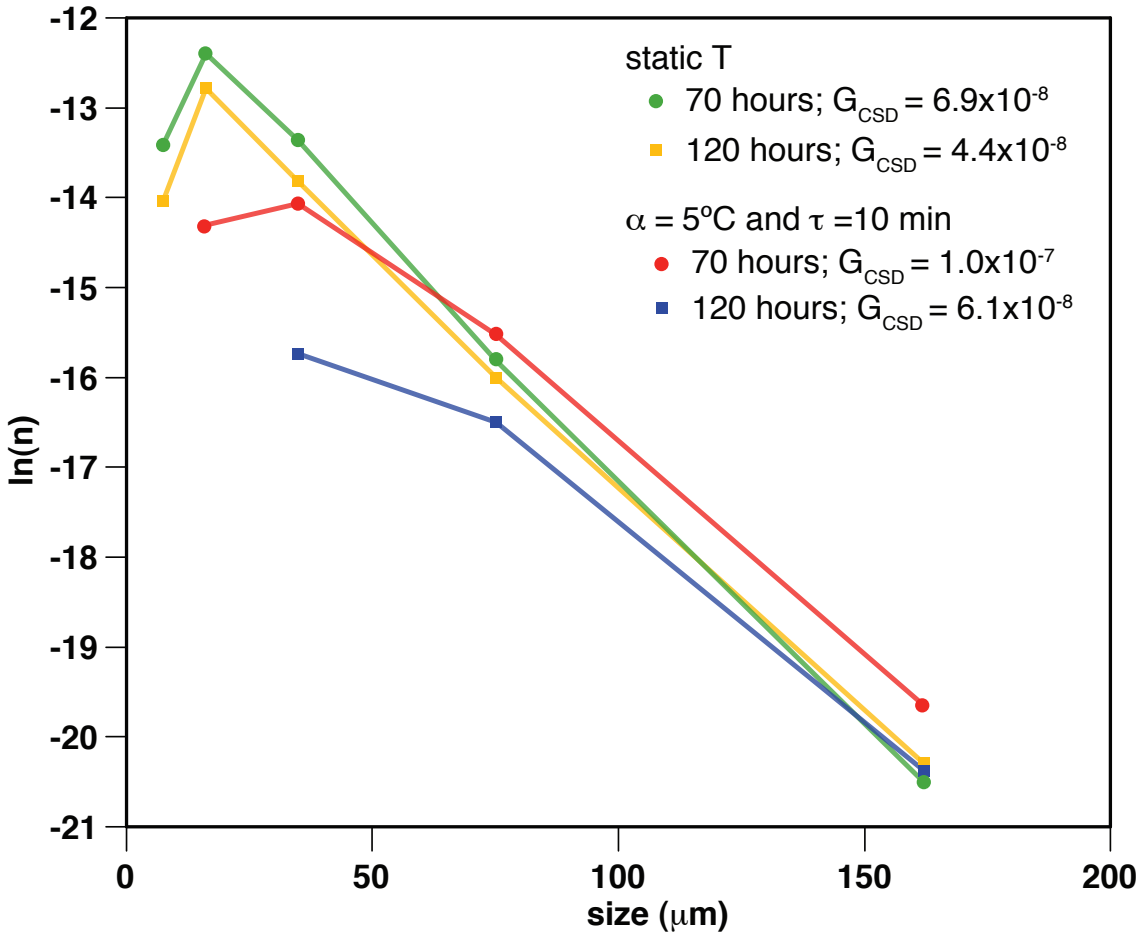

Figure 8 CSD diagram of static temperature experiments with t = 70 and 120 h and cycled temperature experiments (t = 70 and 120 h with τ of 10 min and α of ±5ºC). Calculated G_{CSD} values are listed.

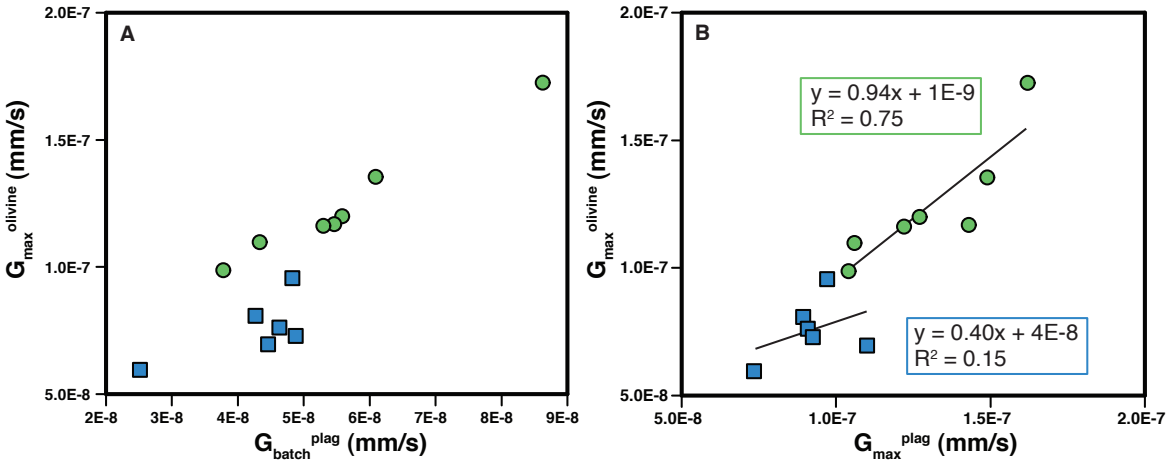

Figure 9 $G_{max}^{olivine}$ plotted against G_{batch}^{plag} (A) and G_{max}^{plag} (B). Green circles represent experiments with t = 70 h and blue squares represent experiments with t = 120 h, all mean T of 1150ºC. Linear fits to the data on B are shown with black lines and the function and R^2 values are shown for both linear fits; box color corresponds to symbol color.

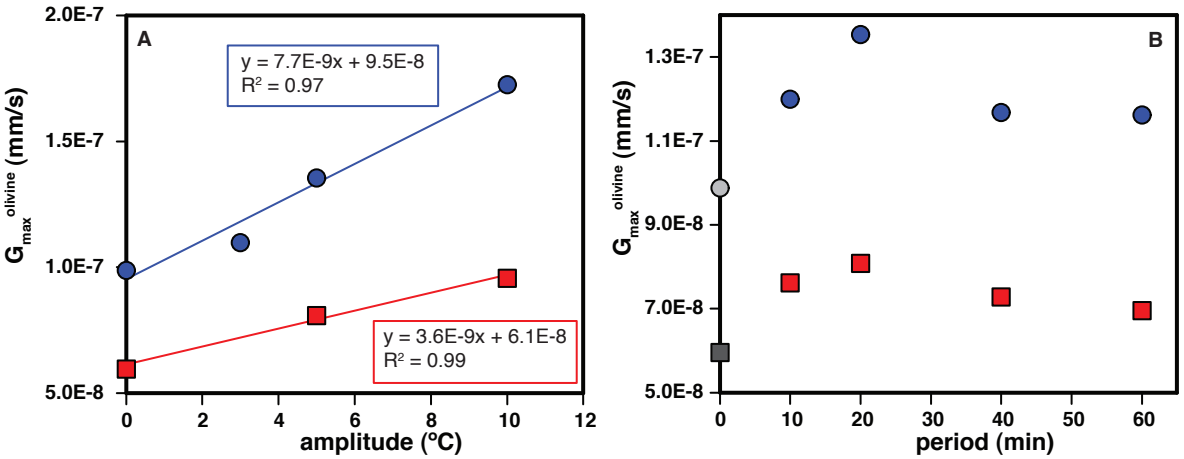

Figure 10 $G_{max}^{olivine}$ plotted against α (A) and τ (B). Blue circles represent experiments with t = 70 h and red squares represent experiments with t = 120 h. Static experiments are shown on B at τ = 0 min for reference.

DISCUSSION

Destruction of nuclei at constant temperature

The decrease in N_V^{plag} with time (Fig. 5) suggests that no nucleation occurs during the experiments. In the magma analog experiments of Mills et al. (2011), direct observation showed that no nucleation occurred during crystal aging under either static or oscillating T, and it is likely that the same crystal destruction processes occurred in our experiments. Destruction of nuclei during static temperature experiments is initially due to partial melting of the starting material and reaction of crystals from the starting material with melt, similar to results from Zieg and Lofgren (2006). The rapid decrease in N_V^{plag} over the first hour of melting (Fig. 5; Table 1) is likely accelerated by the large concentration of dislocations inferred to be in crystals in the starting material, which was crushed to a size near its comminution limit (Glazner and Mills in press). The 20 h experiment consists of euhedral crystals (Fig. 4), and the phase assemblage is the same as phase equilibria experiments using a similar starting material (Ussler and Glazner 1989). This is in contrast to the 1 h experiment that has a diverse phase assemblage inherited from the starting material (Fig. 4). Thus, between 1 and 20 h the starting material has almost completely reacted with the liquid.

After 20 h the decrease in the number of nuclei may be due to the inverse relationship between crystal size and surface energy (Ostwald ripening) which leads to slow destruction of nuclei. Cabane et al. (2005) assessed the role of Ostwald ripening in coarsening of plagioclase in andesite at 1 atmosphere. Although their bulk composition was different, their starting material (glass) was seeded with crystals of plagioclase that were ground to ~1 μm in diameter. Their observed decrease of N_V^{plag} through time was dramatic in the first few hours, similar to our results and to those of Zieg and Lofgren (2006). Thus, in order to compare their Ostwald ripening results with our data we focus on the interval after 20 hours. N_V^{plag} from Cabane et al. (2005) decreased from hour 20 to hour 336 at a rate of -2.3×10^3 $mm^{-3}hr^{-1}$ and our N_V^{plag} decreased from hour 20 to hour 120 at a rate of -7.6×10^3 $mm^{-3}hr^{-1}$ (Fig. 11).

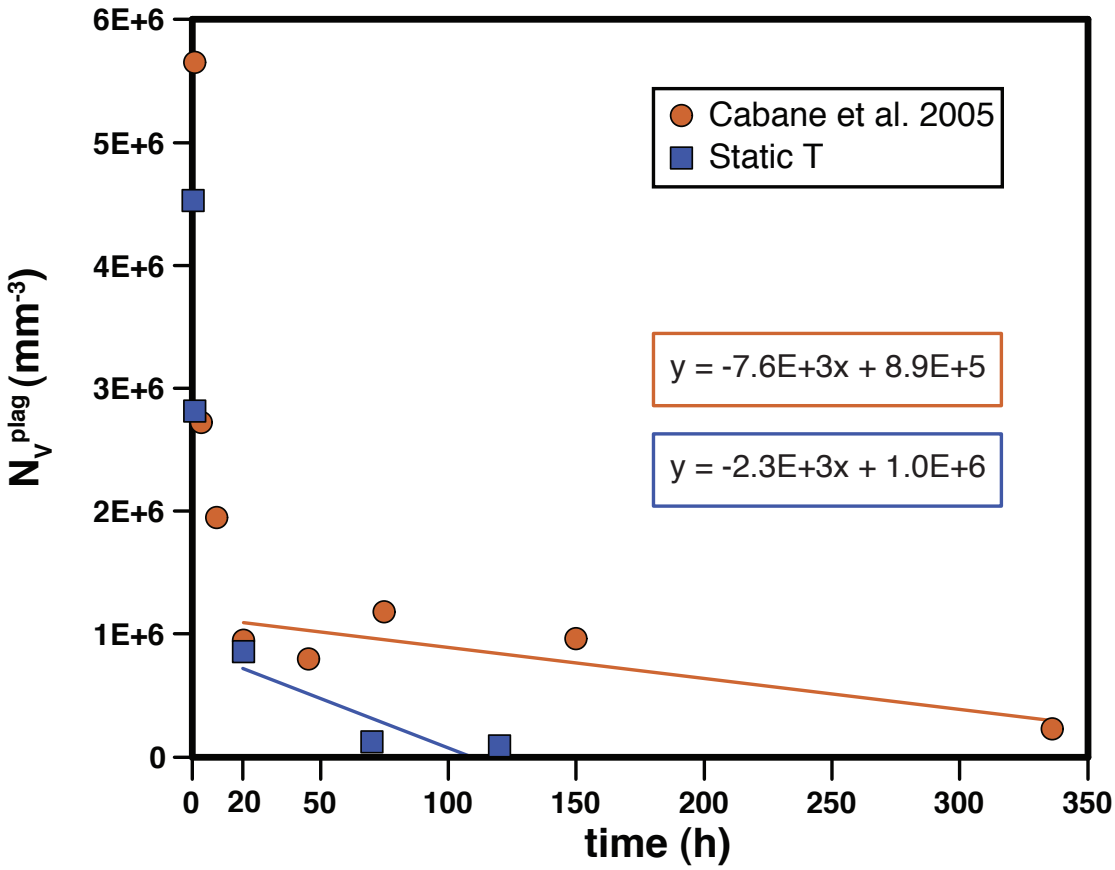

Figure 11 N_V^{plag} from our static-T experiments and static-T experiments of Cabane et al. (2005) plotted against run duration. Best-fit lines were calculated without data for experiments shorter than 20 h; box color corresponds to symbol color.

The difference in these values could be due to the bulk composition, with ripening slowing with increased viscosity (Cabane et al. 2001) owing to decreased diffusion rates (Oishi et al. 1975; Shimizu and Kushiro 1984). The difference may also reflect the greater high-frequency temperature oscillation in our experiments (±1ºC) compared to Cabane et al. (2005) (±0.5ºC). Cabane et al. (2005) discussed the effect of ±0.5ºC temperature oscillation on crystal growth in their experiments and concluded that the coarsening effect was not significant. In our experiments the high frequency temperature oscillations will likely affect only the outer part of the charge, because the skin depth (Turcotte and Schubert 2002, p. 152) for periodic T oscillation with a period of several seconds, using a thermal diffusivity of 0.5 mm^2/sec (Hanley et al. 1978), is on the order of 1 mm.

Effect of temperature cycling on nuclei destruction

Temperature cycling increases the rate at which nuclei are destroyed in the experiments (Figs. 5, 6D, 7D). Dissolution during the up-T portion of the oscillation is one reason for the decrease in nuclei during cycling. Sufficiently small crystals dissolve completely at the high-T point whereas larger crystals survive. Nucleation is suppressed because of the low degree of undercooling during the temperature cycle and the presence of existing nuclei. Work on crystal growth in materials science utilizes this phenomenon to decrease the number of nuclei in the system in order to grow larger crystals (temperature oscillation method; e.g. Hintzmann and Müller-Vogt 1969; Scheel and Elwell 1972).

However, Mills et al. (2011) demonstrated that the dissolution (up-T) part of the cycle does not solely account for the decrease in number of nuclei. Crystals that survive several high-T stands may still progressively decrease in size and eventually disappear. This indicates that another process aids the high-T dissolution and leads to the continued destruction of nuclei. We suggest that during cooling low-energy (large) crystals grow at a faster linear rate than the high-energy (small) crystals. This size-proportional crystal growth (e.g. Canning and Randolph 1967; Eberl et al. 2002) upon cooling leads to a decrease in nuclei after multiple cycles. Cabane et al. (2005) conclude that Ostwald ripening will only affect plagioclase

crystals up to 400 μm^2. However, size-proportional crystal growth appears to affect all crystal sizes (Eberl et al. 2002) and may occur because larger crystals have (1) a greater number of active growth centers on crystal surfaces (Garside et al. 1974) or (2) a greater slip velocity (i.e. relative velocity between crystal and liquid; Canning and Randolph 1967). In addition, growth rate dispersion likely dampens the size-proportional crystal growth signal (Girolami and Rousseau 1985).

Estimating and comparing growth rates

Because of the decrease in crystal number density with time in all our experiments the growth rates we estimated are net growth rates. Our estimates range from G_{batch} to G_{max} with G_{CSD} intermediate between the two; this order is in agreement with results from Brugger and Hammer (2010). The calculation of G based on CSDs for our experiments is subjective because CSDs for our experiments are not log-linear (Fig. 8), and so a decision must be made whether to use only log-linear portions of the distribution or the entire distribution. That decision changes the slope (slope=$G^{-1}t^{-1}$), producing uncertainty in the estimate of G.

G_{max} likely gives the best estimate of gross growth rate because destruction of large crystals is unlikely unless there are external factors favoring growth of nearby crystals, such as temperature gradients. For example, Mills et al. (2011) documented preferential crystal growth, independent of size, for crystals oriented parallel to the direction of heat flow. However, there is no evidence for preferred orientation of crystals in any of our experiments and so we take G_{max} as the best estimate for growth rate.

Comparison between G_{max}^{plag} and $G_{max}^{olivine}$ (Fig. 9B) indicates that experiment *t* decouples growth of the two phases. At 70 h G_{max}^{plag} and $G_{max}^{olivine}$ are positively correlated and fit by a line with a slope of 0.94 (Fig. 9B). At 120 h the data do not define an obvious trend, but there are limited data (Fig. 9B). In addition, the average change in A_{max}^{plag} from 70 h to 120 h for experiments with the same conditions (i.e. α and τ) is 500 μm^2 and for $A_{max}^{olivine}$ it is only 87 μm^2 (Table 1). Thus, coarsening under our experimental conditions is greater for plagioclase than olivine. This is likely due to the absolute temperature difference between the

experimental conditions and the liquidus of plagioclase (~1165ºC) compared to the liquidus of olivine (~1225ºC; Ussler and Glazner 1989). However, feldspars are commonly found as large phenocrysts in porphyritic rocks (e.g. Pirsson 1913) so it is plausible that physiochemical properties of feldspar may accelerate coarsening.

The role of temperature cycling in coarsening igneous textures

Effect of amplitude on coarsening

In cycled experiments N_V^{plag} negatively correlates with α and growth rate positively correlates with α (Fig. 6). The temperature at the high-T point of the cycle (T+α) controls the amount of melting, and thus higher α leads to more dissolution per cycle. Increase in α also leads to greater growth of the largest crystals via size-proportional crystal growth during cooling from T+α to T-α. This process promotes continued destruction of the smallest nuclei. Higher α progressively dissolves larger crystals compared to lower α for a given *t*. However, as the ratio α/τ increases the mean cooling rate on the down-T part of the cycle (4α/τ) increases. Experiments on a synthetic plagioclase system (An_{40}) by Lofgren (1973, 1980) demonstrated that plagioclase morphology is related to cooling rate; at a cooling rate of 2ºC/h tabular crystals dominate, at 32ºC/h arcuate acicular crystals are common, and at 120ºC/h spherulitic crystals formed. Mean cooling rates in our experiments ranged from 20 to 120ºC/h but there was no change in morphology associated with mean cooling rate; plagioclase forms were all tabular to acicular with no spherulitic forms. This suggests that the repeated cycles may have annealed high-energy, ornate spherulites over time.

Effect of period on coarsening

There is little correlation between τ and crystal number density or growth rates at the values of τ we investigated (Fig. 7). This indicates that the proportion of time that the charge spends near the highest-T portion of a cycle does not appear to affect the coarsening process. Diffusion of plagioclase components in the basaltic melt is likely limited by the diffusion

of SiO_2 (Watson 1982). The diffusion coefficient for SiO_2 in basalt is on the order of 10^{-9} cm^2/s (Watson 1982) which equals a linear diffusion rate of 2.5 μm per min. This diffusion rate should be fast enough to transfer solute from small to large crystals (at all investigated periods) when the crystal number density is high or for clustered crystals (Fig. 3). However, the lack of a negative correlation between N_V^{plag} and τ (Fig. 7) suggests that the distance the solute diffuses away from crystal faces has little, or no, effect on coarsening. Ideally, at some threshold the τ will be so short that the diffusion distance will be too small to redistribute the solute except for crystals that are touching. Based on our results in the basaltic system this appears to be a τ less than 10 min. Unfortunately, we were unable to experiment on τ shorter than 10 min because the effective α at the charge would decrease.

At a given T the ratio of crystal growth rate to diffusion rate of relevant components in the liquid will control the τ at which cycling will have a lessened effect on coarsening. For the plagioclase-basaltic melt system we studied that τ is less than 10 min. Diffusion rate inversely scales with melt viscosity (Oishi et al. 1975; Shimizu and Kushiro 1984), so it is likely that plagioclase components in an andesite melt at a similar T below the liquidus will have lower diffusion rates. Thus, the threshold τ of temperature cycling will increase. We can only predict that the threshold τ will increase; it is impossible to determine the magnitude of the increase based on our experiments. Temperature cycling experiments on plagioclase coarsening in andesitic and rhyolitic melts are needed.

The lack of observed variation in nuclei destruction with τ suggests that as long as τ is greater than a threshold value the effect on nuclei destruction and coarsening will be the same. Interestingly, the short threshold τ (<10 min) we found for plagioclase-basalt melt at 1 atmosphere is shorter than periods observed for temperature oscillations in convecting lava lakes (e.g. Wright and Okamura 1977), which are on the order of hours, and much shorter than periodicity of magma input at active volcanoes (e.g. Francis et al. 1993) which are commonly on the order of years.

Model for coarsening by temperature cycling

Our results indicate that crystal coarsening is maximized by large-amplitude temperature oscillations and is insensitive to the magnitude of the cycle period over the range of periods we tested. We speculate that coarsening is accelerated owing to dissolution of small crystals at temperatures above the mean and to size-proportional crystal growth during cooling, in which larger crystals grow faster than smaller crystals. When this process is repeated the integrated result is an increase in mean crystal size and near-complete destruction of small crystals (concave downward CSDs). This process should also refine the crystal population by preferentially dissolving defect-rich crystals or crystals with higher-energy orientations relative to a thermal gradient. This can lead to preferred orientation of crystals (i.e. mineral fabric) if a thermal gradient is present during crystallization (Lundstrom et al 2011; Mills et al. 2011). Also, crystal morphology can change depending on whether the coarsening occurs at static or oscillating T (Brown and Myerson 1989; Mills et al. 2011).

The model of Simakin and Bindeman (2008) for coarsening of crystals in high-silica melts during temperature cycling is based on size-independent growth and size-dependent dissolution. With this model they effectively modeled CSDs of quartz and zircon from rhyolitic magmas. However, our results suggest that the distance crystal components diffuse away from the retreating crystal face during heating has little, or no, effect on coarsening (i.e. no correlation between coarsening and τ) in basaltic magmas. If dissolution is inversely proportional to crystal size then we would expect that as τ increased in our experiments the crystal number density would decrease, and we do not observe this correlation (Fig. 7). In addition, Kile and Eberl (2003) suggested that natural CSDs are typically consistent with size-proportional crystal growth and rarely consistent with size-independent crystal growth. Thus, we prefer a model for coarsening during temperature cycling that is dominantly controlled by size-dependent crystal growth with a minor effect from size-dependent dissolution.

Geologic implications

Silicic igneous rocks with coarsened feldspar textures are common (Pirsson 1913), and Higgins (1998) reevaluated CSDs of Cashman and Marsh (1988) and suggested that plagioclase in a sample from the Makaopuhi lava lake had undergone coarsening. Higgins (1999) and Johnson and Glazner (2010) hypothesized that temperature cycling led to coarsened K-feldspar textures in plutons, and Dunbar et al. (1994) hypothesized that shallow convection in the Mount Erebus lava lake promoted growth of large anorthoclase crystals. Temperature cycling is the likely mechanism for coarsening feldspar in both silicic and mafic rocks because Ostwald ripening is a sluggish mechanism for coarsening plagioclase (Cabane et al. 2005) and cannot produce coarsening patterns in natural CSDs.

Coarsening may be clear from analysis of natural CSDs in some cases (Bindeman 2003) but cryptic in others (Higgins 1998). Caution should be used when estimating time from CSDs based on assumed growth rates because temperature cycling is likely ubiquitous in magma systems and accelerates crystal coarsening which alters growth rates.

CONCLUSIONS

Temperature cycling of a basalt at subliquidus temperatures increases the rate at which plagioclase and olivine coarsen, especially plagioclase. The coarsening of the crystals coincides with a decrease in crystal number density. Coarsening is greater for larger cycle amplitudes but does not appear to correlate with cycle period. We hypothesize that the combined effects of up-T dissolution and size-proportional crystal growth during cooling accelerates coarsening.

Table 1

experiment	mean temperature (ºC)	duration (t; h)	period (τ; min)	amplitude (α; ± ºC)	analyzed area* (mm^2)	plagioclase area (mm^2)	plagioclase mode	number of plagioclase crystals	N_A^{plag} (mm^{-2})	S_N (mm)	G_{batch}^{plag} (mm/s)	N_V^{plag} (mm^{-3})	G_{max}^{plag} (mm/s)	mean plagioclase size (μm^2)	median plagioclase size (μm^2)	A_{max}^{plag} (μm^2)	$A_{max}^{olivine}$ (μm^2)	$G_{max}^{olivine}$ (mm/s)
51	1150	120	0	0	0.81	9.11E-02	0.12	792	984	0.0109	2.52E-08	90521	7.34E-08	115	53	1005	661	5.95E-08
60	1150	120	10	5	0.88	8.68E-02	0.10	224	255	0.0200	4.63E-08	12762	9.08E-08	388	250	1538	1086	7.63E-08
52	1150	120	20	5	0.96	1.15E-01	0.12	347	361	0.0184	4.27E-08	19585	8.93E-08	330	210	1488	1218	8.08E-08
63	1150	120	40	5	0.84	9.08E-02	0.11	210	251	0.0211	4.88E-08	11922	9.25E-08	409	273	1598	991	7.29E-08
62	1150	120	60	5	1.02	1.36E-01	0.14	373	372	0.0193	4.46E-08	19286	1.10E-07	363	209	2247	904	6.96E-08
49	1150	120	20	10	1.13	1.11E-01	0.10	262	231	0.0209	4.83E-08	11075	9.71E-08	424	298	1758	1708	9.57E-08
58	1150	70	0	0	1.00	1.05E-01	0.11	1183	1184	0.0095	3.78E-08	124167	1.04E-07	91	51	691	621	9.89E-08
61	1150	70	10	5	1.13	1.30E-01	0.12	675	598	0.0141	5.58E-08	42549	1.27E-07	199	135	1023	913	1.20E-07
72	1150	70	20	5	1.04	1.36E-01	0.13	578	558	0.0154	6.09E-08	36377	1.49E-07	236	156	1419	1165	1.35E-07
56	1150	70	40	5	1.08	1.11E-01	0.11	603	557	0.0137	5.46E-08	40530	1.43E-07	184	100	1306	867	1.17E-07
79	1150	70	60	5	0.71	7.77E-02	0.11	435	611	0.0134	5.30E-08	45709	1.22E-07	179	113	942	857	1.16E-07
71	1150	70	20	3	1.02	1.26E-01	0.12	1057	1037	0.0109	4.33E-08	95121	1.06E-07	119	76	707	765	1.10E-07
70	1150	70	20	10	1.12	1.07E-01	0.10	227	203	0.0217	8.62E-08	9340	1.62E-07	472	345	1664	1894	1.73E-07
75	1150	20	0	0	0.02	2.31E-03	0.10	98	4153	0.0049	6.75E-08	854787						
76	1150	1	0	0	0.02	2.36E-03	0.10	209	9248	0.0033	9.13E-07	2812268						
77	1150	0.2	0	0	0.02	2.36E-03	0.10	287	12699	0.0028	3.90E-06	4525433						

* analyzed area is the total area of the image minus the area of the bubbles and cracks

REFERENCES

Annen C (2009) From plutons to magma chambers: Thermal constraints on the accumulation of eruptible silicic magma in the upper crust. Earth and Planetary Science Letters 284:409-416

Annen C, Blundy JD, Sparks RSJ (2006) The genesis of intermediate and silicic magmas in deep crustal hot zones. Journal of Petrology 47:505-539

Atwater T, Stock JM (1998) Pacific-North America plate tectonics of the Neogene southwestern United States – an update. International Geological Review 40:375-402

Bachmann O, Bergantz GW (2003) Rejuvenation of the Fish Canyon magma body: A window into the evolution of large-volume silicic magma systems. Geology 31:789-792

Bachmann O, Bergantz GW (2004) On the origin of crystal-poor rhyolites: Extracted from batholith crystal mushes. Journal of Petrology 45:1565-1582

Bachmann O, Bergantz GW (2006) Gas percolation in upper-crustal silicic crystal mushes as mechanism for upward heat advection and rejuvenation of near-solidus magma bodies. Journal of Volcanology and Geothermal Research 149:85-102

Bachmann O, Miller CF, de Silva S (2007) The volcanic-plutonic connection as a stage for understanding crustal magmatism. The Journal of Volcanology and Geothermal Research 167:1-23

Barth AP, Walker JD, Wooden JL, Riggs NR, Schweickert RA (2011) Birth of the Sierra Nevada magmatic arc: Early Mesozoic plutonism and volcanism in the east-central Sierra Nevada of California. Geosphere 7:877-897

Bateman PC, Kistler RW, Peck DL, Busacca AJ (1983) Geologic map of the Tuolumne Meadows Quadrangle, Yosemite National Park, California. U.S. Geological Survey Map GQ-1570, scale 1:62,500

Best MG (1982) Igneous and Metamorphic Petrology. San Francisco, WH Freeman and Company, 630 p

Bindeman IN (2003) Crystal sizes in evolving silicic magma chambers. Geology 31:367-370

Bindeman IN, Valley JW, Wooden JL, Persing HM (2001) Post-caldera volcanism: in situ measurement of U-Pb age and oxygen isotope ratio in Pleistocene zircons from Yellowstone caldera. Earth and Planetary Science Letters 189:197-206

Blundy JD, Cashman KV (2005) Rapid decompression crystallization recorded by melt inclusions from Mount St. Helens volcano. Geology 33:793-796

Blundy JD, Cashman KV (2008) Petrologic reconstruction of magmatic system variables and processes. Rev Mineral Geochem 69:179-239

Boone GM (1959) Significance of oscillatory zoning in alkali and plagioclase feldspars in granodiorite from northern Maine. Geological Society of America Bulletin 70:1571–1572

Boudreau AE, McBirney AR (1997) The Skaergaard layered series; Part III, Non-dynamic layering. Journal of Petrology 38:1003–1020. doi:10.1093/petrology/38.8.1003.

Bouvier A, Vervoort JD, Patchett PJ (2008) The Lu-Hf and Sm-Nd isotopic composition of CHUR: Constraints from unequilibrated chondrites and implications for the bulk composition of terrestrial planets. Earth and Planetary Science Letters 273:48-57

Bowen NL (1928) The evolution of igneous rocks. Princeton University Press Princeton, New Jersey.

Brown PM Myerson AS (1989) The growth, dissolution and aging of terephthalic acid crystals. American Institute of Chemical Engineers Journal 35:1749-1752

Brown SJA, Fletcher IR (1999) SHRIMP U-Pb dating of the preeruption growth history of zircons from the 340 ka Whakamaru Ignimbrite, New Zealand: Evidence for >250 k.y. magma residence times. Geology 27:1035-1038

Brugger CR, Hammer JE (2010) Crystal size distribution analysis of plagioclase in experimentally decompressed hydrous rhyodacite magma. Earth and Planetary Science Letters 200:246-254

Cabane H, Laporte D, Provost A (2001) Experimental investigation of the kinetics of Ostwald ripening of quartz in silicic melts. Contributions to Mineralogy and Petrology 142:361-373

Cabane H, Laporte D, Provost A (2005) An experimental study of Ostwald ripening of olivine and plagioclase in silicate melts: implications for the growth and size of crystals in magmas. Contributions to Mineralogy and Petrology 150:37-53

Campbell SK (1994) A geochemical and strontium isotopic investigation of Laramide and younger igneous rocks in central Colorado, with emphasis on the petrogenesis of the Thirtynine Mile volcanic field, PhD thesis, Tallahassee. Florida State University

Canning TF, Randolph AD (1967) Some aspects of crystallization theory: systems that violate McCabe's delta L law. AIChE Journal. 13:5-10

Cashman KV (1990) Textural constraints on the kinetics of crystallization of igneous rocks. In: Nicholls J, Russell JK (eds) Modern Methods of Igneous Petrology: Understanding Magmatic Processes. Reviews in Mineralogy. Mineralogical Society of America 24:259–314

Cashman KV, Marsh BD (1988) Crystal size distribution (CSD) in rocks and the kinetics and dynamics of crystallization II: Makaopuhi lava lake. Contributions to Mineralogy and Petrology 99:292-305

Chen W, Arculus RJ (1995) Geochemical and isotopic characteristics of lower crustal xenoliths, San Francisco Volcanic Field, Arizona, U.S.A. Lithos 36:203-225

Claiborne LL, Miller CF, Flanagan DM, Clynne MA, Wooden JL (2010) Zircon reveals protracted magma storage and recycling beneath Mount St. Helens. Geology 38:1011-1014

Clemens JD, Helps PA, Stevens G (2010) Chemical structure in granitic magmas – a signal from the source?. Earth and Environmental Science Transactions of the Royal Society of Edinburgh 100:159-172

Colbeck SC (1982) An overview of seasonal snow metamorphism. Reviews of Geophysics and Space Physics 20:45-61

Coleman DS, Gray W, Glazner AF (2004) Rethinking the emplacement and evolution of zoned plutons: Geochronologic evidence for incremental assembly of the Tuolumne Intrusive Suite, California. Geology 32:433-436

Coney PJ, Reynolds SJ (1977) Cordilleran Benioff zones. Nature 270:403-407

Costa F (2008) Residence times of silicic magmas associated with calderas. In: Gottsmann J, Marti J (eds) Developments in Volcanology 10. Caldera Volcanism: analysis, modeling, and response. Elsevier, pp 1-55

Crisp JA (1984) Rates of magma emplacement and volcanic output. Journal of Volcanology and Geothermal Research 20:177-211

Crowley JL, Schoene B, Bowring SA (2007) U-Pb dating of zircon in the Bishop Tuff at the millennial scale. Geology 35:1123-1126

Davis JW, Coleman DS, Gracely JT, Gaschnig R, Stearns M (2012) Magma accumulation rates and thermal histories of plutons of the Sierra Nevada batholith, CA. Contributions to Mineralogy and Petrology 163:449-465

de Silva SL, Gosnold WD (2007) Episodic construction of batholiths: Insights from the spatiotemporal development of an ignimbrite flare-up. Journal of Volcanology and Geothermal Research 67:320-335

DeFrates J, Lundstrom CC, Marshak S (2006) Can diffusion in a thermal gradient produce crystallographic preferred orientation?. Geological Society of America Abstracts with Programs 38:413

Donhowe DP, Hartel RW (1996) Recrystallization of ice cream during controlled accelerated storage. International Dairy Journal 6:1191-1208

Dunbar N, Cashman K, Dupre R (1994) Crystallization processes of anorthoclase phenocrysts in the Mount Erebus magmatic system: evidence from crystal composition, crystal size distributions and volatile contents of melt inclusions. In: Kyle PR (ed) Volcanological and Environmental Studies of Mount Erebus, Antarctica. Antarctica Research Series 66:129-146

Eberl DD, Kile DE, Drits VA (2002) On geological interpretations of crystal size distributions: Constant vs. proportionate growth. American Mineralogist 87:1235-1241

Epis RC, Chapin CE (1975) Geomorphic and tectonic implications of the post-Laramide, late Eocene erosion surface in the Southern Rocky Mountains. In: Curtis, B.F. (ed.) Cenozoic history of the southern Rocky Mountains. Geological Society of America, Memoir 144:45-74

Farmer GL, DePaolo DJ (1984) Origin of Mesozoic and Tertiary granite in the western United States and implications for pre-Mesozoic crustal structure; 2, Nd and Sr isotopic studies of unmineralized and Cu- and Mo-mineralized granite in the Precambrian craton. Journal of Geophysical Research 89:10141-10160

Feldman JD (2010) The emplacement and exhumation history of the Twin Lakes batholith and implication for Laramide orogeny and flat slab subduction, MS thesis, Socorro. New Mexico Institute of Mining and Technology, New Mexico, p 174

Francis P, Oppenheimer C, Stevenson D (1993) Endogenous growth of persistently active volcanoes. Nature 366:554-557

Fridrich CJ, DeWitt E, Bryant B, Steve R, Smith RP (1998) Geologic map of the Collegiate Peaks Wilderness Area and the Grizzley Peak caldera, Sawatch Range, central Colorado. U. S. Geological Survey, Miscellaneous Investigations Series map I-2565, scale 1:5000, 29 p.

Garcia RV (2011) Cenozoic intrusive and exhumation history of the Elk and West Elk Mountain plutons, southwest Colorado, MS thesis, Socorro. New Mexico Institute of Mining and Technology, New Mexico, p 143

Garside J, Mullin JW, Das SN (1974) Growth and dissolution kinetics of potassium sulfate crystals in an agitated vessel. Ind. Eng. Chem. 13:299-305

Girolami MW, Rousseau RW (1985) Size-dependent crystal growth - a manifestation of growth rate dispersion in the potassium alum - water system. AIChE Journal 31:1821-1828

Glazner AF (1991) Plutonism, oblique subduction, and continental growth: An example from the Mesozoic of California. Geology 19:784-786

Glazner AF, Bartley JM, Coleman DS, Gray W, Taylor RZ (2004) Are plutons assembled over millions of years by amalgamation from small magma chambers?. GSA Today 14:4-11

Glazner AF, Coleman DS, Bartley JM (2008) The tenuous connection between high-silica rhyolites and granodiorite plutons. Geology 36:183-186

Glazner AF, Bartley JM, Law B, Coleman DS (2011) The granite aqueduct and advection of water and heat through plutonic terranes. AGU Fall Meeting, San Francisco

Glazner AF, Mills RD (in review) Statistics of two-dimensional cuts through objects with a fractal size distributions: application to xenoliths, breccias, and enclaves. Geosphere

Hall J (1805) Experiments on whinstone and lava. Transactions of the Royal Society of Edinburgh 5:43–75

Hammarstrom JM, Zen E (1986) Aluminum in hornblende: An empirical igneous barometer. American Mineralogist 71:1297-1313

Hammer JE, Rutherford MJ (2002) An experimental study of the kinetics of decompression-induced crystallization in silicic melts. Journal of Geophysical Research 197:1-23

Hanley EJ, DeWitt DP, Roy RF (1978) The thermal diffusivity of eight well-characterized rocks for the temperature range 300-1000 K

Hersum TG, Marsh BD (2007) Igneous textures: On the kinetics behind the words. Elements 3:247–252. doi:10.2113/gselements.3.4.247

Higgins MD (1998) Origin of anorthosite by textural coarsening: quantitative measurements of a natural sequence of textural development. Journal of Petrology 39:1307-1323

Higgins MD (1999) Origin of megacrysts in granitoids by textural coarsening: a crystal size distribution (CSD) study of microcline in the Cathedral Peak Granodiorite, Sierra Nevada, California. Geological Society, London, Special Publications 168:207-219

Higgins MD (2000) Measurement of crystal size distributions. American Mineralogist 85:1105-1116

Higgins MD (2002) A crystal size-distribution study of the Kiglapait layered mafic intrusion, Labrador, Canada: evidence for textural coarsening. Contributions to Mineralogy and Petrology 144:314-330

Higgins MD (2010) Imaging birefringent minerals without extinction using circularly polarized light. Canadian Mineralogist 48:231–235. doi:10.3749/canmin.48.1.231

Higgins MD (2011a) Textural coarsening in igneous rocks. International Geology Review 53:354-376

Higgins MD (2011b) Quantitative petrological evidence for the origin of K-feldspar megacrysts in dacites from Taapaca volcano, Chili. Contributions to Mineralogy and Petrology 162:709-723

Higgins MD, Chandrasekharam D (2007) Nature of sub-volcanic magma chambers, Deccan Province, India: evidence from quantitative textural analysis of plagioclase megacrysts in Giant Plagioclase Basalts. Journal of Petrology 48:885-900

Hildreth W (2004) Volcanological perspectives on Long Valley, Mammoth Mountain, and Mono Craters: several contiguous but discrete systems. Journal of Volcanology and Geothermal Research 136:169–198

Hintzmann W, Müller-Vogt G (1969) Crystal growth and lattice parameters of rare-earth doped yttrium phosphate, arsenate and vanadate prepared by the oscillating temperature flux technique. Journal of Crystal Growth 5:274-278

Huang F, Lundstrom CC, Glessner J, Ianno A, Boudreau A, Li J, Ferre EC, Marshak S, DeFrates J (2009) Chemical and isotopic fractionation of wet andesite in a temperature gradient; experiments and models suggesting a new mechanism of magma differentiation. Geochimica et Cosmochimica Acta 73:729–749. doi:10.1016/j.gca.2008.11.012

Hughes WT (1986) Geochemical evolution of basalts from Amboy and Pisgah lava fields, Mojave Desert, California. MS Thesis, University of North Carolina, Chapel Hill

Huppert HE, Sparks RSJ (1998) The generation of granitic magmas by intrusion of basalt into the continental crust. Journal of Petrology 29:599-624

Iddings JP (1909) Igneous Rocks vol. 1. New York, John Wiley and Sons

Jerram DA, Higgins MD (2007) 3D analysis of rock textures; quantifying igneous microstructures. Elements 3:239–245. doi:10.2113/gselements.3.4.239

Johnson BR, Glazner AF (2010) Formation of K-feldspar megacrysts in granodioritic plutons by thermal cycling and late-stage textural coarsening. Contributions to Mineralogy and Petrology 159:599-619

Kile DE, Eberl DD (2003) On the origin of size-dependent and size-independent crystal growth: influence of advection and diffusion. American Mineralogist 88:1514-1521

Kirkpatrick RJ (1977) Nucleation and growth of plagioclase, Makaopuhi and Alae lava lakes, Kilauea Volcano, Hawaii. Geological Society of America Bulletin 88:78-84

Klemetti EW, Cooper KM (2007) Cryptic young zircon and young plagioclase in the Kaharoa Rhyolite, Tarawera, New Zealand: Implications for crystal recycling in magmatic systems. American Geophysical Union, Fall Meeting

Krogh TE (1973) A low-contamination method for hydrothermal decomposition of zircon and extraction of U and Pb for isotopic age determinations. Geochim Cosmochim Acta 37:485-494

Kuiper KF, Deino A, Hilgen FJ, Krijgsman W, Renne PR, Wijbrans JR (2008) Synchronizing rock clocks of earth history. Science 320:500-504

Lesher CE, Cashman KV, Mayfield JD (1999) Kinetic controls on crystallization of Tertiary North Atlantic basalt and implications for the emplacement and cooling history of lava at Site 989, Southeast Greenland rifted margin. Proceedings Ocean Drilling Program 163:135-148

Lipman PW (2007) Incremental assembly and prolonged consolidation of Cordilleran magma chambers: evidence from the Southern Rocky Mountain volcanic field. Geosphere 3:42-70

Lipman PW, McIntosh WC (2008) Eruptive and noneruptive calderas, northeastern San Juan Mountains, Colorado: Where did the ignimbrites come from? Geological Society of America Bulletin 120:771-795

Lofgren GE (1973) Experimental crystallization of synthetic plagioclase at prescribed cooling rates. EOS Trans. AGU 54:482

Lofgren GE (1980) Experimental studies on the dynamic crystallization of silicate melts. In: Hargraves RB (ed) The Physics of Magmatic Processes, Princeton, pp 487-551

Lofgren GE, Donaldson CH, Williams RJ, Mullins O, Usselman TM (1974) Experimentally produced textures and mineral chemistry of Apollo 15 quartz normative basalts. Lunar Planet Sci Conf 5:549-568

Lundstrom CC, Marshak S, DeFrates J, Mabon J (2011) Alternative processes for developing fabric and mineral compositional zoning in intrusive rocks. International Geology Review 53:377-405

Mangan MT (1990) Crystal size distribution systematics and the determination of magma storage times: the 1959 eruption of Kilauea Volcano. Journal of Volcanology and Geothermal Research 44:295-302

Marsh BD (1998) On the interpretation of crystal size distributions in magmatic systems. Journal of Petrology 39:553-599

Martin D, Griffiths RW, Campbell IH (1987) Compositional and thermal convection in magma chambers. Contributions to Mineralogy and Petrology 96:465-475

Mattinson JM (1973) Anomalous isotopic composition of lead in young zircons. Carnegie Institute of Washington Year Book 72:613-616

Mattinson JM (2005) Zircon U-Pb chemical abrasion ("CA-TIMS") method: combining annealing and multi-step partial dissolution analysis for improved precision and accuracy of zircon ages. Chemical Geology 220:47-66

Matzel JEP, Bowring SA, Miller RB (2006) Time scales of pluton construction at differing crustal levels: examples from the Mount Stuart and Tenpeak intrusions, North Cascades, Washington. Geological Society of America Bulletin 118:1412-1430

McDonough WF, Sun SS (1995) The composition of the Earth. Chemical Geology 120:223-253

McIntosh WC, Chapin CE (2004) Geochronology of the central Colorado volcanic field. New Mexico Bureau of Geology and Mineral Resources, Bulletin 160:205-237

McQuarrie N, Oskin M (2010) Palinspastic restoration of NAVDat and implications for the origin of magmatism in southwestern North America. Journal of Geophysical Research 115: B10401

Means WD, Park Y (1994) New experimental approach to understanding igneous texture. Geology 22:323–326

Menand T (2008) The mechanics and dynamics of sills in layered elastic rocks and their implications for the growth of laccoliths and other igneous complexes. Earth and Planetary Science Letters 267:93-99

Menand T (2011) Physical controls and depth of emplacement of igneous bodies: A review. Tectonophysics 500:11-19

Michel J, Baumgartner L, Putlitz B, Schaltegger U, Ovtcharova M (2008) Incremental growth of the Patagonian Torres del Paine laccolith over 90 k.y. Geology 36:459-462

Miller JS, Glazner AF, Walker JD, Martin MW (1995) Geochronologic and isotopic evidence for Triassic-Jurassic emplacement of the eugeoclinal allochthon in the Mojave Desert region, California. Geological Society of America Bulletin 107:1441-1457

Miller JS, Matzel JEP, Miller CF, Burgess SD, Miller RB (2007) Zircon growth and recycling during the assembly of large composite arc plutons. Journal of Volcanology and Geothermal Research 167:282-299

Mills RD, Glazner AF, Coleman DS (2008) Comparing the compositional patterns of volcanic and plutonic rocks using the NAVDAT database. Geochimica et Cosmochimica Acta 72:A631

Mills RD, Ratner JJ, Glazner AF (2011) Experimental evidence for crystal coarsening and fabric development during temperature cycling. Geology 39:1139-1142

Mills RD, Glazner AF (2011) Experimental evidence for coarsening of crystals and bubbles during thermal cycling of mafic and silicic magmas. Goldschmidt Conference Abstracts, Mineralogical Magazine, 75:1475

Morgan SS (1998) Pluton emplacement, aureole deformation and metamorphism, and regional deformation within the White-Inyo Range of eastern California, PhD thesis, Blacksburg. Virginia Polytechnic Institute and State University, Virginia, p 172

Morgan S, Stanik A, Horsman E, Tikoff B, de Saint Blanquat M, Habert G (2008) Emplacement of multiple sheets and wall rock deformation: Trachyte Mesa intrusion, Henry Mountains, Utah. Journal of Structural Geology 30:491-512

Mundil R, Ludwig KR, Metcalfe I, Renne PR (2004) Age and timing of the Permian mass extinctions: U/Pb dating of closed system zircons. Science 305:1760-1763

Mutschler FE, Larson EE, Bruce RM (1987) Laramide and younger magmatism in Colorado- New petrologic and tectonic variations on old themes. In: Drexler JW, Larson EE (eds) Cenozoic volcanism in the Southern Rocky Mountains updated: A tribute to Rudy C. Epis- Part 1, Colorado School of Mines Quarterly 82:1-47

Obradovich JD, Mutschler FE, Bryant B (1969) Potassium-Argon Ages Bearing on the Igneous and Tectonic History of the Elk Mountains and Vicinity, Colorado: A Preliminary Report. Geological Society of America Bulletin 80:1749-1756

Oishi Y, Terai R, Ueda H (1975) Oxygen diffusion in liquid silicates and relation to their viscosity. In: Cooper AR, Heuer AH (eds) Mass Transport Phenomena in Ceramics, Plenum Press, NY pp 297-310

Parrish RP (1987) An improved micro-capsule for zircon dissolution in U-Pb geochronology. Chemical Geology 66:99-102

Parrish RP, Krogh TE (1987) Synthesis and purification of ^{205}Pb for U-Pb geochronology. Chemical geology 66:103-110

Peck DL, Wright TL, Moore JG (1966) Crystallization of tholeiitic basalt in Alae lava lake, Hawaii. Bulletin of Volcanology 29:629–655. doi:10.1007/BF02597182.

Pirsson LV (1913) Rocks and rock minerals: a manual of the elements of petrology without the use of the microscope. John Wiley and Sons, New York

Pitcher, W.S., and Berger, A.R., 1972, The geology of Donegal: A study of granite emplacement and unroofing, Regional geology series: New York, Wiley-Interscience, 435 p.

Pupier E, Duchene S, Toplis MJ (2008) Experimental quantification of plagioclase crystal size distribution during cooling of basaltic liquid. Contributions to Mineralogy and Petrology 155:555-570

Randolph AD, Larson MA (1971) Theory of Particulate Processes. Academic Press New York

Reid MR, Coath CD (2000) In situ U-Pb ages of zircons from the Bishop Tuff: No evidence for long crystal residence times. Geology 28:443-446

Reid MR, Coath CD, Harrison TM, McKeegan KD (1997) Prolonged residence times for the youngest rhyolites associated with Long Valley Caldera: ^{230}Th-^{238}U ion microprobe dating of young zircons. Earth and Planetary Science Letters 150:27-39

Renne PR (2006) Progress and challenges in K-Ar and ^{40}Ar/^{39}Ar geochronology. In: Olszewski T (ed) Geochronology: emerging opportunities. Paleont Soc Pap 12:47-66

Renne PR, Mundil R, Balco G, Min K, Ludwig KR (2010) Joint determination of ^{40}K decay constants and ^{40}Ar*/^{40}K for the Fish Canyon sanidine standard and improved accuracy for ^{40}Ar/^{39}Ar geochronology. Geochim Cosmochim Acta 74:5349-5367

Saleeby JB, Kistler RW, Longiaru S, Moore JG, Nokleberg WJ (1990) Middle Cretaceous silicic metavolcanic rocks in the Kings Canyon area, central Sierra Nevada, California. In: Anderson JL (ed) The nature and origin of Cordilleran magmatism, Geological Society of America Memoir 174:251-270

Salisbury MJ, Bohrson WA, Clynne MS, Ramos FC, Hoskin P (2008) Multiple plagioclase crystal populations identified by crystal size distribution and in situ chemical data: implications for timescales of magma chamber processes associated with the 1915 eruption of Lassen Peak, CA. Journal of Petrology 49:1755-1780

Scheel HJ, Elwell D (1972) Stable growth rates and temperature programming in flux growth. Journal of Crystal Growth 12:153-161

Scherer E, Münker C, Mezger K (2001) Calibration of the lutetium-hafnium clock. Science 293:683-687

Schiavi F, Walte N, Keppler H (2009) First in situ observation of crystallization processes in a basaltic-andesitic melt with the moissanite cell. Geology 37:963-966

Schmitt AK, Grove M, Harrison TM, Lovera O, Hulen J, Walters M (2003a) The Geysers-Cobb Mountain Magma System, California (Part 1): U-Pb zircon ages of volcanic rocks, conditions of zircon crystallization and magma residence times. Geochimica et Cosmochimica Acta 67:3423-3442

Schmitt AK, Grove M, Harrison TM, Lovera O, Hulen J, Walters M (2003b) The Geysers-Cobb Mountain Magma System, California (Part 2): Timescales of pluton emplacement and implications for its thermal history. Geochimica et Cosmochimica Acta 67:3443-3458

Schmitz MD, Bowring SA (2001) U-Pb zircon and titanite systematics of the Fish Canyon Tuff: an assessment of high precision U-Pb geochronology and its application to young volcanic rocks. Geochim Cosmochim Acta 65:2571-2587

Schmitz MD, Schoene B (2007) Derivation of isotope ratios, errors, and error correlations for U-Pb geochronology using 205Pb-235U-(233U)-spiked isotope dilution thermal ionization mass spectrometric data. Geochemistry Geophysics Geosystems 8 Q08006

Shannon JR (1988) Geology of the Mount Aetna cauldron complex, Sawatch Range, Colorado, PhD thesis, Golden. Colorado, Colorado School of Mines, p 439

Shannon JR, Epis RC, Naeser CW, Obradovich JD (1987) Correlation of intracaldera and outflow tuffs and an intrusive tuff dike related to the Oligocene Mount Aetna cauldron, central Colorado. In Drexler JW, Larson EE (eds) Cenozoic volcanism in the Southern Rocky Mountains revisited, Colorado School of Mines, Quarterly 82:65-80

Shelley D (1993) Igneous and Metamorphic Rocks under the Microscope. London, Chapman & Hall

Shimizu N, Kushiro I (1984) Diffusivity of oxygen in jadeite and diopside melts at high pressures. Geochimica et Cosmochimica Acta 48:1295-1303

Simakin AG, Bindeman IN (2008) Evolution of crystal sizes in the series of dissolution and precipitation events in open magma systems. Journal of Volcanology and Geothermal Research 177:997-1010

Simon JI, Reid MR (2005) The pace of rhyolite differentiation and storage in an 'archetypical' silicic magma system, Long Valley, California. Earth and Planetary Science Letters 135:123-140

Simon JI, Renne PR, Mundil R (2008) Implications of pre-eruptive magmatic histories of zircons for U-Pb geochronology of silicic extrusions. Earth and Planetary Science Letters 266:182-194

Sisson TW, Ratajeski K, Hankins WB, Glazner AF (2005) Voluminous granitic magmas from common basaltic sources. Contributions to Mineralogy and Petrology 148:635-661

Smith RL (1979) Ash-flow magmatism. In: Chapin CE, Elston WE (eds) Ash-flow tuffs, Geological Society of America Special Paper 180:5-27

Söderlund U, Patchett PJ, Vervoort JD, Isachsen CE (2004) The ^{176}Lu decay constant determined by Lu-Hf and U-Pb isotope systematics of Precambrian mafic intrusions. Earth and Planetary Science Letters 219:311-324

Spera FJ, Crisp JA (1981) Eruption volume, periodicity, and caldera area: Relationships and inferences on development of compositional zonation in silicic magma chambers. Journal of Volcanology and Geothermal Research 11:169-187

Steiger RH, Jager E (1977) Subcommision of geochronology; convention on the use of decay constants in geo- and cosmo-chemistry. Earth and Planetary Science Letters 36:359-362

Stein HJ (1985) A lead, strontium, and sulfur isotope study of Laramide-Tertiary intrusions and mineralization in the Colorado Mineral Belt with emphasis on Climax-type porphyry molybdenum systems plus a summary of other newly acquired isotopic and rare earth element data, PhD thesis, Chapel Hill. North Carolina, University of North Carolina, p 493

Stein HJ, Crock JG (1988) Late Cretaceous-Tertiary magmatism in the Colorado Mineral Belt; Rare earth element and samarium-neodymium isotopic studies. In: Anderson JL (ed) The nature and origin of Cordilleran magmatism, Geological Society of America Memoir 174:195-223

Sun SS, McDonough WF (1989) Chemical and isotopic systematics of oceanic basalts: implications for mantle composition and processes. Geological Society, London, Special Publications 42:313-345

Tappa MJ, Coleman DS, Mills RD, Samperton KM (2011) The plutonic record of a silicic ignimbrite from the Latir volcanic field, New Mexico. Geochemistry Geophysics Geosystems 12 Q10011

Toulmin P, Hammarstrom JM (1990) Geology of the Mount Aetna volcanic center, Chaffee and Gunnison Counties, Colorado. US Geological Survey Bulletin 1864

Turcotte DL, Schubert G (2002) Geodynamics. Cambridge University Press, Cambridge

Tweto O (1979) Geologic Map of Colorado. US Geological Survey Special Map scale 1:500,000

Underwood E (1970) Quantitative Stereology. Addison-Wesley, Massachusetts, 274 pp

Ussler W, Glazner AF (1989) Phase equilibria along a basalt-rhyolite mixing line: implications for the origin of calc-alkaline intermediate magmas. Contributions to Mineralogy and Petrology 101:232-244

Vernon RH (1986) K-feldspar megacrysts in granites: Phenocrysts, not porphyroblasts. Earth-Science Reviews 23:1–63

Voorhees PW (1985) The theory of Ostwald ripening. Journal of Statistical Physics 38:231-252

Walker D, Kirkpatrick RJ, Longhi J, Hays JF (1976) Crystallization history of lunar picritic basalt sample 12002: phase-equilibria and cooling-rate studies. Geological Society of America Bulletin 87:646-656

Walker D, Jurewicz S, Watson EB (1988) Adcumulus dunite growth in a laboratory thermal gradient. Contributions to Mineralogy and Petrology 99:306–319. doi:10.1007/BF00375364

Waters C, Boudreau AE (1996) A reevaluation of crystal-size distributions in chromite cumulates. American Mineralogist 81:1452-1459

Watson EB (1982) Basalt contamination by continental crust: some experiments and models. Contributions to Mineralogy and Petrology 80:73-87

White SM, Crisp JA, Spera FJ (2006) Long-term volumetric eruption rates and magma budgets. Geochemistry Geophysics Geosystems 7 Q03010

Wright TL, Okamura RT (1977) Cooling and crystallization of tholeiitic basalt, 1965 Makaopuhi lava lake, Hawaii. United States Geological Survey Professional Paper 1004, 78 pp

Yamamoto T (2007) A rhyolite to dacite sequence of volcanism directly from the heated lower crust: Late Pleistocene to Holocene Numazawa volcano, NE Japan. Journal of Volcanology and Geothermal Research 167:119-133

Zak J, Paterson SR, Memeti V (2007) Four magmatic fabrics in the Tuolumne Batholith, central Sierra Nevada, California (USA): Implications for interpreting fabric patterns in plutons and evolution of magma chambers in the upper crust. Geological Society of America Bulletin 119:184-201

Zieg MJ, Lofgren GE (2006) An experimental investigation of texture evolution during continuous cooling. Journal of Volcanology and Geothermal Research 154:74-88

Zimmerer MJ, McIntosh WC (in prep) The timing of caldera eruptions and pluton emplacement at the Mt. Aetna Caldera Complex, central Colorado